Doctoral Thesis

Resonant Plasma-Wave Device for Terahertz Detection and Emission

Jong Yul Park

Department of Electrical Engineering

Graduate School of UNIST

2020

Resonant Plasma-Wave Device for Terahertz Detection and Emission

Jong Yul Park

Department of Electrical Engineering

Graduate School of UNIST

Resonant Plasma-Wave Device for Terahertz Detection and Emission

A thesis/dissertation
submitted to the Graduate School of UNIST
in partial fulfillment of the
requirements for the degree of
Doctor of Philosophy

Jong Yul Park

12 / 03 / 2019

Approved by

Advisor
Kyung Rok Kim

Resonant Plasma-Wave Device for Terahertz Detection and Emission

Jong Yul Park

This certifies that the thesis/dissertation of Jong Yul Park is approved.

12 / 03 / 2019

signature

Advisor: Kyung Rok Kim

signature

Kibog Park: Thesis Committee Member #1

signature

Jongwon Lee: Thesis Committee Member #2

signature

Jiwon Chang: Thesis Committee Member #3

signature

Sung-Min Hong: Thesis Committee Member #4;

Abstract

THz technology, which is mainly composed of imaging, spectroscopy, and communication, is appealing to researchers due to its useful properties and various applications such as food inspection and security. Among the electronic device-based THz wave emitter and detector, plasma-wave device (PWD) based on silicon (Si) FET structure has advantages in terms of low cost and large-scale integration. Also, graphene R-PWD is expected to show high performance due to its high mobility. In this thesis, I firstly report the possibility of silicon (Si) plasma wave transistor (PWT) as a resonant terahertz (THz) emitter and detector based on the theoretical analysis focusing on the strained Si with enhanced mobility. Under asymmetric boundary conditions for plasma wave instability, the amplitude of plasma wave in FET channel increases and this plasma wave increment provides the basis of the electromagnetic (EM) wave emission from FET and responses for external THz signal. Secondly, a novel structure of floating gate R-PWT with suspended channel is introduced with considering graphene having ultra-high channel mobility. Finally, I report experimental evidences for plasma-wave resonance in strained-Si channel FET based on the design window of R-PWT. I explain three reasons why resonance occurs with various measurement data: Resonant peak exist above-threshold regime and its output response voltage increase non-linearly as external frequency increases when quality factor $Q = \omega' \tau_{eff} > 1$ condition is satisfied.

Contents

List of figures

List of tables

Nomenclature

THz	Terahertz
EM wave	Electromagnetic wave
FET	Field-effect transistor
R-PWD	Resonant plasma-wave device
R-PWT	Resonant plasam-wave transistor
FG SC-PWD	Floating gate R-PWD with suspended-channel
2DEG	Two-dimensional electron gas
HEMT	High electron mobility transistor
n-MODFET	N-type modulation doped FET
Si	Silicon

Chapter I
Introduction

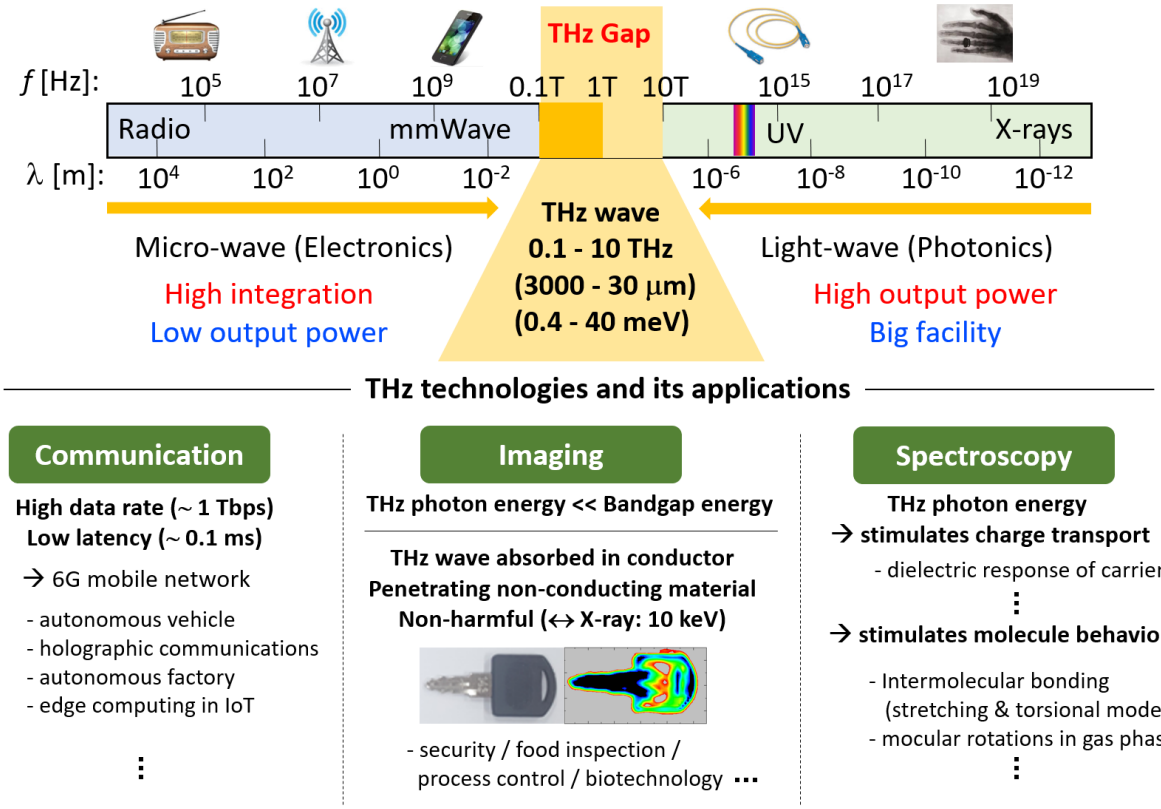

Figure 1-1. THz wave and its applied technologies.

1.1. Terahertz wave properties

Figure 1-1 illustrates that terahertz (THz) wave has frequency range from 0.1 to 10 THz and wavelength range from 3 mm to 30 μm, which is called "THz gap". In wireless communication technology, sub-THz frequency from 0.1 to 1 THz would be chosen for 6G mobile network system, which has higher data rate (~ 1 Tbps) and lower latency (~ 0.1 ms) than of 5G (~ 20 Gbps and 1 ms) so that THz wave is expected to make a breakthrough and give solutions for the beyond 5G societal and business requests such as real time holographic communication and automatic industry with high precision (expected frame error rate ~ $1\text{-}10^{-9}$ in 6G) and enhanced energy efficiency (targeting 1 pJ/bit in 6G) [1-3].

Also, by using Plank's equation, $E=hc/\lambda=hf$, it can be estimated that the radiation power of THz wave has the ranges of 0.4 – 40 meV. Because these photon energies are lower than the band gap energies of non-metallic materials, THz wave has properties to be absorbed in metal and penetrate insulator. Therefore, THz imaging system can be used in the industrial fields of security, food inspection, process control, and biotechnology [4-7], which is safe to human body or bio samples due to its low and non-destructive radiation power compared to X-ray imaging (~ 10 keV). Furthermore, because the behaviors of quasi-particles and collective excitations occur with meV energy scales, the characteristics of charge transport in a material can be clearly revealed by using THz time-domain spectroscopy with measuring ac electrical conductivity [8-10]. THz spectroscopy is also a powerful method to analyze molecular dynamics of meV energy scales. For example, the intermolecular bonding such as stretching and torsional modes, collective water dipole relaxation, and molecular rotations in the gas phase are stimulated by incident THz wave on samples [11-12].

1.2. Photonic approaches and its limitations

There are two ways to fill out the THz gap: One is electronic approaches and the other is photonic approaches as shown in Fig. 1-1. In the case of photonic approaches, a free electron laser (FEL), which generates photons by transverse acceleration of the electrons passing through a periodic arrangement of magnets, have been reported to emit THz wave with average power of 20 W [13]. Despite of its usefulness of academic researches, it is necessary to secure large and expensive facilities. In terms of semiconductor photonics, the photon energy range (0.4 - 40 meV) of THz gap makes it hard to find proper material to emit photon by interband transition from bandgap between conduction and valence bands. To deal with this problem, a quantum cascade laser (QCL), which uses intersubband transitions in a superlattice of semiconductors and covers the wavelength range from near 3 μm to 250 μm, can be a solution to make THz source and shows an order of magnitude in mW scale above f= 1 THz. However, its maximum operation temperature in THz regime is limited up to T~ 200 K [14]. A THz molecular laser (ML), which uses rotational transition of molecular gas optically pumped by an infrared (IR) source, can be operated at room temperature. Especially, the THz ML using NH_3 pumped by mid-IR QCL is recently reported to emit 1 mW continuous wave at f= 1.1 THz with ~100 mW pumping laser (f= 29 THz) [15]. Even though THz ML overcomes the temperature limitation with comparable output power of THz QCL, it has more complex structure and bigger size than chip-based THz sources, which is connected to cost efficiency and widespread business-to-customer applications. To achieve versatile THz technologies for communication, imaging, and spectroscopy, electronic approaches are appealing to researchers since it has advantages of low cost, low power consumption, and ability of high integration. In the next chapter, it will be discussed conventional electronic approaches represented as electron transit mode and its limitation due to cut-off frequency. Also, the plasma mode will be introduced to make a breakthrough in this frequency limitation of the sub-THz regime.

1.3. Electronic approaches: Plasma mode vs. conventional transit mode

In the case of conventional electronic devices, there are two categories to be used in millimeter wave (mmW) regime (f= 30-300 GHz): One is two-terminal devices using negative differential resistance (NDR) such as resonant tunneling diode (RTD), impact ionization avalanche transit-time (IMPATT) diode, and Gunn diode. The other is three-terminal devices such as bipolar junction transistor (BJT) and field-effect transistor (FET) with monolithic microwave integrated circuit (MMIC). Even though these are successfully commercialized in the applications of RF/mmW, its high output power below 100 GHz abruptly decreases and falls into the order of μW scale near f= 1 THz, which is lower than any other photonic-based devices [16]. The reason is strongly related to the limitation of electron transit velocity. For example, the operation frequency of Gunn diode is approximately equal to v_s/L_{ac} , where v_s is electron saturation velocity and L_{ac} is active region length [17]. Because it has been reported that planar Gunn diode cannot generate and sustain its signal below L_{ac}= 0.6 μm, its operation frequencies are limited up to 167 GHz considering v_s~ 10^7 cm/s for GaAs and 375 GHz for InP Gunn diode (v_s~ 2.25×10^7 cm/s) [17]. A high-electron-mobility transistor (HEMT), which is also widely used in RF/mmW technology, has the cut-off frequency limitation as [17]

$$f_T = \frac{g_m}{2\pi C_{gs}} \cong \frac{v_s}{2\pi L}$$

where g_m is transconductance, C_{gs} is gate-to-source capacitance, and L is gate length. This equation shows that gate length scaling with securing high v_s guarantees device operation at higher frequency, which is similar to the case of two-terminal devices. However, as the gate length shrinks down and becomes comparable to the thickness of barrier layer, the short channel effect occurs in the device and the cut-off frequency is saturated so that exceeding 1 THz of operation frequency is very challenging [18].

To make a breakthrough in this cut-off frequency limitation, in 1993, M. Shur has proposed theoretically that resonant plasma-wave, which is temporal and spatial collective oscillation of 2DEG electrons in the channel of FET, can generate THz wave with boundary conditions at source and drain side [29]. This plasma-mode FET, which is named as plasma-wave transistor (PWT), is experimentally proven by various research groups. Another impressive point of PWT is that Si, which have been used in channel material of CMOS in RF application at lower frequency than III-V HEMT case due to its low mobility, low electron saturation velocity, and narrow band gap, even can attain to THz regime, as illustrated in Fig. 1-2 [19]. It means that it is possible to make Si THz PWT based on CMOS technology with lower cost and higher integration than any other photonic and electronic devices.

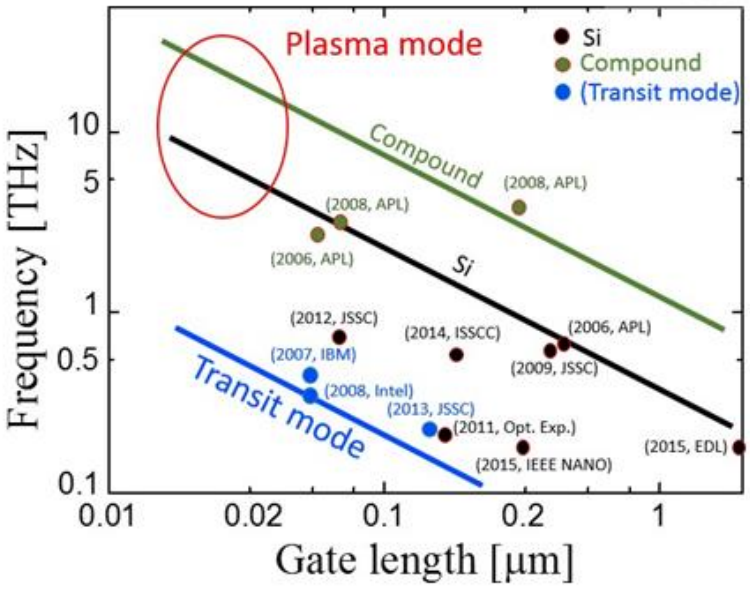

Figure 1-2. Comparison of plasmonic and transit mode operating frequency limits vs. gate length for several semiconductor materials.

1.4. Resonant mode vs. non-resonant plasma mode

In terms of THz detection, the plasma-mode can be categorized into resonant (R) and non-resonant (NR) mode whose schematic views are illustrated in Fig. 1-3. Firstly, non-resonant THz detection can be achieved when boundary conditions of $C_{gs} > C_{gd}$ or $C_{gs} < C_{gd}$ are implemented [4-7] since the NR plasma-wave, which consists of source and drain injected electrons by external THz signal ($V_a\cos(\omega t)$) on the gate, should have voltage difference between source and drain boundaries so that output voltage has the value of V_{out}= <$V(x= l_{eff})$> – <$V(x= 0)$>. As gate voltage increases, inversion electrons make a channel below the gate and plasma-wave velocity increases ($s \propto (V_g - V_{th})$^1/2) so that plasma-wave started from source side attains drain side. In this case, if the ideal boundary conditions of ac short at source ($|Z_s|= 0$) and ac open ($|Z_d|= \infty$) at drain are implemented, plasma-wave resonance occurs and amplitude increases at drain side, which means that output voltage by THz signal can be measured. Considering THz detection applications, it is possible for R-PWT to detect THz signal above 1 THz with higher V_{out} due to plasma-wave resonance for each gate voltages compared to NR-PWT as shown in Fig 1-3. Also, the other advantage of R-PWT is that it can be operated as THz emitter by modulating drain voltage (as detailed in chapter 2.2.1).

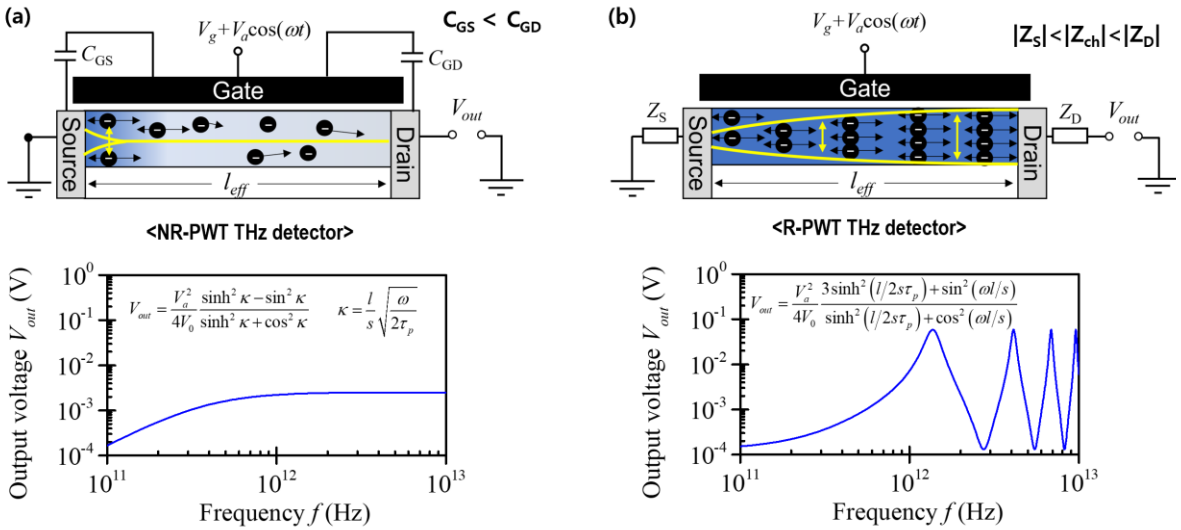

Figure 1-3. Schematic view and theoretical output voltage (V_{out}) [25] for external THz signal of (a) NR-PWT and (B) R-PWT. Both cases are assumed that electrons are injected only from the source ($C_{gs} << C_{gd}$) and $|Z_s| < |Z_{ch}| < |Z_d|$.

1.5. Motivation

Because it has been deemed that high channel mobility is necessary for plasma-wave resonance due to multiple reflection at drain and source side, III-V HEMTs and graphene FET have been extensively investigated for plasma-mode THz emitters [26-28] and detectors [20-25,34] with a tunable frequency above 1 THz at room temperature. Because of low channel mobility in Si FETs, only non-resonant detectors have been demonstrated on CMOS technology platform in sub-THz regime (< 1 THz) [4-7]. Despite the CMOS-based plasmonic THz detectors are showing comparable performance with other commercial THz detectors operating at room temperature, there has been no experimental report of resonant THz wave detection and emission based on Si CMOS devices that has a lot of advantages such as low-cost small-size integrated THz systems on a chip with both detector and emitter. In this thesis, physical analysis of R-PWT THz emitter and detector (chapter II), which based on ideal assumption, is presented firstly in order to derive analytic equations smoothly for non-ideal cases. Also, novel device concept of floating gate R-PWD with suspended-channel (FG SC-PWD) is introduced to maximize the performance of graphene with its ultra-high mobility (chapter III). Taken these together, a design window for R-PWT and FG SC-PWD is introduced, which can make researchers to judge the possibility of plasma-wave resonance for specific channel materials (chapter IV). Finally, experimental results of plasma-wave resonance using Si quasi-ballistic FET is reported with explanation of three evidences (chapter V).

Chapter II
Theory of resonant plasma-wave transistor (R-PWT)

2.1. Introduction

After theoretical possibility for resonant THz plasma-wave generation in FET channel was revealed by M.Shur [29], there has been several progresses related to theoretical framework of R-PWT based on FET structure such as resonant THz detection [33], analysis of plasma-wave drain reflection coefficient [35], definition of effective momentum relaxation time (τ_{eff}) which explains damping of plasma-wave [28], the effect of diffusion and viscosity on plasma-wave resonance [37]. However, there are still absence of consideration of relatively low channel mobility materials. Therefore, the conventional experimental researches of resonant mode have been focused on HEMT structure to obtain high channel mobility, as discussed in previous section 1.5. In this chapter, it will be shed light on the theory of R-PWT considering plasma-wave with covering the assumption of $s \sim v_0$ for analyzing relatively low channel mobility material (section 2.2) and finite drain impedance $|Z_d|$ to make sure realistic possibility of R-PWT (section 2.3). Also, it will be introduced how to evaluate the radiation power of R-PWT by deriving power equation which combines with the theories of plasma-wave and dot-charge dipole (section 2.4). Finally, it will be reviewed the definition of τ_{eff} and reported V_{out} equations for PWT THz detection. Based on these concepts, the wavenumber and V_{out} equations are newly derived to investigate resonant peaks near threshold voltage of R-PWT considering $s \sim v_0$ case of low mobility and short channel length (section 2.5).

2.2. Resonance phenomena in PWT

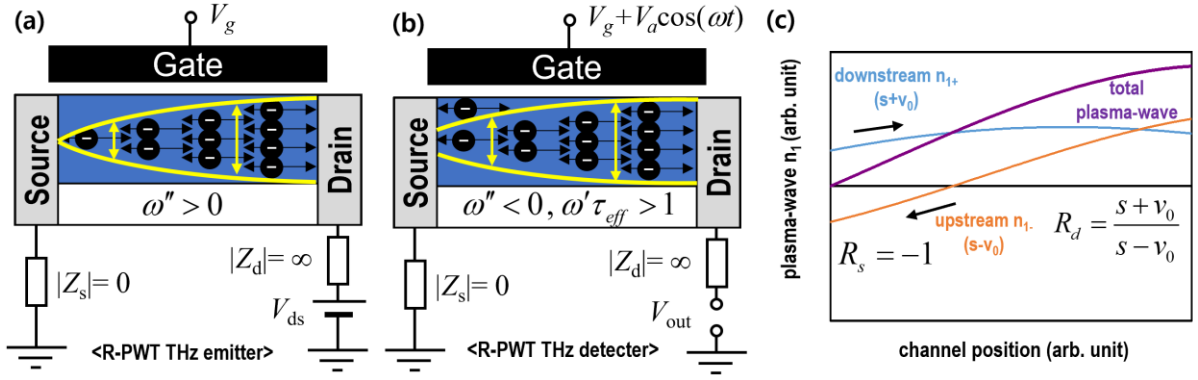

Figure 2-1. Schematic views of (a) R-PWT THz emitter and (b) THz detector assuming ideal boundary conditions. (c) Plasma-wave consisting of downstream and upstream for THz emission case

The most important variable in the theory of conventional FET is the electron drift velocity (v_0) to demonstrate local electron drift transport under the finite channel mobility (μ) and the momentum relaxation time (τ_p). In high density ballistic channel with gate overdrive voltage ($U_0 = V_g - V_{th}$ where V_g is the gate voltage and V_{th} is the threshold voltage), though, the frequent collisions between the local electrons cause the collective behavior of channel 2DEG. The plasma-wave, which is the oscillation (wave) of the 2DEG density (plasma), can be generated in the channel of FET (i.e. PWT) under ideal boundary conditions of ac open at drain ($|Z_d| = \infty$) and ac short at source (impedance $|Z_s| = 0$) [29]. This plasma-wave velocity ($s = (eU_0/m)^{(1/2)}$) is the key variable in the theory of PWT, because it decides the angular frequency of plasma-wave ($\omega = \omega' + i\omega''$) and its harmonics under given v_0 of FET by following equations as [29]

$$\omega' = \frac{s^2 - v_0^2}{2l_{eff}\, s} N\pi \tag{2.1}$$

$$\omega'' = \frac{s^2 - v_0^2}{2l_{eff}\, s} \ln\left|\frac{s+v_0}{s-v_0}\right| - \frac{1}{2\tau_p} \tag{2.2}$$

where l_{eff} is the effective channel length and N is an odd integer explaining resonant plasma-wave harmonics. It is notable that the amplitude of plasma-wave increases as time elapse if $\omega'' > 0$ since the plasma-wave can be represented as $n(x,t) \sim \exp(\omega'' t)$. In this case, it is feasible that the R-PWT can be operated as THz emitter (see Fig. 2-1(a)), whose emission mechanism of EM wave and evaluated radiation power will be discussed in section 2.4. Also, the resonance of plasm-wave cannot occur itself if $\omega'' < 0$ so that it is necessary to bias ac THz wave ($U_a\cos(\omega t)$) on the gate of R-PWT in order to provide energy to plasma-wave, as illustrated in Fig. 2-1(b), whose detailed discussion in section 2.5. Figure 2-

1(c) shows that the plasma-wave makes standing wave represented by the resonant frequency of Eq. (2.1) from the superposition of upstream and downstream plasma-waves with different velocity during reflections in the quasi-ballistic or diffusive channel cavity. To conduct quantitative and physical analysis of this plasma-wave resonance in gated PWT channel, the decomposed analytical model of upstream and downstream in the resonant channel cavity with finite $\mu(\tau_p)$ is now being derived focusing on the fundamental (lowest) mode (N= 1).

By using the governing formalism of the first order of hydrodynamic Euler equation and continuity equation as [29]

$$\frac{\partial v_1}{\partial t} + v_0 \frac{\partial v_1}{\partial x} + \frac{e}{m}\frac{\partial n_1}{\partial x} + \frac{v_1}{\tau_p} = 0 \tag{2.3}$$

$$\frac{\partial n_1}{\partial t} + n_0 \frac{\partial v_1}{\partial x} + v_0 \frac{\partial n_1}{\partial x} = 0 \tag{2.4}$$

and combining Eq. (2.3) and (2.4) with the considerations of the first-order oscillation terms as n_1, v_1, and U_1 in the oscillatory plasma-wave $n(x,t)= n_0+n_1(x)\exp(i\omega t)$, electron velocity $v(x,t)= v_0+v_1(x)\exp(i\omega t)$, and electric potential $U(x,t)= U_0+U_1(x)\exp(i\omega t)$, where $n_0= C_{ox}U_0/e$ is the surface electron density, C_{ox} is the areal capacitance of the oxide, e is the elementary electronic charge [29], the analytical solutions of the divided downstream and upstream plasma-wave dispersion relation explicitly as

$$k_{\pm} = \frac{\omega'}{(v_0 \pm s)} + i\frac{\omega''}{(v_0 \pm s)} + i\frac{\tau_p^{-1}}{2(v_0 \pm s)} = \alpha_{\pm} + i\beta_{\pm} + i\zeta_{\pm} \tag{2.5}$$

where k_+ and k_- are the wavenumber of downstream and upstream plasma-wave as illustrated in Fig. 2-1(c). It should be noted that there is an assumption of $2sk > 1/\tau_p$ to derive Eq. (2.5), which means R-PWT has high channel mobility. It will be dealt in section 2.5.3 which considers $2sk \sim 1/\tau_p$ condition to derive wavenumber and V_{out} equations for resonant THz detection in low mobility channel.

From Eq. (2.5), the oscillatory terms of n_1 can be divided into the linear-independent superposition of n_{1+} and n_{1-} as

$$\begin{aligned} n_1(x,t) &= n_{1+} + n_{1-} = \left(C_+ e^{ik_+ x} + C_- e^{ik_- x}\right)e^{-i\omega t} \\ \mathrm{Re}[n_{1\pm}(x,t)] &= C_{\pm} e^{-(\beta_{\pm}+\zeta_{\pm})x+\omega'' t}\left[\cos(\alpha_{\pm}x)\cos(\omega' t) + \sin(\alpha_{\pm}x)\sin(\omega' t)\right] \end{aligned} \tag{2.6}$$

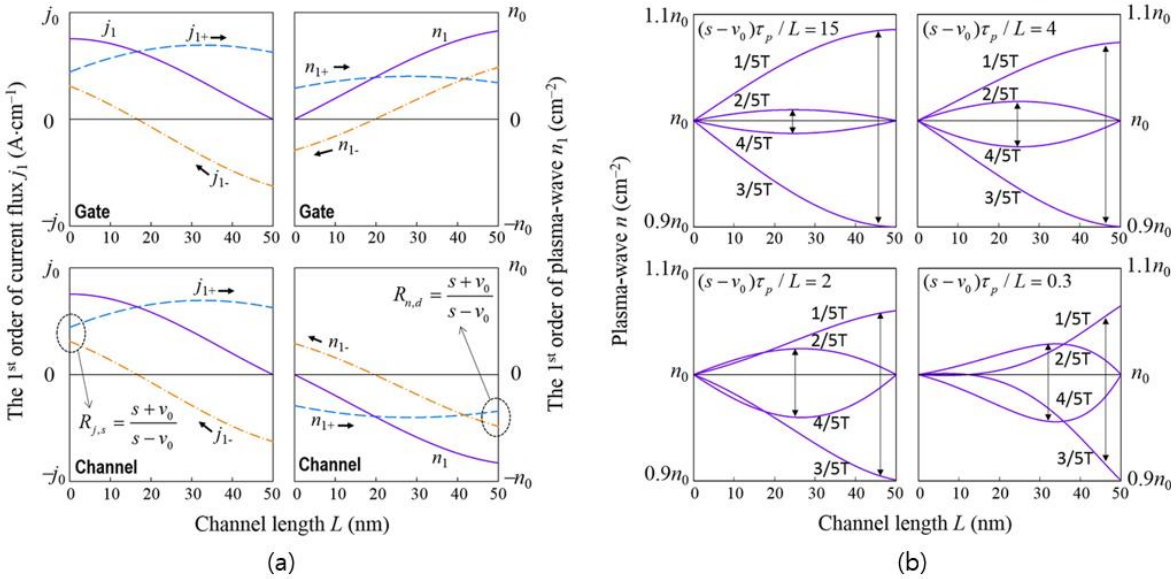

Figure 2-2. (a) The calculation results of 1st harmonic (N=1) n_1 and j_1 after 150 ps in the gate and channel for PWT with L= 50 nm, τ_p= 100 fs, m= 0.028m_0, s= 1.5×10^8 cm/s, and v_0= 2.6×10^7 cm/s. Here f= 7 THz, n_0= 7.73×10^{12} cm^{-2} and j_0= 32 A·cm^{-1} assuming the initial perturbation coefficient C_+= - C_-= 2.16×10^5 cm^{-2}. (b) The evaluated waveforms of 1st harmonic plasma-wave n (= n_0+n_1) in the same PWT channel in Fig. 2-2 for s= 7.70×10^8, 2.25×10^8, 1.25×10^8 and 4.00×10^7 cm/s, respectively. in each plot. Harmonic waveforms with different period (T) are plotted at each same periodic time of T/5 2T/5, 3T/5, and 4T/5.

where C_+ and C_- are initial coefficients for downstream and upstream. Furthermore, v_1 and U_1 also have these initial perturbation coefficients, which are not clearly defined in their relations and thus, it is difficult to derive the analytical solution for the current density $j(x,t)$ from the simple relation of $j/q=nv$ $= n_0v_0 + (n_1v_0 + n_0v_1)e^{-i\omega t} + n_1v_1e^{-2i\omega t}$ with the 1st-order current flux of $j_1 = (n_1v_0 + n_0v_1)e^{-i\omega t}$.

At this point, for the analytical j_1 with more simple formalism (not by defining v_1 with unknown perturbation coefficients), we consider the first order of continuity equation as

$$\frac{\partial n_1}{\partial t} + v_0\frac{\partial n_1}{\partial x} + n_0\frac{\partial v_1}{\partial x} = 0 \tag{2.7}$$

which yields the analytical solution of $n_1v_0 + n_0v_1 = (\omega/k)n_1 = j_1$.

Using these analytical approaches, j_1 can be defined in the form of linear-independent upstream and downstream as

$$j_1(x,t) = j_{1+} + j_{1-} = \mathrm{Re}\left[\left(\frac{\omega}{k_+}C_+e^{ik_+x} + \frac{\omega}{k_-}C_-e^{ik_-x}\right)e^{-i\omega t}\right] \tag{2.8}$$

with each phase velocity of $\omega/k_\pm$ which is plasma-wave velocity rather than electron drift velocity.

As shown in Fig. 2-2(a), by using Eqs. (2.6) and (2.8), it is feasible to illustrate the behavior of decomposed plasma-waves $n_{1\pm}(x,t)$ and current fluxes $j_{1\pm}(x,t)$ both in the PWT channel and gate where collision terms ($e^{-\zeta_{1\pm}x}$) are included. There have been vague arguments for plasma-wave reflections at the boundaries. In Ref. [29], Dyakonov and Shur state that the amplitude ratio of the reflected and oncoming waves is $(s+v_0)/(s-v_0)$ without considering the exact terminology of reflection coefficient. In the other theoretical report by F. J. Crowne [35], the reflection coefficient $(v_0-s)/(v_0+s)$ is always lower than unity in absolute value for $0 < v_0 < s$. On the one hand, the current and voltage reflection coefficient for the Dyakonov-Shur instability has been studied by M. V. Cheremisin et. al. [42] in the form of equation. In this work, we conducted the physical analysis for the reason why the reflection coefficients are larger than unity by taking the analogy with the transmission line model between gate and channel. This theoretical analogy itself has been mentioned in Dyakonov-Shur theory [29]. But our present work is distinguished in that we take this analogy to investigate the reason why reflection coefficient > 1 as illustrated in Fig. 2-2(a).

It is noticeable that the relation between current flux and plasma-wave is similar to the current and voltage waves in the transmission line theory. As a starting point, let us consider that the j_{1+} (downstream) propagates to the boundary of drain-channel (lower-left one of Fig. 2-2(a)). Due to ac open condition on drain side ($Z_{GD} = \infty$ at $x = L$), the j_{1+} reflects with −180° of phase difference to make $j_1(x = L) = 0$ so that the reflection coefficient of j_1 at the drain side is $R_{j,d} = -1$. The n_{1+} (downstream) at the drain-channel boundary is also reflected and converts to n_{1-} (upstream) in the channel (lower-right one of Fig. 2-2(a)). At this reflection of n_1, the n_{1+} has the same phase with the n_{1-} since the number of electrons should increase at the drain side by the additional electrons in the reflected j_{1-} (upstream) in the channel. By the boundary condition of $j_1(L) = 0$ from Eq. (2.8), the reflection coefficient ($R_{n,d}$) for the n_1 at the drain side can be defined from Eq. (2.6), which is given by

$$R_{n,d} = \frac{n_{1-}(L)}{n_{1+}(L)} = \frac{k_+}{k_-} = \frac{s+v_0}{s-v_0} \tag{2.9}$$

Subsequently, the upstream n_{1-} and j_{1-} propagate to source in the channel and transfer to the gate region (upper ones of Fig. 2-2 (a)) since the channel and gate is related to the ac short condition at the source (x=0). Therefore, the j_{1-} from the gate region also flows to the channel and convert to j_{1+} with increasing plasma-wave velocity that has the same phase to the j_{1-} in the channel. Thus, it is clear that the j_{1-} is just reflected and changed to the j_{1+} so that the reflection coefficient ($R_{j,s}$) of j_1 at the source side can be evaluated by each components of $j_{1+}(0)$ and $j_{1-}(0)$ using Eq. (2.8):

$$R_{j,s} = \frac{j_{1+}(0)}{j_{1-}(0)} = \frac{k_+}{k_-} = \frac{s+v_0}{s-v_0} \tag{2.10}$$

At the source side with zero impedance at x= 0 (ac short condition), the n_1 becomes zero since the phase of transferred n_{1+} from the gate region is directly opposite to the n_{1-} in the channel, i.e. the reflection coefficient of n_1 at the source side is $R_{n,s}$= −1. The results of Eqs. (2.9) and (2.10) represent that $R_{n,d}$ and $R_{j,s}$ are always higher than unity when U_{DS} is biased while they become unity without U_{DS} that is the same results for the standing wave in the transmission line theory with the same boundary conditions and ac voltage source [43].

The sum of j_{1+} and j_{1-} makes standing wave (j_1) which has anti-node and node at the source and drain side, respectively, while the sum of n_{1+} and n_{1-} also makes standing wave (n_1) that has node and anti-node at the drain and source side, respectively. It is noteworthy that the plasma-wave resonance is originated from these standing waves with the increment of the amplitude during multiple reflections. Because the n_1 in the channel and gate are different each other with the phase of −180°, the electric dipole is formed and oscillates in the R-PWT, which means the electromagnetic (EM) wave is emitted with THz frequency.

By using this theoretical analysis of the plasma-wave in the channel, Figure 2-2 (b) describes that the resonance quality of plasma-wave is decided by the $(s-v_0)\tau_p/L$. condition. In terms of resonance, the ideal case is that standing wave has fixed node and anti-node, which connected that the simple harmonic oscillator is formed. In the channel of PWT, though, the plasma-wave oscillation rather shows the behavior of coupled harmonic oscillator, which distributes the energy to make intended frequency and intensity of electromagnetic wave, as shown at points in 2T/5 and 4T/5 in Fig. 2-2 (b).

In comparable s~v_0 range, the $(s-v_0)\tau_p/L$ condition can become a criterion to judge how standing wave is close to the simple harmonic oscillator. As the velocity of upstream is decreased by increasing v_0 or decreasing s, which means that $(s\text{-}v_0)\tau_p/L$ is lowered and $R_{n,d}$ is increased, the resonance quality becomes worse as shown in Fig. 2-2 (b) because the simple harmonic oscillator gradually changes to the coupled harmonic oscillator as the velocity difference between downstream and upstream increase.

2.3. Influence of finite drain impedance on R-PWT

Based on FET structure, the ideal operation principle of R-PWT should consider ideal boundary conditions of ac short at source side ($|Z_s|= 0$) and ac open at drain side ($|Z_d|= \infty$). With these boundary conditions, drain reflection coefficient becomes higher than unity and plasma-wave resonance occurs in the channel of R-PWT when biasing gate overdrive voltage ($U_0= U_g–U_{th}$) and drain voltage (U_{ds}) [29].

In comparison with ac short at source side, achieving infinite $|Z_d|$ for ac open is so challenging that finite $|Z_d|$ should be considered for practical analysis. Considering finite $|Z_d|$, Eq. the 1st order of current flux at drain side as

$$j_1(l,t) = \frac{U_1(l)}{|Z_d|W} = \mathrm{Re}\left[\left(\frac{\omega}{k_+}C_+e^{ik_+l} + \frac{\omega}{k_-}C_-e^{ik_-l}\right)e^{-i\omega t}\right] \tag{2.11}$$

where W is channel width. Under infinite $|Z_d|$ the 1st order of current flux becomes zero. By using Eq. (2.11), it is possible to yield drain reflection coefficient at drain side as follows:

$$r_d = \frac{n_{1-}(l)}{n_{1+}(l)} = \frac{|Z_d|WC_{ox}(s+v_0)-1}{|Z_d|WC_{ox}(s-v_0)+1} \tag{2.12}$$

where C_{ox} is the areal capacitance of the oxide. If the drain impedance is infinite, Eq. (2.12) becomes Eq. (2.9). The transmission line theory implies that Eq. (2.12) can be represented as

$$r_d = \frac{|Z_d|/|Z_{ch}^+|-1}{|Z_d|/|Z_{ch}^-|+1} \tag{2.13}$$

$$|Z_{ch}^{\pm}| = \frac{1}{WC_{ox}(s\pm v_0)} = \left\{\frac{1}{|Z_{ch}|}+\frac{1}{(\pm|Z_e|)}\right\}^{-1} = \frac{|Z_e||Z_{ch}|}{|Z_e|\pm|Z_{ch}|} \tag{2.14}$$

where $Z_{ch}^{\pm}$ are channel plasma-wave impedances for downstream and upstream, respectively. If there is no applied drain bias (i.e. $v_0= 0$), $|Z_{ch}^{\pm}|= |Z_{ch}|$ is exactly same to the characteristic impedance $|Z_0|= (L_{ch}/C)^{-1}$ in transmission line theory, where $L_{ch}= ml/e^2n_0W$ is kinetic inductance, m is electron effective mass, and $C= WC_{ox}$ [44]. In this case, the plasma-wave for downstream and upstream have the same

plasma-wave velocity s which means $r_{d,i}= 1$ and $r_d < 1$ for ideal and realistic case, respectively. By applying drain bias, electrons flow toward drain side with v_0 and upstream plasma-wave has slower velocity ($s_-= s-v_0$) than downstream ($s_+= s+v_0$), which means that the propagation of upstream is obstructed so that $|Z_{ch}^-|$ has higher impedance than $|Z_{ch}^+|$. This impedance discrepancy, which is due to channel drift electron impedance $|Z_e|$, causes r_d to be higher than unity and necessary minimum $|Z_d|$ for unity r_d can be easily derived as follows:

$$\left|Z_{d,\min}\right| = \left|Z_e\right| = \frac{1}{WC_{ox}v_0} \tag{2.15}$$

The drain reflection coefficient considering finite drain impedance changes imaginary part of angular frequency as follows:

$$\omega'' = \frac{s^2 - v_0^2}{2ls}\ln\left(\frac{\left|Z_d\right|WC_{ox}\left(s+v_0\right)-1}{\left|Z_d\right|WC_{ox}\left(s-v_0\right)+1}\right) - \frac{1}{2\tau_p} \tag{2.16}$$

Considering the physical conditions of $\omega'' > 0$ for resonance, it is possible to derive the critical drain reflection coefficient ($r_{d,c}$) and critical drain impedance ($|Z_{d,c}|$) for plasma-wave resonance as

$$r_{d,c} = \exp\left[\frac{ls}{\left(s^2 - v_0^2\right)\tau_p}\right] \tag{2.17}$$

$$\left|Z_{d,c}\right| = Z_{ch}^+\left(\frac{1+r_{d,c}}{1-r_{d,c}/r_{d,i}}\right) \tag{2.18}$$

Figure 2-3 illustrates that plasma-wave resonance occurs when $|Z_d|>|Z_{d,c}|>|Z_{ch}^+|$. The finite drain impedance allows downstream of plasma-wave (n_{1-}) to pass through drain side so that reflection occurs lesser than infinite $|Z_d|$ case. As frequency increases ($s >> v_0$), the critical drain impedance becomes asymptotically to

$$\left|Z_{d,c}\right|_{f\to\infty} = \frac{1}{WC_{ox}\left\{v_0 - \left(l/2\tau_p\right)\right\}} \tag{2.19}$$

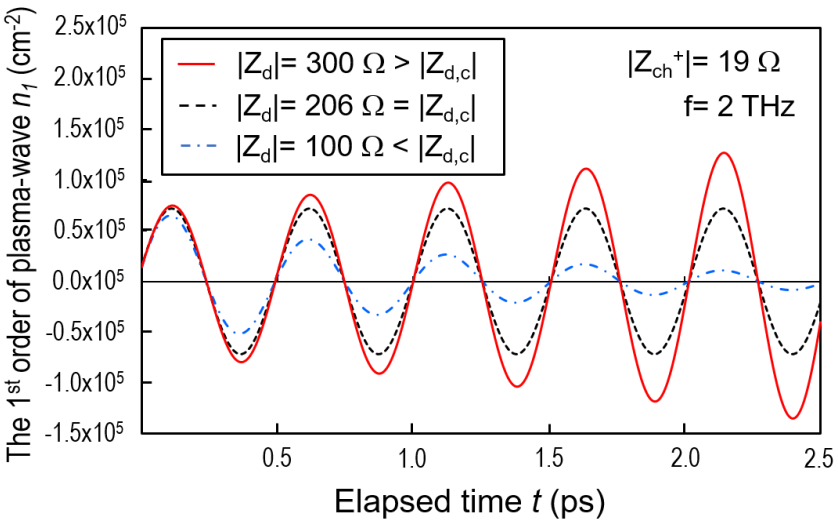

Figure 2-3. The plasma- wave behavior at the drain side for the arbitrary channel material.

In the case of ballistic mobility ($\tau_p = \infty$), $|Z_{d,c}|$ is exactly same to $|Z_e|$ (= $|Z_{d,min}|$). Also, $|Z_e|$ is always bigger than $|Z_{ch}^+|$ when $s > v_0$ because $|Z_{ch}^+|$ is parallel impedance for $|Z_e|$ and $|Z_{ch}|$. Therefore, $|Z_{d,c}|$ is always higher than $|Z_{ch}^+|$, which well explains the fact that drain impedance should be higher than channel impedance for resonance.

When choosing channel material of R-PWT, higher channel mobility is desirable because the electrons, which compose plasma-wave, experience collision with phonons or impurities lesser so that plasma-wave traveling channel can sustain its amplitude longer. From this point of view, exfoliated graphene mobility of which have been reported up to 140,000 $cm^2/V{\cdot}s$ (hall mobility) at room temperature [45] can be a good candidate of channel material of R-PWT. However, exfoliated graphene is hard to be mass produced for commercializing THz R-PWT. Therefore, it is necessary to consider CVD graphene as channel material even if it has lower mobility (μ= 4000 $cm^2/V{\cdot}s$ [46], 7100 $cm^2/V{\cdot}s$ [47] at room temperature as field-effect mobility) than that of exfoliated one.

Figure 2-4 shows the possibility of graphene THz R-PWT for various parameters. For example, Assuming CVD graphene with channel mobility μ= 5000 cm^2/V·s and channel length l= 40 nm, W= 10 μm, and t_{ox}= 5 nm, the critical drain impedance of 200 Ω is always higher than $|Z_{ch}^{+}|$= 10 Ω. In this case, $|Z_d| > 200$ Ω should be imposed for successful operation of THz R-PWT (Fig. 2-4(a)). It should be noted that abrupt increase of $|Z_{d,c}|$ is due to physical property of plasma-wave in the channel of R-PWT. Because decreasing frequency means that s and v_0 also decrease, plasma-wave becomes slower and much more collision occur. Therefore, insufficient amplitude arrives at drain side so that higher $|Z_d|$ should be required for sufficient reflection to occur plasma-wave resonance. In the case of infinite $|Z_d|$, the resonance never occurs if the channel mobility is too low or channel length is too long since plasma-wave is already fully overdamped at drain side (Figs. 2-4(a) and 2-4(b)). Additionally, W and $C_{ox}=\varepsilon/t_{ox}$ are inversely proportional to impedance component as shown in Eqs. (2.15) and (2.18), and (2.19) (Figs. 2-4(c) and 2-4(d)).

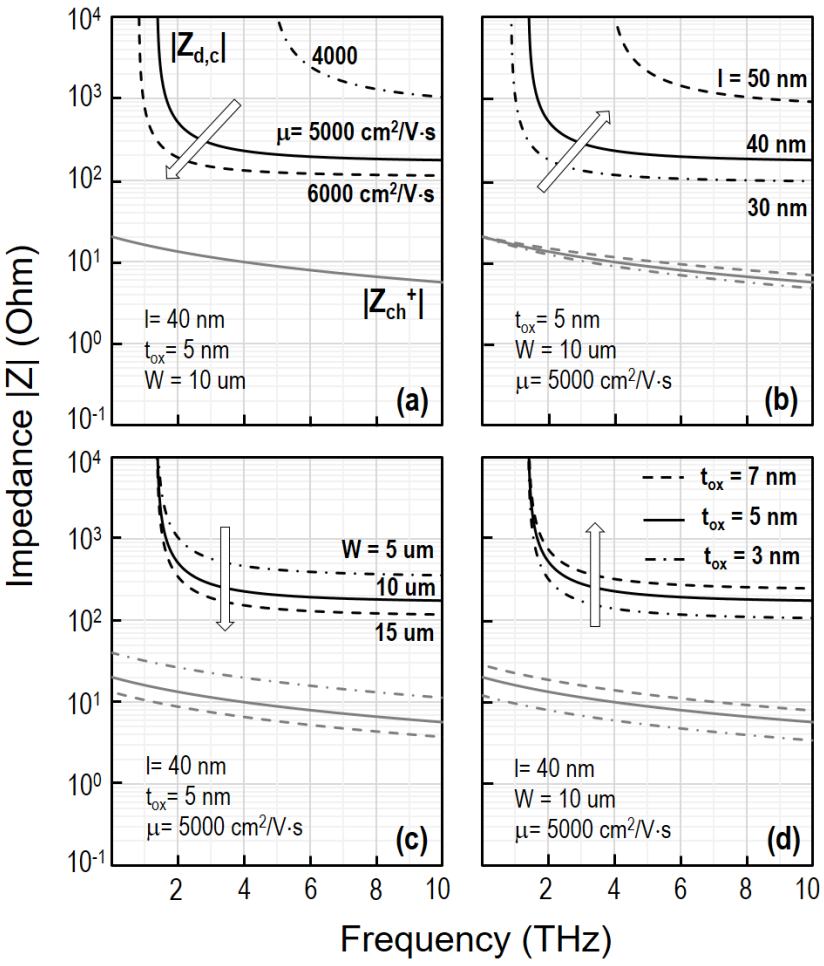

Figure 2-4. $|Z_d|$ vs. frequency plot to show the possibility of graphene THz R-PWT for the various parameters of (a) channel mobility, (b) channel length, (c) channel width, and (d) oxide thickness. Hexagonal BN is assumed as oxide material.

Furthermore, in terms of high integration and cost efficiency for the commercial impact in THz applications, it is essential to achieve Si R-PWT. For this purpose, considering finite $|Z_d|$ on theoretical analysis is helpful for investigating realistic possibility of resonance in the Si channel. Figure 2-5 shows $|Z_{d,c}|$ and $|Z_{ch}^{+}|$ for strained Si (s-Si) R-PWT with variation of channel width (W= 10, 30, 50 nm) and reported MOSFET channel mobility (μ= 500, 650, 800 cm^2/V·s) [48,64]. Compared to Fig. 2-4 of CVD graphene case, evaluated $|Z_{d,c}|$ is higher than graphene by two or three orders of magnitude, since short channel width is assumed (cf. $|Z_{d,c}|$~ 100 Ω for assumed s-Si R-PWT with W= 10 μm). It is recommended to fabricate the channel width of R-PWT as short as possible in order to suppress oblique plasma-wave mode [21,49]. The 10-100 kΩ scale of $|Z_{d,c}|$ for s-Si R-PWT has no problem for actual experiment because the load impedance of lock-in-amp (LIA) is 10 MΩ [50]. The detailed experimental results and discussion of Si R-PWT will be dealt in chapter V.

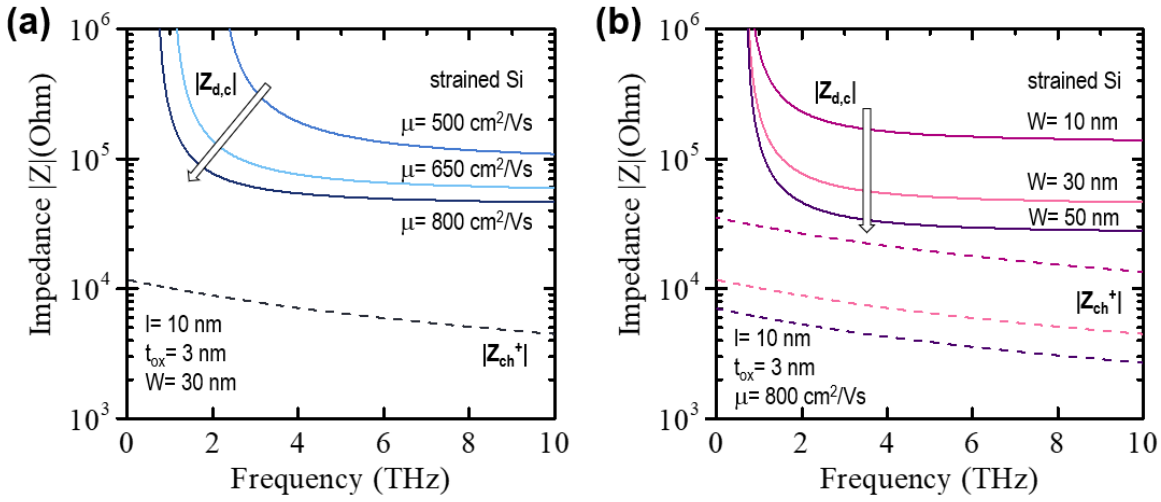

Figure 2-5. $|Z_d|$ vs. frequency plot to show the possibility of s-Si THz R-PWT for the various parameters of (a) channel mobility, (b) channel width. SiO_2 is assumed as oxide material.

2.4. R-PWT THz emission

Considering the device structure of R-PWT, longitudinal THz plasma-wave generated by 2DEG is converted into TEM mode electromagnetic (EM) waves in free-space through capacitive coupling between channel plasma-wave and gate mirror image plasma-wave [29]. M. Shur briefly introduced electrostatic power estimation as $P \sim C_{ox}U_1^2 W v_0$, by which the maximum radiation power was estimated 2 mW at f= 1.5 THz for l= 200 nm, W= 100 μm, v_0= 10^7 cm/s, s= 1.15×10^8 cm/s, d= 35 nm, ε= 13, and U= 0.5 V [29]. Even though this estimation referred to upper bound of the actual radiated power, the experimental results have been reported to be ~μW scale [51]. In order to improve and attain to the upper bound of the radiated power of R-PWT THz emitter, it is essential to derive analytical power equation, which have not been reported yet.

The basic idea to derive power equation is combining conventional dot-charge dipole theory and 2DEG plasma-wave theory, as illustrated in Fig. 2-6. The electric potential from R-PWT and surface charge is given by,

$$V(\vec{r},t) = \frac{1}{4\pi\varepsilon_0}\left[\int \frac{\rho(\vec{r}'_+,t_r)}{|\vec{R}_+|}d\tau' - \int \frac{\rho(\vec{r}'_-,t_r)}{|\vec{R}_-|}d\tau'\right] \tag{2.20}$$

$$\rho(\vec{r}',t) = e\{n_0 + n_1(x')e^{-i\omega t}\} \tag{2.21}$$

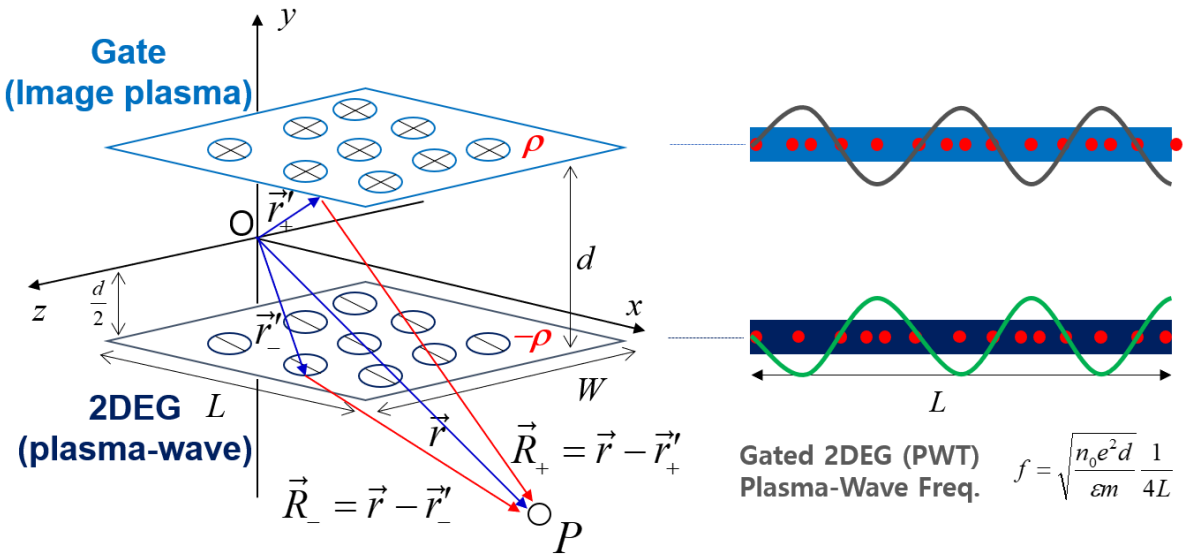

Figure 2-6. Concept of combining conventional dot-charge dipole and 2DEG plasma-wave theory for yielding radiated power equation.

By using approximation of $r'_{\pm} << r$ and $r' << \lambda = (2\pi c)/\omega$ considering its actual measurement point and short wavelength of THz wave ($\lambda = 100\ \mu m$ at $= 3$ THz), the electric potential is yielded as

$$V(\vec{r},\theta,t) = -\frac{ed\omega}{4\pi\varepsilon_0 c}\left(\frac{\cos\theta}{r}\right)\xi e^{-i\omega\left(t-\frac{|r|}{c}\right)} \tag{2.22}$$

$$\xi = WC_+\left[K' + iK''\right], \quad K = \frac{\xi}{WC_+} \tag{2.23}$$

$$K' = \frac{\kappa''_{+,s} + \kappa'_{+,c} - k'_+}{k'^2_+ + k''^2_+} - \frac{\kappa''_{-,s} + \kappa'_{-,c} - k'_-}{k'^2_- + k''^2_-}, \qquad K'' = \frac{\kappa'_{+,s} - \kappa''_{+,c} + k''_+}{k'^2_+ + k''^2_+} - \frac{\kappa'_{-,s} - \kappa''_{-,c} + k''_-}{k'^2_- + k''^2_-}$$

$$\kappa'_{\pm,s} = k'_\pm e^{-k''_\pm l}\sin\left(k'_\pm l\right), \quad \kappa'_{\pm,c} = k'_\pm e^{-k''_\pm l}\cos\left(k'_\pm l\right)$$

$$\kappa''_{\pm,s} = k''_\pm e^{-k''_\pm l}\sin\left(k'_\pm l\right), \quad \kappa''_{\pm,c} = k''_\pm e^{-k''_\pm l}\cos\left(k'_\pm l\right)$$

where ξ is related to plasma-wave behavior in the channel of R-PWT, K and κ are defined wavenumbers for ease of calculations. Next, the vector potential can be obtained by considering displacement current between floating gate and suspended channel, which is result in

$$A(\vec{r},t) = -\frac{\mu_0 qd\omega}{4\pi r}\xi e^{-i\omega\left(t-\frac{|r|}{c}\right)}\hat{y} \tag{2.24}$$

Based on Eq. (2.22) and (2.24), the electric and magnetic field can be obtained by using approximation of $r >> \lambda = (2\pi c)/\omega$ due to the same reason of deriving Eq. (2.24), as follows:

$$\vec{E} = i\frac{\mu_0 qd\omega^2}{4\pi}\left(\frac{\sin\theta}{r}\right)\xi e^{-i\omega\left(t-\frac{|r|}{c}\right)}\hat{\theta} \tag{2.25}$$

$$\vec{B} = i\frac{\mu_0 qd\omega^2}{4\pi c}\left(\frac{\sin\theta}{r}\right)\xi e^{-i\omega\left(t-\frac{|r|}{c}\right)}\hat{\phi} \tag{2.26}$$

Therefore, the Poynting vector and radiated power is

$$\vec{S} = \frac{\mu_0}{c}\frac{q^2d^2\omega^4\xi^2}{16\pi^2}\left(\frac{\sin^2\theta}{r^2}\right)\left\{\sin^2\omega'\left(t-\frac{|r|}{c}\right)\right\}e^{2\omega''\left(t-\frac{|r|}{c}\right)}\hat{r} \tag{2.27}$$

$$\langle P\rangle = \int\left\langle\vec{S}\right\rangle\cdot d\vec{a} = \frac{\mu_0 q^2d^2\left(\omega'^2+\omega''^2\right)^2}{12\pi c}|\xi|^2 e^{2\omega''t_{\max}} \tag{2.28}$$

where t_{max} is a point in time that amplitude of plasma-wave attains to its maximum peak. If $\omega' >> \omega''$, the power equation has simpler form as

$$\langle P \rangle = \frac{\mu_0 q^2 d^2 \omega'^4}{12\pi c} |\xi|^2 e^{2\omega'' t_{max}} \tag{2.29}$$

This result has similar form of the radiated power of dot-charge dipole as follows:

$$\langle P \rangle_{\text{dot-chage dipole}} = \frac{\mu_0 q^2 d^2 \omega^4}{12\pi c} \tag{2.30}$$

Considering CVD graphene PWT with μ= 5000 cm^2/V·s, L= 40 nm, and W= 15 μm, the radiated power of THz wave is evaluated in the range of nW - μW scale, which is strongly influenced by ω'^4 dependency in Eq. (2.25). Even though the validity of power equation (detailed in chapter 2.5) has been conducting, the insufficient emission power of R-PWT motivates to invent a novel PWD structure. A floating gate R-PWD with suspended channel (FG SC-PWD), as part of its efforts, shows mW scale radiation power, which will be discussed in chapter III.

2.5. R-PWT THz detection

2.5.1. Effective momentum relaxation time for plasma-wave

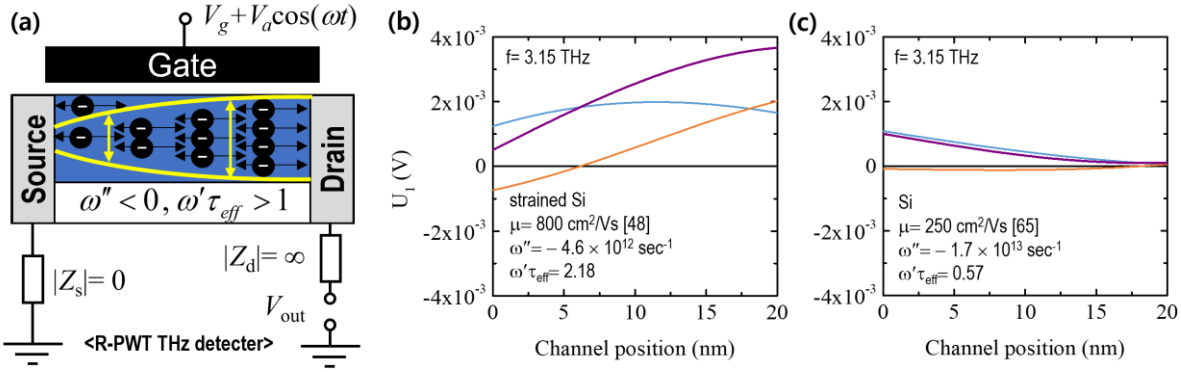

Figure 2-7. (a) Schematic view of R-PWT THz detector. (b) the behavior of resonant plasma-wave assuming strained Si (μ= 800 cm^2/Vs [48]) and (c) Si cases (μ= 250 cm^2/Vs [65]) with V_a= 1 mV.

When $\omega'' > 0$, plasma-wave resonance occurs with biasing small drain voltage so that the amplitude increases as time elapses due to $n_1(x,t) \sim \exp(\omega'' t)$, as detailed in section 2.2. On the contrary, it is obvious that plasma-wave resonance cannot occur itself when $\omega'' < 0$. In this case, it is necessary to bias ac THz wave ($U_a\cos(\omega t)$) on the gate of R-PWT in order to provide energy to plasma-wave so that resonance occur, as illustrated in Fig. 2-7(b). Therefore, R-PWT operates as driven damped harmonic oscillator with forcing frequency (ω) and resonant plasma-wave frequency (ω'). In terms of verifying resonant THz detection, it is essential to consider the effective momentum relaxation time (τ_{eff}) derived from $\omega'' = -1/2\,\tau_{eff}$ as [36]

$$\frac{1}{\tau_{eff}} = \frac{1}{\tau} - \frac{s^2 - v_0^2}{l_{eff}\, s} \ln\left(\frac{s + v_0}{s - v_0}\right) \tag{2.31}$$

Because of high τ_{eff} means less damping of the amplitude of plasma-wave, it is useful to introduce quality factor of $\omega'\tau_{eff}$ for evaluation of R-PWT THz detector. If we consider both strained Si (s-Si) and Si as a channel material of PWT with l= 20 nm, it is impossible to use these PWTs as a THz emitter. However, s-Si PWT with relative high channel mobility (μ= 800 cm^2/Vs [48]) makes it possible to operate as a resonant THz detector with its τ_{eff} = 110 fs (see Fig. 2-7(b)) compared to τ_{eff} = 29 fs for Si case, which still cannot be operated as R-PWT and only have a function as NR-PWT (see Fig. 2-7(c)).

2.5.2. Review on reported V_{out} equations

In this section, it will be reviewed to explain V_{out} equations reported by other research groups. By using similar way of THz emission case, we can assume the following voltage wave equations:

$$U_1 = \mathrm{Re}\left[\left(C_+ e^{ik_+ x} + C_- e^{ik_- x}\right) e^{-i\omega t}\right] \tag{2.32}$$

Also, hydrodynamic Euler equations and continuity equations to describe energy relation as

$$\frac{\partial v_1}{\partial t} + v_0 \frac{\partial v_1}{\partial x} + \frac{e}{m}\frac{\partial U_1}{\partial x} + \frac{v_1}{\tau} = 0 \tag{2.33}$$

$$\frac{\partial U_1}{\partial t} + U_0 \frac{\partial v_1}{\partial x} + v_0 \frac{\partial U_1}{\partial x} = 0 \tag{2.34}$$

Using Eq. (2.32), Eq. (2.34) changes to

$$v_1 = \mathrm{Re}\left[\left(C_+ \frac{\omega - k_+ v_0}{k_+ U_0} e^{ik_+ x} + C_- \frac{\omega - k_- v_0}{k_- U_0} e^{ik_- x}\right) e^{-i\omega t}\right] \tag{2.35}$$

At $x = 0$, $U_1(0,t) = U_a \cos(\omega t) = \mathrm{Re}[U_a \exp(-i\omega t)]$ so that $C_+ + C_- = U_a$. Using Eq. (2.8) at $x = l$ then [52]

$$j_1(l) = \mathrm{Re}\left[e\left(C_+ \frac{\omega}{k_+} e^{ik_+ l} + \left(n_a - C_+\right)\frac{\omega}{k_-} e^{ik_- l}\right) e^{-i\omega t}\right] = 0 \tag{2.36}$$

$$C_\pm = \frac{n_a}{1 - \dfrac{k_\mp e^{ik_\pm l}}{k_\pm e^{ik_\mp l}}} \tag{2.37}$$

Furthermore, it is possible to derive V_{out} equation using Eqs. (2.33) and (2.34) with taking time average and integral for channel length from $x = 0$ to $x = l$, which is given by [52]

$$V_{out} = \left\langle U(l)\right\rangle - \left\langle U(0)\right\rangle = \frac{m}{2e}\left[\frac{\left\langle v_1^2(0)\right\rangle - \left\langle v_1^2(l)\right\rangle}{2}\right] \tag{2.38}$$

$$V_{out} = \frac{U_a^2}{4U_0}\frac{\omega'^2}{\left(\omega - \omega'\right)^2 + \left(1/2\tau_{eff}\right)^2} \tag{2.39}$$

Eq. (2.39) is V_{out} equation only for resonant mode and the general case that contains resonant and non-resonant mode as [33]

$$V_{out} = \frac{U_a^2}{4U_0}\left[1+\beta-\frac{1+\beta\cos\left(2k_0'l\right)}{\sinh^2\left(k_0''l\right)+\cos^2\left(k_0'l\right)}\right],\quad \beta=\frac{2\omega\tau_p}{\sqrt{1+\left(\omega\tau_p\right)^2}} \tag{2.40}$$

$$k_0' = \frac{\omega}{s}\sqrt{\frac{\sqrt{1+\left(\omega\tau_p\right)^{-2}}+1}{2}},\quad k_0'' = \frac{\omega}{s}\sqrt{\frac{\sqrt{1+\left(\omega\tau_p\right)^{-2}}-1}{2}} \tag{2.41}$$

Wavenumbers in Eq. (2.39) and Eq. (2.40) assumes $s >> v_0$ and $\omega\tau_p >> 1$ so that it is not valid for low sub-THz frequency and low channel mobility R-PWT.

Finally, non-resonant mode V_{out} equation: [53]

$$V_{out} = \frac{eU_a^2}{4ms_0^2}\left\{\left[1+\kappa\exp\left(-\frac{eU_0}{\eta k_BT}\right)\right]^{-1}-\left[\left\{1+\kappa\exp\left(-\frac{eU_0}{\eta k_BT}\right)\right\}^2\left[\sinh^2 Q+\cos^2 Q\right]\right]^{-1}\right\} \tag{2.42}$$

$$s_0^2 = \frac{\eta k_BT}{m},\quad Q=\frac{l}{s}\sqrt{\frac{\omega}{2\tau_p}},\quad \kappa=\frac{j_0L^2me}{2C\tau_p\eta^2\left(k_BT\right)^2} \tag{2.43}$$

where η is the ideality factor. The plasma-wave velocity in Eq. (2.42) is defined as

$$s^2 = s_0^2\left[1+\exp\left(-\frac{eU_0}{\eta k_BT}\right)\right]\ln\left[1+\exp\left(\frac{eU_0}{\eta k_BT}\right)\right] \tag{2.44}$$

When $U_0 << 0$, $s = s_0$ which means that plasma-wave injected from source or drain side has velocity by thermal voltage. On the contrary, when $U_0 << 0$, s becomes familiar equation $s=(eU_0/m)^{(1/2)}$ in ideal case.

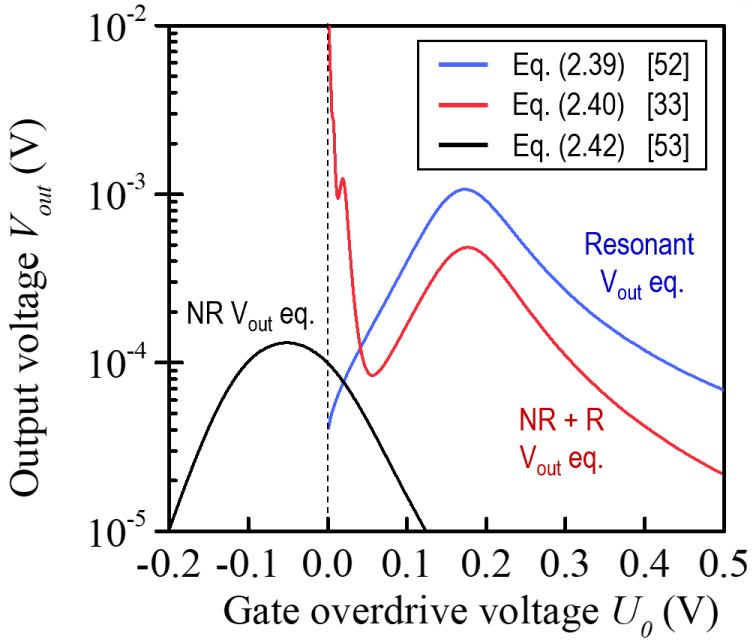

Figure 2-8. V_{out} vs. U_0 plot at f= 5 THz using reported equations for same parameters assuming strained Si (m^*/m= 0.19, μ= 800 cm2/Vs, l_{eff}= 20 nm) as channel material of R-PWT THz detector.

Fig. 2-8 shows each reported V_{out} equation using same parameters at f= 5 THz. It is noticeable that Eqs. (2.39) and (2.40) diverge at $U_0 = 0$ due to $V_{out} \propto 1/U_0$, which cause abrupt increasing V_{out} of Eq. (2.40) near U_0= 0 V and make discrepancy between 'NR+R V_{out} equation' of Eq. (2.40) and 'NR Vout equation' of Eq. (2.42). Thus, it is false to interpret distorted V_{out} at $U_0 = 0$ as peak value of NR V_{out} evaluated by 'NR+R V_{out} equation'. Also, in order to make R-PWT with low channel mobility, it is necessary to achieve short channel length for resonance. However, resonant frequency increases in short channel PWT with same gate voltage compared to long channel due to rapid propagation of plasma-wave from source to drain, as shown in the following equation:

$$\omega' = \frac{s^2 - v_0^2}{2l_{eff}s} N\pi$$

In other words, it is possible to obtain same resonant frequency with slower plasma-wave velocity, which means that R-PWT operates at lower gate voltage and it is required to consider $s \sim v_0$ condition. With considering low channel mobility, this new condition forces to derive new wavenumber k equation without the assumption of $2ks >> \tau^{-1}{}_p$, which will be dealt in next section.

2.5.3. Wavenumber considering low μ and $s \sim v_0$ condition

The general equation of plasma-wave velocity (Eq.(2.44)) is derived by [53]

$$s = \sqrt{\frac{ne^2}{mC}} = \sqrt{\frac{e}{m}\frac{n}{(dn/du)}}\Bigg|_{u=U_0} \tag{2.45}$$

$$n_0 = n^* \ln\left[1+\exp\left(\frac{eU_0}{\eta k_B T}\right)\right], \quad n^* = \eta \frac{C}{e}\frac{k_B T}{e} \tag{2.46}$$

where n_0 is derived from unified charge control model [53]. Figure 2-9 shows that plasma-wave velocity for Eq. (2.44) and $s=(eU_0/m)^{\wedge}(1/2)$. It is obvious that Eq.(2.44) should be considered in the evaluation of V_{out} and its related equations to explain whole range of gate voltage. Also, Eq. (2.45) explains that there is voltage component to determine plasma-wave velocity as

$$U = \frac{n}{(dn/du)} = \frac{\eta k_B T}{e}\left[1+\exp\left(-\frac{eU_0}{\eta k_B T}\right)\right]\ln\left[1+\exp\left(\frac{eU_0}{\eta k_B T}\right)\right] \tag{2.47}$$

which becomes $U= U_0$ when $U_0 >> 0$ and $U= \eta k_B T/e$ when $U_0 << 0$. Because the plasma-wave velocity is defined by Euler and continuity equation, Eq. (2.35) should be changed to

$$v_1 = \mathrm{Re}\left[\left(C_+ \frac{\omega - k_+ v_0}{k_+ U} e^{ik_+ x} + C_- \frac{\omega - k_- v_0}{k_- U} e^{ik_- x}\right) e^{-i\omega t}\right] \tag{2.48}$$

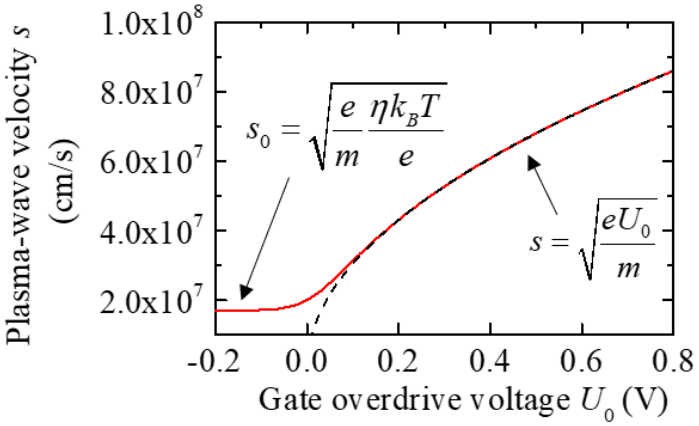

Figure 2-9. s vs. U_0 plot which use Eq. (22) and $s=(eU_0/m)^{\wedge}(1/2)$ for s-Si ($m^*/m= 0.19$) and $\eta = 1.2$

When deriving wavenumber of downstream and upstream (Eq. (2.5)), combining Eq. (2.3) and (2.4) results in

$$\omega = \frac{2kv_0 - i\tau_p^{-1} \pm \sqrt{4k^2s^2 - \tau_p^{-2}}}{2} \tag{2.49}$$

In the section 2.2, $2ks >> \tau^{-1}{}_p$ was assumed to derive Eq. (2.5). However, as shown in Fig. 2-10, the momentum relaxation time cannot be neglected in the case of relatively low channel mobility such as Si. Therefore, combining Eq. (2.3) and (2.4) for general k equation considering the assumption of $2ks \sim \tau^{-1}{}_p$ as follows:

$$k_{\pm} = \frac{2\omega v_0}{2\left(v_0^2 - s^2\right)} + \frac{iv_0\tau_p^{-1}}{2\left(v_0^2 - s^2\right)} \mp \xi\sqrt{1+i\gamma} \tag{2.50}$$

$$\xi = \frac{s\tau^{-1}\sqrt{4\omega^2\tau_p^2 - M^2}}{2\left(v_0^2 - s^2\right)}, \quad \gamma = \frac{4\omega\tau_p}{4\omega^2\tau_p^2 - M^2} \tag{2.51}$$

where $M = s/v_0$ is Mach number.

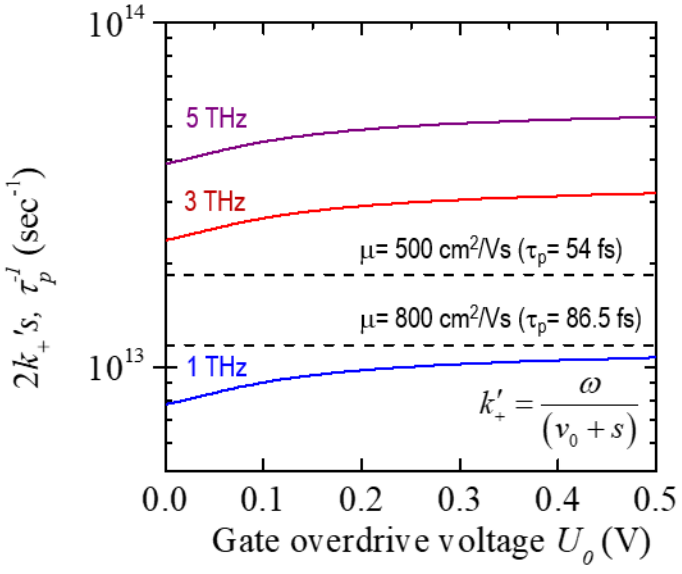

Figure 2-10. $2k'_+s$ vs. U_0 plot assuming strained Si of $m^*/m = 0.19$ for $\mu = 500$, 800 cm²/Vs as channel material of R-PWT. Even though here k'_+ is derived from the ideal assumption of $2ks >> \tau^{-1}{}_p$, newly derived k'_+ considering $2ks \sim \tau^{-1}{}_p$ in Fig. 2-6 shows same trends that the $\tau^{-1}{}_p$ term should not be neglected.

There are two regions by sign of root term in ξ. Firstly, if $2\omega\tau_p > M$,

$$k'_{\pm} = \frac{2\omega v_0}{2\left(v_0^2 - s^2\right)} \mp \xi \,\mathrm{Re}\left[\sqrt{1+i\gamma}\right] \tag{2.52}$$

$$k''_{+} = \frac{v_0 \tau_p^{-1}}{2\left(v_0^2 - s^2\right)} \mp \xi \,\mathrm{Im}\left[\sqrt{1+i\gamma}\right] \tag{2.53}$$

$$\mathrm{Re}\left[\sqrt{1\pm i\gamma}\right] = \sqrt{\frac{1+\sqrt{1+\gamma^2}}{2}}, \quad \mathrm{Im}\left[\sqrt{1\pm i\gamma}\right] = \frac{\gamma}{|\gamma|}\sqrt{\frac{-1+\sqrt{1+\gamma^2}}{2}} \tag{2.54}$$

Secondly, if $2\omega\tau_p < M$,

$$k'_{+} = \frac{2\omega v_0}{2\left(v_0^2 - s^2\right)} \pm \xi_{II} \,\mathrm{Im}\left[\sqrt{1+i\gamma}\right] \tag{2.55}$$

$$k''_{+} = \frac{v_0 \tau_p^{-1}}{2\left(v_0^2 - s^2\right)} \mp \xi_{II} \,\mathrm{Re}\left[\sqrt{1+i\gamma}\right] \tag{2.56}$$

$$\xi = \frac{s\tau^{-1}\sqrt{-\left(M^2 - 4\omega^2\tau^2\right)}}{2\left(v_0^2 - s^2\right)} = i\frac{s\tau^{-1}\sqrt{M^2 - 4\omega^2\tau^2}}{2\left(v_0^2 - s^2\right)} = i\xi_{II} \tag{2.57}$$

where ξ_{II} is defined for the convenience of calculation. Figure 2-11 shows that derived general k equation also placed in $2ks \sim \tau^{-1}{}_p$ region for relatively low frequency that the $\tau^{-1}{}_p$ term should not be neglected.

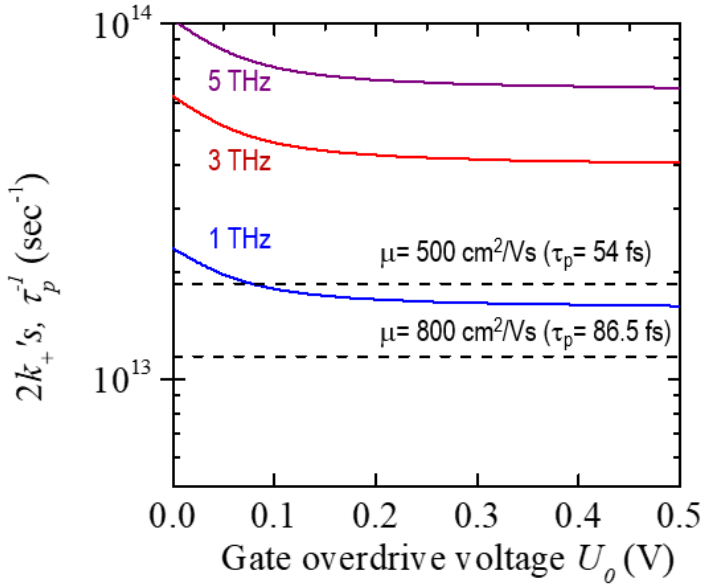

Figure 2-11. $2k'_+s$ vs. U_0 plot used general k'_+ equation assuming strained Si of m^*/m= 0.19 for μ= 500, 800 cm2/Vs as channel material of R-PWT.

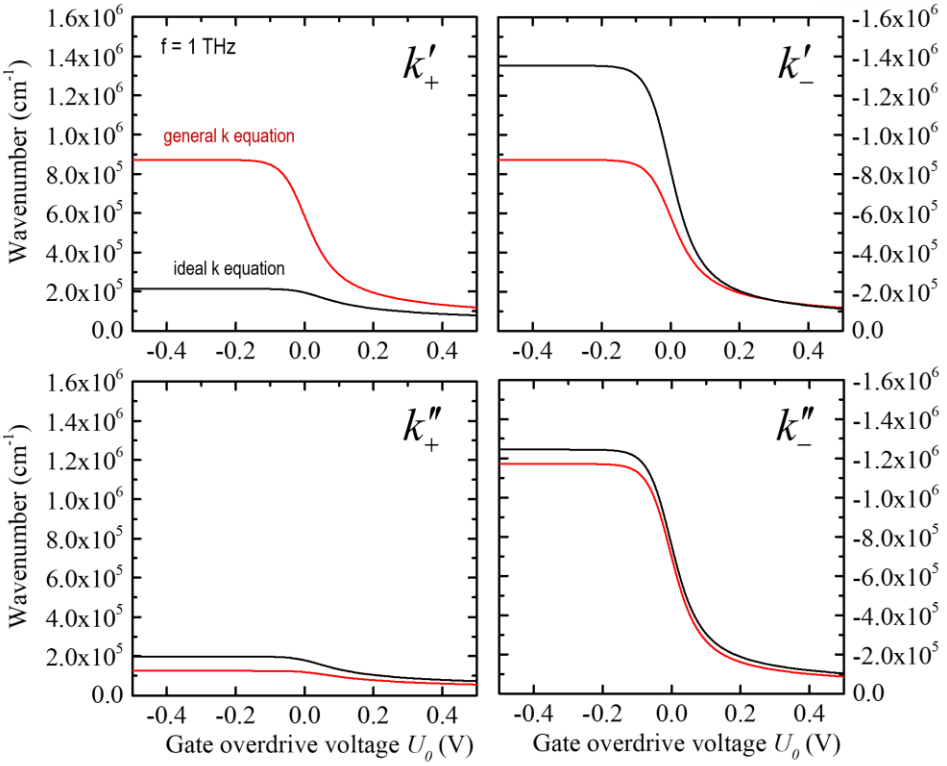

Figure 2-12. general wavenumber equation for assuming strained Si (m^*/m= 0.19, μ= 800 cm^2/Vs, l_{eff}= 20 nm, v_{inj}= 1.23×10^7 cm/s) at f= 1 THz.

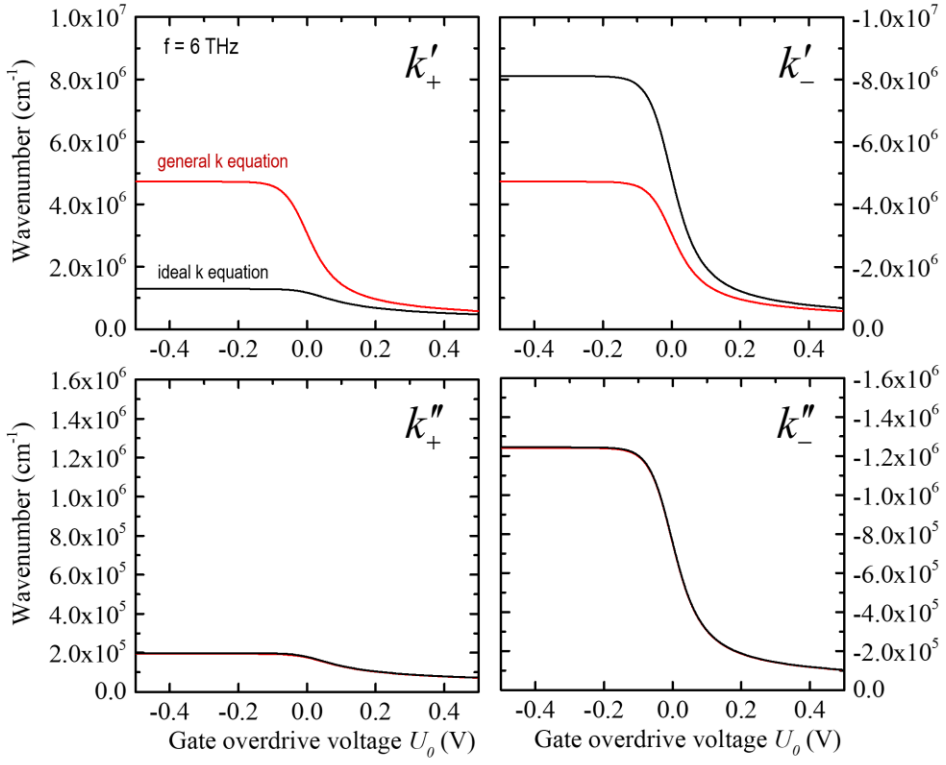

Figure 2-13. general wavenumber equation for assuming strained Si (m^*/m= 0.19, μ= 800 cm^2/Vs, l_{eff}= 20 nm, v_{inj}= 1.23×10^7 cm/s) at f= 6 THz.

Figure 2-12 and 2-13 show that differences between derived general and ideal wavenumber equations. Firstly, the discrepancy between real parts of general and ideal cases become obvious as gate voltage decreases due to decreased plasma-wave velocity in $k'_{\pm}=\omega/(s-v_0)$ for ideal case, which makes drain reflection coefficient ($r_{n,d}= s+v_0/s-v_0$) high. On the contrary, general case shows $|k'_{+}|=|k'_{-}|$ that means imaginary part of wavenumber determines $r_{n,d}.= k_{+}/k_{-}$. Secondly, if we compare Fig 2-12 for f= 1 THz case with Fig 2-13 for f= 6 THz case, it is noticeable that damping term of plasma-wave due to low frequency is included correctly in general case $\exp[-k''_{\pm}x]$ term. Therefore, the ideal k equation can be only used in relatively high frequency in the THz range and high gate voltage having similar $|k'_{+}|=|k'_{-}|$ values.

2.5.4. General resonant V_{out} equation

As discussed in chapter 2.5.2, Veksler et al. have derived V_{out} equation using approximations of $s >> v_0$ and $\omega' \tau_p >> 1$ [52]. Despite this equation well fit into the case for the high mobility materials or high frequency above f= 1 THz, it is necessary to exclude these approximations in order to investigate the materials having relatively low channel mobility or sub-THz regime. The basic idea of derivation process for general V_{out} equation is introduced in Ref. [33]. The resultant V_{out} equation as

$$V_{out} = \frac{m}{e}\left[\frac{1}{2}\left(\left\{\frac{\langle U_1(0)v_1(0)\rangle}{U_0}\right\}^2 - \left\{\frac{\langle U_1(l)v_1(l)\rangle}{U_0}\right\}^2\right) + \left(\frac{\langle v_1^2(0)\rangle - \langle v_1^2(l)\rangle}{2}\right) + \left(\frac{1}{\tau}\int_{x=0}^{x=l}\frac{\langle U_1 v_1\rangle}{U_0}\partial x\right)\right] \quad (2.58)$$

$$\langle v_0\rangle = -\frac{\langle U_1 v_1\rangle}{U_0} \quad (2.59)$$

Each term in Eq. (2.58) are defined as 1st $\langle v_0\rangle^2$, 2nd $\langle v_1^2\rangle$ (2nd term), and 3rd integral $\langle v_0\rangle$ terms in this thesis. Firstly, $\langle v_1^2\rangle$ term will be examined, which is dominant term in the case of $s >> v_0$ and $\omega' \tau_p >> 1$. Here we use general k equations in chapter 2.5.3 in order to shed light on V_{out} near and below threshold voltage. Starting from Eq. (2.48) as

$$v_1 = \mathrm{Re}\left[\left(C_+\frac{\omega - k_+ v_0}{k_+ U}e^{ik_+ x} + C_-\frac{\omega - k_- v_0}{k_- U}e^{ik_- x}\right)e^{-i\omega t}\right]$$

This equation is combined with real and imaginary parts for C, k, and ω so that it is necessary to make v_1= Re[v_1]+Im[v_1] as

$$\frac{\omega - (k_+' + ik_+'')v_0}{(k_+' + ik_+'')U} = \frac{\omega k_+' - k_+'^2 v_0 - k_+''^2 v_0}{(k_+'^2 + k_+''^2)U} - i\frac{\omega k_+''}{(k_+'^2 + k_+''^2)U} = M_+' - iM_+'' \quad (2.60)$$

$$\begin{aligned} C_+\frac{\omega - k_+ v_0}{k_+ U}e^{ik_+ x} &= Q_+' + iQ_+'' = \\ &\left[C_+'M_+'\cos(k_+'x) + C_+''M_+''\cos(k_+'x) - C_+''M_+'\sin(k_+'x) + C_+'M_+''\sin(k_+'x)\right]e^{-k_+''x} \\ &+i\left[C_+'M_+'\sin(k_+'x) + C_+''M_+''\sin(k_+'x) + C_+''M_+'\cos(k_+'x) - C_+'M_+''\cos(k_+'x)\right]e^{-k_+''x} \end{aligned} \quad (2.61)$$

In order to solve $C_{\pm}$, Eq. (2.37) is used as follows,

$$C_{\pm} = \frac{k_{\pm}U_a}{k_{\pm} - k_{\mp}e^{k_{\mp}''l - k_{\pm}''l}e^{i\left(k_{\pm}'l - k_{\mp}'l\right)}} = \frac{k_{\pm}U_a}{c' + ic''} = \frac{U_a\left(k_{\pm}'c_{\pm}' + k_{\pm}''c_{\pm}''\right)}{c_{\pm}'^2 + c_{\pm}''^2} + i\frac{U_a\left(k_{\pm}''c_{\pm}' - k_{\pm}'c_{\pm}''\right)}{c_{\pm}'^2 + c_{\pm}''^2} = C_{\pm}' + iC_{\pm}'' \tag{2.62}$$

$$c_{\pm}' = k_{\pm}' - e^{k_{\mp}''l - k_{\pm}''l}\left[k_{\mp}'\cos\left(k_{\pm}'l - k_{\mp}'l\right) - k_{\mp}''\sin\left(k_{\pm}'l - k_{\mp}'l\right)\right]$$

$$c_{\pm}'' = k_{\pm}'' - e^{k_{\mp}''l - k_{\pm}''l}\left[k_{\mp}'\sin\left(k_{\pm}'l - k_{\mp}'l\right) + k_{\mp}''\cos\left(k_{\pm}'l - k_{\mp}'l\right)\right]$$

Therefore, v_1 for downstream and upstream becomes as

$$v_1 = \left(Q_+' + Q_-'\right)\cos\left(\omega t\right) + \left(Q_+'' + Q_-''\right)\sin\left(\omega t\right) \tag{2.63}$$

Finally, the V_{out} equation considering only $\langle v_1^2 \rangle$ term as

$$V_{out} = \left\langle U\left(l\right)\right\rangle - \left\langle U\left(0\right)\right\rangle = \frac{1}{2}\frac{m}{e}\left[\left\langle v_1\left(0\right)^2\right\rangle - \left\langle v_1\left(l\right)^2\right\rangle\right] \tag{2.64}$$

$$\left\langle v_1^2\left(x\right)\right\rangle = \frac{\left(Q_+'\left(x\right) + Q_-'\left(x\right)\right)^2}{2} + \frac{\left(Q_+''\left(x\right) + Q_-''\left(x\right)\right)^2}{2} \tag{2.65}$$

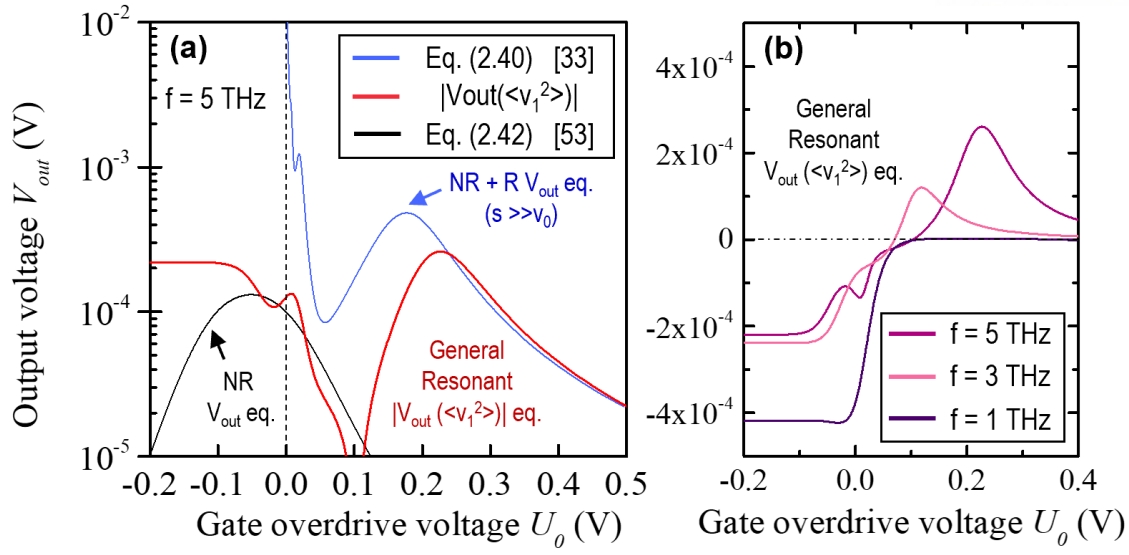

Figure 2-14. V_{out} vs. U_0 plot (a) at f= 5 THz adding Eq. (2.63) newly derived which displays absolute value in order to compare to reported equations (Eq. (40) and (42)). Negative V_{out} is calculated below $U_0 < 0.1$ V. Each equation uses same parameters for clear comparison assuming strained Si R-PWT THz detector (m^*/m= 0.19, μ= 800 cm2/Vs, l_{eff}= 20 nm, $U_a(=V_a)$= 5 mV). (b) Frequency dependence of general resonant V_{out} equation.

Figure 2-14(a) shows that comparison general resonant V_{out} equation using Eq. (2.65) with the reported equations. It is noticeable that there is the shift of resonant peak toward higher gate voltage compared to reported V_{out} equations (Eq. (2.40)), which uses the approximation of $s >> v_0$ ($\omega' = s\pi/2l$), since Eq. (2.65) consider $s \sim v_0$ condition (see Eq. (1)). Also, there is no NR 'peak' appeared on general resonant V_{out} equation, because non-resonant phenomena aren't fully considered in both resonant k and V_{out} equations. Despite W. Knap et al. have demonstrated the NR V_{out} equation (Eq.(2.42) [53]), it is debatable to accept the argument that the reason to form NR peak is due to the gate leakage current. Furthermore, figure 2-14 (b) illustrates that the frequency dependence of V_{out} using only $\langle v_1^2 \rangle$ term. The calculated V_{out} below V_{th} becomes abruptly high and its trend intensify as lowering external THz frequency, since the reflection coefficients at low gate voltage and low frequency are overestimated due to lack of the consideration of non-resonant phenomena, again, whose V_{out} increases and saturates as frequency increased, as mentioned in chapter 1.4 and Fig. 1-3(a). It has been conducting to derive the general V_{out} equation considered both resonant and non-resonant phenomena, which will be briefly dealt in chapter 2.7 as a remaining work to be done.

Next, $\langle v_0 \rangle^2$ and integral $\langle v_0 \rangle$ terms in Eq. (2.58) will be examined. The 1st order of voltage wave U_1 is represented as

$$U_1 = \left(q_+^c + q_-^c\right)\cos(\omega t) + \left(q_+^s + q_-^s\right)\sin(\omega t) \tag{2.66}$$

$$q_\pm^c = \left[C_\pm' \cos\left(k_\pm' x\right) - C_\pm'' \sin\left(k_\pm' x\right)\right] e^{-k_\pm'' x}, \quad q_\pm^s = \left[C_\pm' \sin\left(k_\pm' x\right) + C_\pm'' \cos\left(k_\pm' x\right)\right] e^{-k_\pm'' x}$$

Therefore, the 2nd order of time average for energy flux becomes as

$$\langle U_1 v_1 \rangle = \frac{\left(q_+^c + q_-^c\right)\left(Q_+' + Q_-'\right)}{2} + \frac{\left(q_+^s + q_-^s\right)\left(Q_+'' + Q_-''\right)}{2} \tag{2.67}$$

The resultant integral $\langle v_0 \rangle$ term has complicated form but simple derivation process.

$$\frac{1}{2U_0\tau}\left[\int_{x=0}^{x=l}\left(q_+^c Q_+' + q_+^s Q_+''\right)\partial x + \int_{x=0}^{x=l}\left(q_-^c Q_-' + q_-^s Q_-''\right)\partial x + \int_{x=0}^{x=l}\left(q_-^c Q_+' + q_+^c Q_-' + q_-^s Q_+'' + q_+^s Q_-''\right)\partial x\right] =$$

$$\frac{1}{2U_0\tau}\left[\begin{array}{l} \dfrac{(CM)_c\, e^{-(k_+''+k_-'')l}\left[\left(k_+''-k_-''\right)\sin\left(k_+''l - k_-''l\right) + \left(k_+''+k_-''\right)\left\{e^{(k_+''+k_-'')l} - \cos\left(k_+''l - k_-''l\right)\right\}\right]}{2\left(k_+''^2 + k_-''^2\right)} - \\ \dfrac{(CM)_s\, e^{-(k_+''+k_-'')l}\left[\left(k_+''+k_-''\right)\sin\left(k_+''l - k_-''l\right) - \left(k_+''-k_-''\right)\left\{e^{(k_+''+k_-'')l} - \cos\left(k_+''l - k_-''l\right)\right\}\right]}{2\left(k_+''^2 + k_-''^2\right)} - \\ \dfrac{(CM)_+\left(e^{-2k_+''l} - 1\right)}{2k_+''} - \dfrac{(CM)_-\left(e^{-2k_-''l} - 1\right)}{2k_-''} \end{array}\right] \tag{2.68}$$

$$(CM)_+ = \left[C_+'^2 + C_+''^2\right]M_+', \quad (CM)_- = \left[C_-'^2 + C_-''^2\right]M_-'$$

$$(CM)_c = C_+'C_-'\left[M_+' + M_-'\right] - C_+'C_-''\left[M_+'' - M_-''\right] + C_-'C_+''\left[M_+'' - M_-''\right] + C_+''C_-''\left[M_+' + M_-'\right]$$

$$(CM)_s = C_+'C_-'\left[M_+'' - M_-''\right] + C_+'C_-''\left[M_+' + M_-'\right] - C_-'C_+''\left[M_+' + M_-'\right] + C_+''C_-''\left[M_+'' - M_-''\right]$$

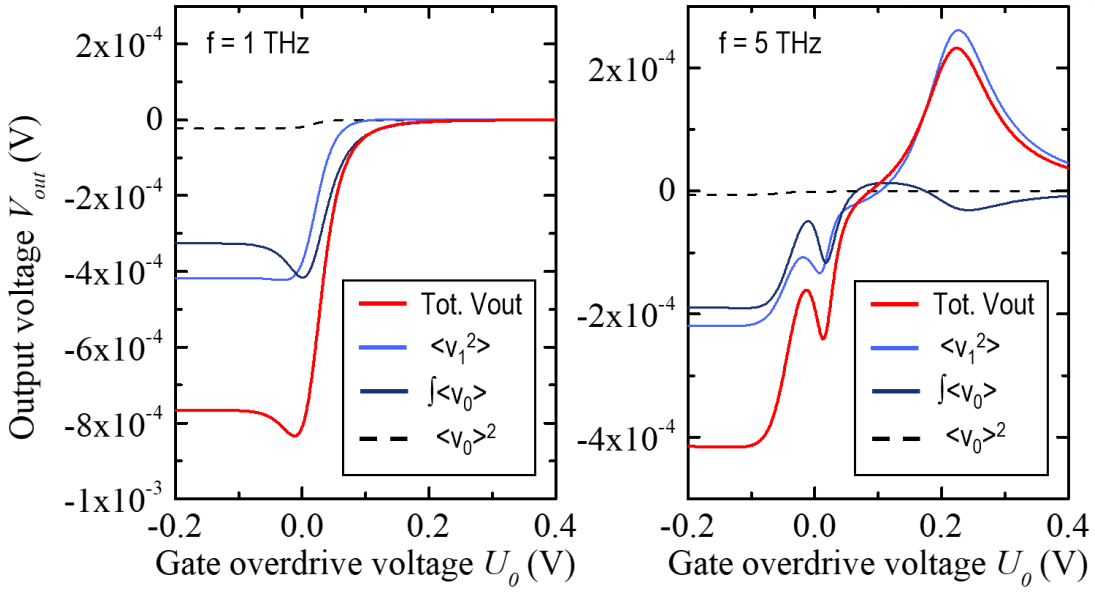

Figure 2-15. V_{out} vs. U_0 plot considering all terms in Eq. (2.58) (a) f= 1 THz and (b) 5 THz, which assumes s-Si R-PWT THz detector using same parameters to Fig. 2-10 (m^*/m= 0.19, μ= 800 cm2/Vs, l_{eff}= 20 nm, U_a= 5 mV).

Figure 2-15 shows that general resonant V_{out} equations containing all terms as in Eq. (2.58). It is obvious that integral $\langle v_0 \rangle$ term is dominant in relatively low 1 THz regime but $\langle v_0 \rangle^2$ term is negligible through whole THz range. It means that it is important to consider both $\langle v_1^2 \rangle$ and integral $\langle v_0 \rangle$ terms in V_{out} equations to investigate the low channel mobility R-PWT showing $s \sim v_0$ tendency.

2.6. Summary

In this chapter, the theoretical analysis of R-PWT have been conducted starting from investigating resonance phenomena in the channel of R-PWT by adopting transmission line theory based on assumptions of infinite drain impedance and zero source impedance as boundary conditions. Next, it has been considered how finite drain impedance influences on the operation of R-PWT in terms of realistic fabrication. Also, the equation of radiation power has been derived to study the practical use of R-PWT as a THz emitter. Even though the expected power has been evaluated in μW scale with wide channel width and considering CVD graphene, it motivates to invent novel device structure, which will be dealt in next section, and it would be the further work to be done by reconstructing power equation and considering other missed parameters or variables that should be contained in the equation for R-PWT. Based on the definition of momentum relaxation time for plasma-wave, finally, the reported V_{out} equations by other research groups have been reviewed to shed light on the points that should be taken into account low channel mobility R-PWT in $s \sim v_0$ regime. As a result, the equations of wavenumber and general resonant V_{out} have been introduced to correct distorted V_{out} value near threshold voltage and would be helpful to analyze short channel R-PWT THz detector. All these theoretical works in this section have aimed to investigate the realization of Si R-PWT having advantages of cost efficiency and high integration (detailed in chapter V), and high-power graphene R-PWD (detailed in chapter III) with design window to check its possibility (detailed in IV).

Chapter III
Theory of floating gate R-PWD with suspended-channel (FG SC-PWD)

3.1. Structural limitation of PWT

The conventional plasma-wave theory has been adopted as a plasma-wave transistor (PWT), which has the 2-dimensional electron gas (2DEG) formed by the gate terminal of the conventional FET structure. Because of that, the PWT has fundamental problem of the electron mobility degradation by the gate field and the surface roughness scattering as well as the diminution of the electron charge density by the gate leakage current through the thin gate oxide. Therefore, it is difficult to observe THz resonant characteristics and the output power is marginal as micro-Watt class although they implemented PWT THz emitter with relatively high mobility FET such as HEMT [51, 54-55]. Besides, when an ideal 2D material like graphene is inserted below the gate as a channel, the original high mobility is significantly deteriorated [56-57], so the implementation of PWT based on conventional FET, whose channel is controlled by the gate, has serious performance limitation as a THz emitter and detector.

Therefore, in this chapter, we are taking an approach away from the conventional transistor operation which forms and controls 2DEG channel by the gate, and propose a new THz plasma-wave device structure where the channel is not controlled by the gate. Through the theoretical verification and an innovative implementation, it is possible to develop a wideband/high-power/high-sensitivity THz plasma-wave device and commercial emitter/camera system.

3.2. Device structure of FG SC-PWD

The original PWT device operation rely on the gate terminal to carry out multiple purposes, which includes inducing the channel, converting channel plasma waves generated by mirror image charge at the gate electrode into TEM mode electromagnetic waves via electric dipole function, etc. The basic idea to overcome the inevitable structural problem of PWT is to make R-PWD which performs same functions of PWT gate terminal by placing floating gate (FG). In this case, the resonance phenomena in FG R-PWD solely follows the ungated 2DEG plasma-wave theory that has been considered as parasitic component analysis of HEMT structure which degrades the performance of the gated 2DEG [38]. In terms of choosing ungated channel material of FG R-PWD, the graphene, which shows ambipolar *I-V* characteristics with high minimum drain current at Dirac point voltage, would be the best candidate with its ultra-high mobility [45]. Furthermore, in order to eliminate mobility degradation originated from band bonding between graphene and insulator, it is efficient to fabricate suspended-channel (SC) structure [58]. Figure 3-1 illustrates the device structure of floating gate R-PWT with suspended channel (FG SC-PWD).

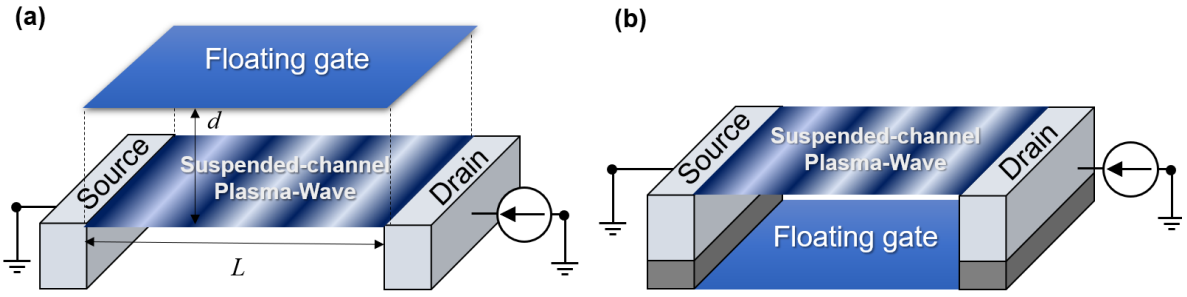

Figure 3-1. Schematic view of FG SC-PWD. The device structure can be chosen by the optimization of fabrication (a) placing floating gate top or (b) bottom.

3.3. Resonance phenomena in FG SC-PWD

After M. Dyakonov and M. Shur have reported the theory of plasma-wave resonance in ungated region [59], M. V. Cheremisin and G. G. Samsonidze have derived V_{out} equation for THz detection with dimensionless units for investigating universal characteristic of ungated plasma-wave [40-41]. In this chapter, it will be reviewed the derivation flow in order to analyze specific channel materials such as graphene with considering finite drain impedance for studying realistic possibility of FG SC-PWD. Also, it will be introduced the reconstruction of k equation represented as real and imaginary parts in order to examine the channel plasma-wave, which is helpful for calculating the radiation power of graphene FG SC-PWD as THz emitter having higher power than R-PWT case. Finally, it will be briefly demonstrated the critical drain impedance ($|Z_{d,c}|$) considering this newly derived wavenumber to analyze the channel material which cannot use the assumptions of $\omega' >> \omega''$ and negligible $i/2\,\tau_p$ condition.

3.3.1. Influence of finite drain impedance on FG SC-PWD

On the structure of FG SC-PWD as shown in Fig. 3-1, plasma-waves ($n_1(x,t)$) are defined as the sum of the downstream (n_{1+}) and upstream (n_{1-}) as follows:

$$n_1(x,t) = n_{1+}(x,t) + n_{1-}(x,t) = \left(C_+ e^{ik_+ x} + C_- e^{ik_- x}\right) e^{-i\omega t} \tag{3.1}$$

where $C_\pm$ is the perturbation coefficient by noise signals, $k_\pm$ is the wave number and ω is the angular frequency. The behaviors of these plasma-waves are governed by the following first order of hydrodynamic Euler equation and continuity equation [59],

$$\frac{\partial v_1}{\partial t} + v_0 \frac{\partial v_1}{\partial x} = -\frac{e}{m}\frac{\partial \Psi_1}{\partial x} \tag{3.2}$$

$$\frac{\partial n_1}{\partial t} + n_0 \frac{\partial v_1}{\partial x} + v_0 \frac{\partial n_1}{\partial x} = 0 \tag{3.3}$$

where e is the elementary electric charge, m is the effective mass, $\Psi = (en_1)/(2k\varepsilon)$ is the self-electric potential, and ε is the 2D channel material permittivity. By combing Eqs. (3.2) with (3.3), it is possible to derive the dispersion relation as follows [59]:

$$\omega = kv_0 \pm \sqrt{\frac{e^2 k n_0}{2m\varepsilon}} \tag{3.4}$$

where n_0 is surface electron concentration. This dispersion relation ($\omega \sim k^{1/2}$) shows that the plasma-waves in the suspended channel act like deep water behaviors. It means that the plasma-wave is dispersive, and its velocity (s) is dependent on the wave number which is given by

$$s_\pm = \frac{\omega}{k} = v_0 \pm \sqrt{\frac{e^2 n_0}{2m\varepsilon k_\pm}} = v_0 \pm \sqrt{\frac{2\alpha}{k_\pm}} \tag{3.5}$$

where α is acceleration of plasma-wave. If we consider momentum relaxation time (τ_p) to explain collision between electrons and phonons or impurities, new term of $-v_1/\tau_p$ is contained in right side of (3.2) and the wave numbers in this case can be derived as follows [40]:

$$k_{\pm} = \pm \frac{1 \pm \frac{v_0}{a}\left(\omega + \frac{i}{2\tau_p}\right) - \sqrt{1 \pm 2\frac{v_0}{a}\left(\omega + \frac{i}{2\tau_p}\right) - \frac{v_0^2}{4\tau_p^2 a^2}}}{v_0^2/a} \tag{3.6}$$

It has been reported the approximated k equations with assumption of $\omega' >> \omega''$, and negligible $i/2\tau_p$ and $(v_0^2/4\tau_p^2 a^2)$ terms as

$$k_{\pm} = \pm \frac{1 \pm \eta' - \sqrt{1 \pm \eta'}}{v_0^2/\alpha} \tag{3.7}$$

where $\eta' = \omega' v_0/\alpha$. Assuming ideal boundary conditions, which means that both ac short and ac open conditions are implemented on source ($|Z_s| = 0$) and drain ($|Z_d| = \infty$), respectively, the oscillatory component of current flux cannot penetrate through drain, which can be described by [32]

$$j_1(L) = \frac{\omega}{k_+} C_+ e^{ik_+ L} + \frac{\omega}{k_-} C_- e^{ik_- L} = 0 \tag{3.8}$$

where L is the channel length. By using (3.8), it is possible to yield real (ω') and imaginary (ω'') part of angular frequency and ideal drain reflection coefficient ($r_{d,i}$) as follows:

$$\omega' = \frac{\alpha}{2v_0}\sqrt{1 - \frac{1}{4}\left\{\left(2 - \frac{v_0^2}{\alpha L} N\pi\right)^2 - 2\right\}^2} \tag{3.9}$$

$$\omega'' = \frac{v_0\sqrt{1-(2\eta)^2}}{\left(\sqrt{1+2\eta} - \sqrt{1-2\eta}\right)L} \ln|r_d| - \frac{1}{2\tau_p} \tag{3.10}$$

$$r_{d,i} = \frac{1 - \eta - \sqrt{1-2\eta}}{1 + \eta - \sqrt{1+2\eta}} \tag{3.11}$$

where N is odd number for plasma-wave harmonics. Because of $n_1 \sim \exp(\omega'' t)$, it is necessary that ω'' should be bigger than zero for making resonance so that r_d should exceed a critical value ($r_{d,c}$), which is given by

$$r_{d,c} = \exp\left[\frac{\left(\sqrt{1+2\eta} - \sqrt{1-2\eta}\right)L}{2\tau_p v_0\sqrt{1-(2\eta)^2}}\right] \tag{3.12}$$

In the case of ideal boundary conditions, $r_{d,c}$ is always smaller than $r_{d,i}$ when the plasma-wave resonance occurs. However, implementing infinite impedance on drain side is hard to be achieved in real case so that it is needed to consider finite drain impedance. In this case, current flux at drain side is not zero anymore and (3.8) changes to the following equation by using Ohm's law

$$\frac{\Psi_1(L)}{|Z_d|W} = e\left(\frac{\omega}{k_+}C_+e^{ik_+L} + \frac{\omega}{k_-}C_-e^{ik_-L}\right) \tag{3.13}$$

where W is the channel width. Here we should consider self-electric potential for the finite size of 2DEG channel as

$$\Psi_1(x) = \frac{e}{2\varepsilon}\left\{\frac{C_+e^{ik_+x} - C_+}{k_+} + \frac{C_-e^{ik_-x} - C_-}{k_-}\right\} \tag{3.14}$$

By using (3.13) and (3.14), it is possible to yield drain reflection coefficient for the finite drain impedance as follows:

$$r_d = r_{d,i} - \frac{r_{d,i}+1}{\left(1-2|Z_d|W\varepsilon\omega\right)e^{ik_+L_g}} \tag{3.15}$$

It can be checked that r_d becomes again $r_{d,i}$, if $|Z_d| = \infty$. Also, the resonance starts to occur if rd=rd,c. Thus, by using (3.12) and (3.15), it is possible to find critical impedance $|Z_{d,c}|$ for FG SC-PWD THz emitter, which is given by

$$|Z_{d,c}| = \left|\frac{1}{2W\varepsilon\omega'}\left\{1 + \frac{r_{d,i}+1}{r_{d,c}-r_{d,i}}\cos k_+L\right\}\right| \tag{3.16}$$

Fig. 3-2 shows that SC-PWD is more acceptable for making THz emitter compared to R-PWT. Assuming graphene as the channel 2D material and the channel length and mobility are same for both of SC-PWD and R-PWT as L= 300 nm and μ= 10^5 cm/Vs, the necessary $|Z_d|$ for FG SC-PWD is much less than R-PWT case, which is about 500 Ω at 10 THz. If we consider that reported channel mobility of R-PWT is usually low (assuming μ= 7000 cm/Vs) so that the channel length should be shorter (assuming L= 30 nm), necessary $|Z_d|$ of FG SC-PWD is lower than of R-PWT case for all operation frequency range.

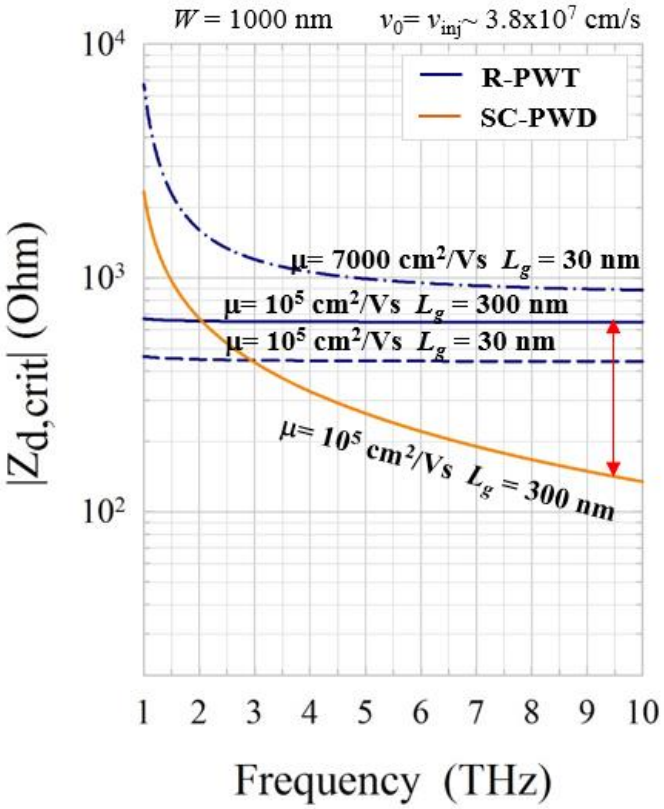

Figure 3-2. $|Z_{d,c}|$ vs. frequency plot assuming v_0=3.81×10^7 cm/s and W= 1000 nm.

3.3.2. Radiation power of FG SC-PWD

The reported k equation of Eq.(3.7), which is represented only as real part, uses too much approximation so that the calculated reflection coefficient at drain side (r_d) always becomes unity, despite the actual r_d is higher than it. Therefore, it is necessary to derive k equation consisting of real and imaginary parts. The derivation process starts from only using the assumption of negligible ($v_0^2/4\,\tau_p^2 a^2$) term in Eq. (3.6).

$$k_{\pm} = \pm \frac{1 \pm \frac{v_0}{a}\left(\omega + \frac{i}{2\tau_p}\right) - \sqrt{1 \pm 2\frac{v_0}{a}\left(\omega + \frac{i}{2\tau_p}\right)}}{v_0^2/a} \tag{3.17}$$

By using series expansion, the resultant $k = k' + ik''$ equation as

$$k_{\pm} = \pm \frac{1 \pm \eta' - \sqrt{1 \pm 2\eta'}}{v_0^2/\alpha}, \quad k''_{\pm} = \frac{\eta'' + \frac{\chi}{2} - \frac{2\eta'' + \chi}{2\sqrt{1 \pm 2\eta'}}}{v_0^2/\alpha} \tag{3.18}$$

$$\eta' = \frac{\omega' v_0}{\alpha} \quad \eta'' = \frac{\omega'' v_0}{\alpha} \quad \chi = \frac{v_0}{\tau\alpha} \quad \alpha = \frac{e^2 n_0}{4m\varepsilon}$$

In order to investigate the radiation power of R-PWD, it is important to consider the correct resonant plasma-wave behavior in the channel. Figure 3-3 illustrates that the resonance phenomenon is well defined in FG SC-PWD by using the newly derived k equations of Eq. (3.17) compared to reported k equations of Eq. (3.7)

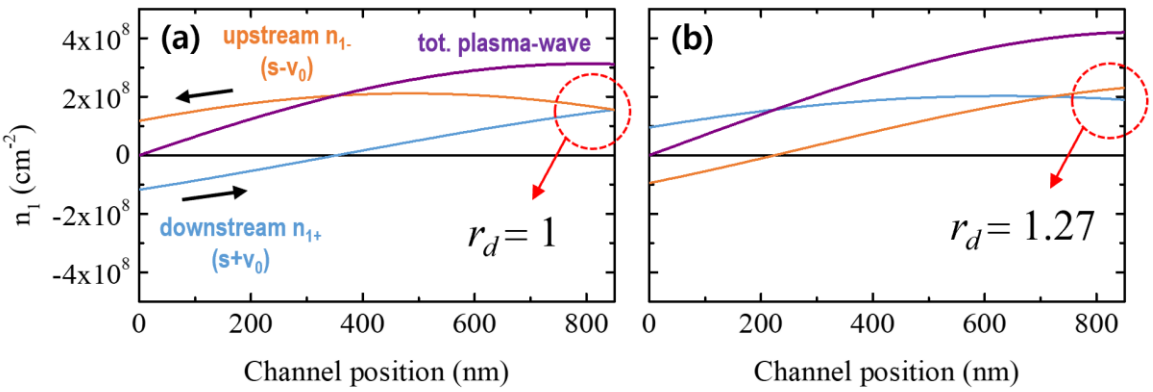

Figure 3-3. Plasma-wave behavior in the channel of FG SC-PWD for (a) using approximation of $\omega' \gg \omega''$, and negligible $i/2\,\tau_p$ and ($v_0^2/4\tau_p^2 a^2$) terms and (b) assuming only negligible ($v_0^2/4\tau_p^2 a^2$) term.

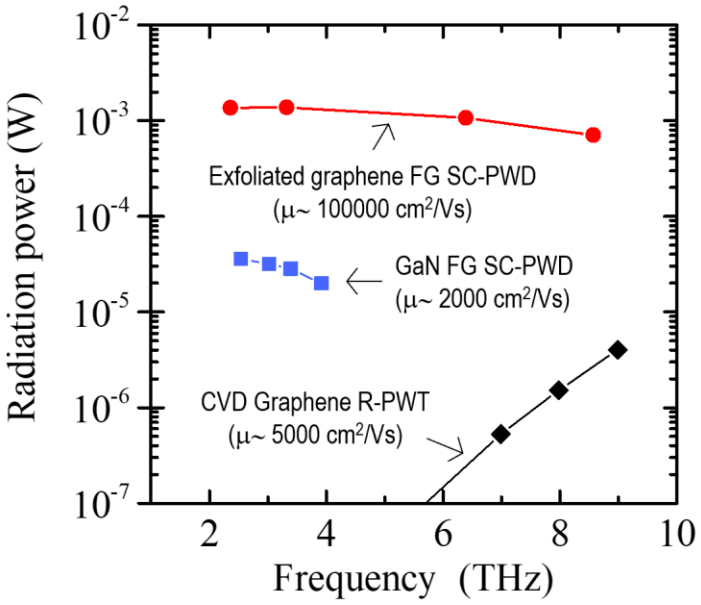

Figure 3-4. The preliminary calculation results of radiation power for FG SC-PWD assuming d=200 nm and R-PWT for graphene and GaN, which has same channel width W= 10 μm. The exfoliated graphene FG SC-PWDs are assumed to have channel lengths 20/100/400/800 nm and 20/30/40/60 nm for GaN case. Each device has the limitation of maximum channel length as THz emitter, which are 865 nm for exfoliated graphene and 69 nm for GaN, respectively. The detailed explanation of maximum channel length will be discussed in chapter IV.

The emission of THz EM wave from FG SC-PWD has same mechanism to R-PWT so that it is possible to evaluate its radiated power by using Eqs. (2.28) and (3.18). In the case of FG SC-PWD, there is no biasing gate voltage which means that each device characterized with its channel length has narrow operation frequency regime, or it is necessary to use additional back-gate voltage. The calculation results of radiation power in Fig 3-4 are carried out using various channel length for each channel material. If exfoliated graphene is used as channel of FG SC-PWD, the emitted THz EM wave shows mW scale through whole THz regime, which is sufficiently applicable to various THz technology and ~100 times higher than of CVD graphene R-PWT case. It should be noticed that even GaN having relatively low mobility can emit THz EM wave with 10 μW scale. The radiation power of FG SC-PWD decreases as frequency increases, since shorter channel length has higher resonance frequency and contains less electrons in the channel area. Also, if CVD graphene FG SC-PWD is considered, the evaluated power is 10 μW scale with l=30 nm, W= 8 μm, d= 10 nm, and emission frequency f= 10 THz. However, the power equation of FG SC-PWD does not fully consider the distance between channel and gate, it is necessary to find optimized distance for FG SC-PWD as a further work.

Additionally, it is possible to define the ideal reflection coefficient ($r_{d,i}$) by using Eq. (3.18) as

$$r_{d,i} = -\frac{k_-}{k_+} = -\left\{ \frac{k'_+k'_- + k''_+k''_-}{k'^2_+ + k''^2_+} + i\left(\frac{k'_+k''_- + k''_+k'_-}{k'^2_+ + k''^2_+} \right) \right\} = -\left[r'_{d,i} + r''_{d,i} \right] \tag{3.19}$$

Because of $r_{d,i} = -[r'_{d,i} + r''_{d,i}]$ and $k = k' + ik''$, it is necessary to rearrange Eq. (3.15) to real and imaginary part as

$$r_d = r'_{d,i} - \left(1 - r'_{d,i}\right)\left\{ \frac{\zeta\omega''\sin\left(k'_+l\right) + \left[1 - \zeta\omega'\right]\cos\left(k'_+l\right)}{\left[\left(1 - \zeta\omega'\right)^2 + \left(\zeta\omega''\right)^2\right]e^{-k''_+l}} \right\} - r''_{d,i}\frac{\zeta\omega''\cos\left(k'_+l\right) - \left[1 - \zeta\omega'\right]\sin\left(k'_+l\right)}{\left(1 - \zeta\omega'\right)^2 + \left(\zeta\omega''\right)^2}e^{k''_+l} \tag{3.20}$$

where $\zeta = 2|Z_d|W\varepsilon$. It can be checked that r_d becomes again $r_{d,i}$, if $|Z_d| = \infty$. By using Eq. (3.20) it is possible to derive $r_{d,c}$ with the condition of $\omega'' = 0$ as

$$r_{d,c} = r'_{d,i} - \frac{\left(1 - r'_{d,i}\right)\cos\left(k'_+l\right)}{1 - \zeta\omega'}e^{k''_+l} + \frac{r''_{d,i}\sin\left(k'_+l\right)}{1 - \zeta\omega'}e^{k''_+l} \tag{3.21}$$

Also, the resonance starts to occur if $r_d = r_{d,c}$. Thus, by using (3.19) and (3.20), it is possible to find critical impedance $|Z_{d,c}|$ for FG SC-PWD THz emitter, which is given by

$$\left|Z_{d,c}\right| = \frac{1}{2W\varepsilon\omega'}\left[1 + \frac{\left[\left(1 - r'_{d,i}\right)\cos\left(k'_+l\right) - r''_{d,i}\sin\left(k'_+l\right)\right]}{r_{d,c} - r'_{d,i}}e^{k''_+l} \right] \tag{3.22}$$

This definition of critical impedance makes it possible to analyze FG SC-PWD more accurately. In the case of exfoliated graphene having ultra-high mobility, there is no serious differences between precise $|Z_{d,c}|$ (Eq. 3.22)) and more approximated $|Z_{d,c}|$ (Eq. (3.16)). However, this result will be helpful for researchers to investigate ungated plasma-wave phenomena in the low mobility channel.

3.4. Summary

In this chapter, it has been shed light on the novel device structure of floating gate R-PWD with suspended channel (FG SC-PWD) required to make a breakthrough the structural limitation of R-PWT. Its theoretical analysis has been conducted based on the ungated plasma-wave theory, which have been originally considered as parasitic component in HEMT structure. To verifying its practical and realistic feasibility, the finite drain impedance have been considered on FG SC-PWD by using same deriving procedure to R-PWT case and its resultant analysis have been shown that FG SC-PWD has advantages of lower critical drain impedance to occur resonance as frequency increases compared to R-PWT due to its property of dispersive wave. Moreover, the estimated radiation power has been evaluated to attain to ~mW scale in the case of exfoliated graphene case with its ultra-high channel mobility and ~ 10 μW scale for CVD graphene case. As a further work, it is necessary to find optimized distance between channel and floating gate which should be contained in the power equation of FG SC-PWD to exclude overestimation of radiated power.

Chapter IV
Design window of R-PWD

4.1. Introduction

After R-PWT has been introduced by M. Dyakonov and M. Shur [29], the theory of R-PWT has been investigated only for basic operation principle and ideal case based on impractical framework. These tendencies cause that Si, which has advantages of cost efficiency and high integration based on nano-CMOS technology, has not been considered as the channel material of R-PWT due to its low mobility. In this chapter, we introduce practical design windows to explain the possibility of R-PWD with its operation frequency and expected role as THz detector or emitter, and even non-resonant detector for various channel materials.

4.2. Design window of R-PWT

4.2.1. R-PWT Design window based on physical conditions

In order to conduct theoretical evaluation of R-PWT, the design window of 2D s-v_0 plot, which has two independent variables of s from plasma-wave theory and v_0 from FET theory in each axis, should be considered because s and v_0 in the comparable range decide the operation frequency of PWT with given channel length. On this s-v_0 plot, it is possible to draw the resonance window by using physical conditions in Table I with fixed L and the parameters related to the channel materials such as μ, m, τ_p. For each underdamped, reflection, increment, and frequency conditions make the line equations as

$$s = \frac{4L}{2\pi\tau_p\left|1-M^2\right|} \quad \text{(underdamped)} \tag{4.1}$$

$$s = v_0 + \frac{L}{\tau_p} \quad \text{(reflection)} \tag{4.2}$$

$$s = \left(\tau_p\left|1-M^2\right|\ln\left|\frac{1+M}{1-M}\right|\right)^{-1} L \quad \text{(increment)} \tag{4.3}$$

$$s = (1\times10^{13})\frac{4L}{\left|1-M^2\right|} \quad \text{(frequency)} \tag{4.4}$$

where $M = v_0/s$ is Mach number. Figure 4-1 shows the basic composition of design window, which assumes $m = 0.028m_0$ and $\mu = 6300\ \mathrm{cm^2\cdot V^{-1}\cdot s^{-1}}$ ($\tau_p = 100$ fs). In this example, it is expected that the R-PWT ($L = 50$ nm) fabricated by these parameters has operation ranges as THz emitter of $7.74\times10^7 < s < 2.05\times10^8$ cm/s and $2.72\times10^7 < v_0 < v_{inj} = 3.22\times10^7$ cm/s at $T = 300$ K with the operation frequency range $3.4 < f < 10$ THz. It should be noticed that the physical condition of plasma-wave reflection $(s-v_0)\tau_p/L > 1$ is considered on the design window. Most of the previous theoretical works by other research groups have focused only on the ideal case of $s >> v_0$, which makes reflection condition to be negligible $s = L/\tau_p$ on the design window. In the comparable $s \sim v_0$ range, however, the reflection condition of Eq. (4.2) should be included for more precise evaluation of R-PWT THz emitter having quasi-ballistic channel because Eq. (4.2) in s-v_0 plot with unity slope is always located above $\omega'\tau_p = 1$.

TABLE I. PHYSICAL CONDITIONS FOR RESONANT PWT THZ EMITTERS

Physical Condition for Plasma-wave	Criteria
Underdamped	$\omega\tau_p > 1$
Reflection	$(s-v_0)\tau_p/L > 1$
Instability	$v_0 < v_{inj} < s$
Increment	$\omega'' > 0$
Frequency	$f < 10$ THz

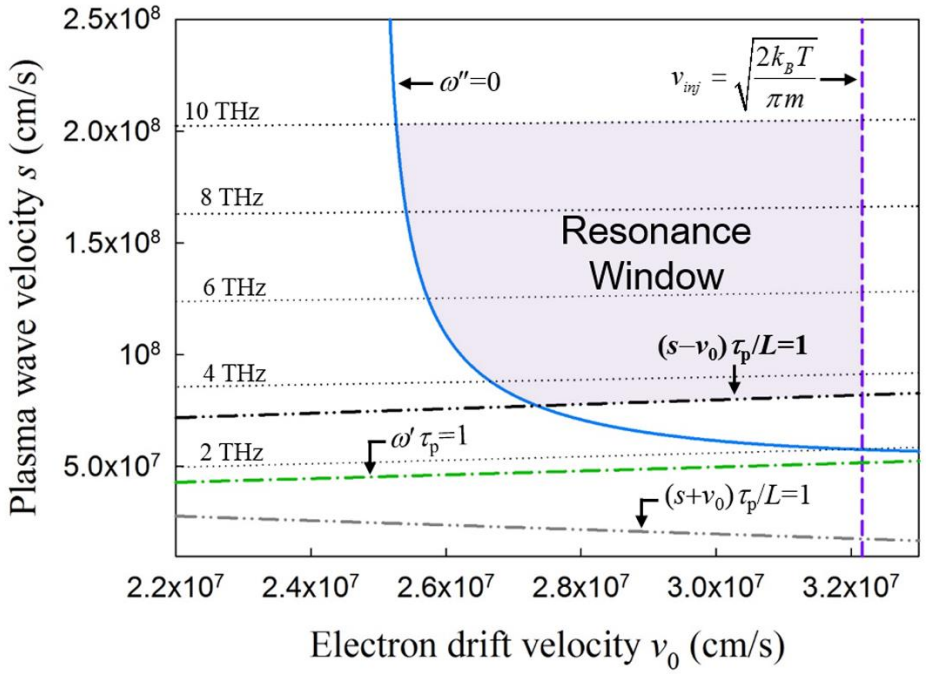

Figure 4-1. PWT resonance window assuming $L = 50$ nm and $\tau_p = 100$ fs by applying the reflection condition of $(s\text{-}v_0)\tau_p/L > 1$, which result in the reduction of tunable operation frequency range. Every point in this $s\text{-}v_0$ plot can be represented by Mach number $M = v_0/s$.

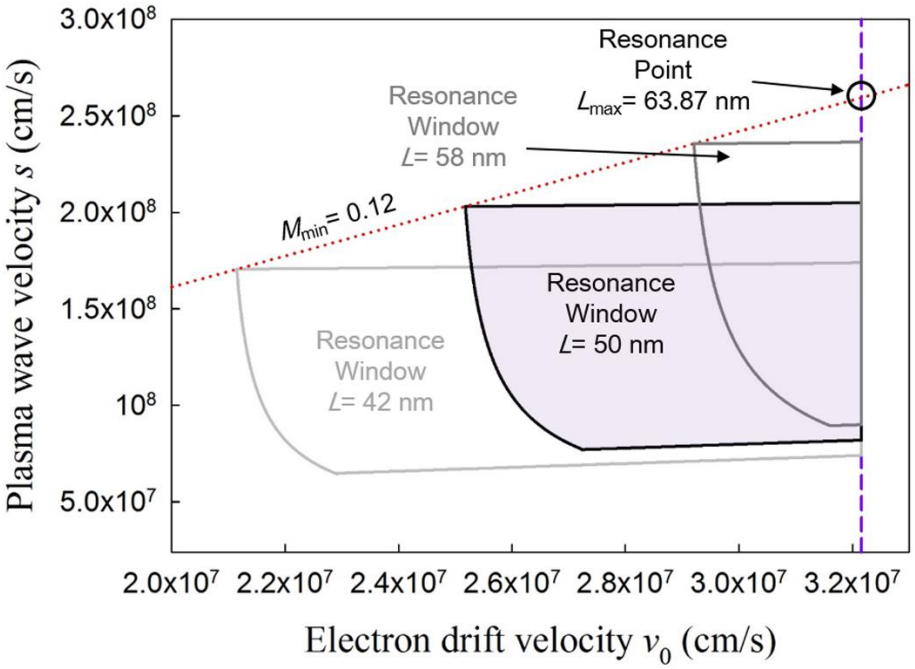

Figure 4-2. PWT resonance windows assuming τ_p= 100 fs for L= 42, 50, and 58 nm. Each resonance window has the same M_{min} and L_{max} is determined as 64 nm at the point of v_0= v_{inj} and s= s_{max} for 10 THz.

To apply Eq. (4.2) onto the s-v_0 plot, the proper estimation of possible L, which is the critical dimension of PWT design, should be conducted based on the maximum channel length (L_{max}) as defined by

$$L_{max} = \frac{s_{max}\left|1 - M_{min}^2\right|}{4\times10^{13}} \tag{4.5}$$

$$M_{min} = \frac{\exp\left(4\tau_p \times 10^{13}\right)^{-1} - 1}{\exp\left(4\tau_p \times 10^{13}\right)^{-1} + 1} \tag{4.6}$$

where s_{max}= v_{inj}/M_{min} [30]. Figure 4-2 shows that the resonance windows is reduced with same M_{min} as L increases and L_{max} is decided at the resonance point of v_0= v_{inj} and s= s_{max} for 10 THz, which is the maximum frequency of so-called "THz gap". It is noticeable that this arbitrarily assumed PWT with τ_p= 100 fs and m= 0.028m_0 can operates as the THz emitters only if the channel length is shorter than L_{max}= 64 nm. By using the concept of maximum channel length, we can calculate feasible $L < L_{max}$ from experiments of FETs with τ_p and m for THz emitter operation.

The evaluated results of L_{max} are summarized in Table II for Si-compatible (Si, Ge and strained Si) or compound semiconductor (InAs, GaAs, and InGaAs) channel materials in MOSFET [60-65] and HEMT structures [66-68]. As listed in Table II, HEMT structure has higher channel mobility than MOSFET on the same material because of the suppression of surface roughness scattering. In case of InGaAs HEMTs [66-67], L_{max} ranges around 170 nm on average which can explain the experimental data of 2.9 THz emission from 130-nm InGaAs HEMT [69]. Focusing on the s-Si channel MOSFET [65] and n-type modulation-doped FET (n-MODFET) [68] where L_{max} increases up to 40 nm, resonant PWT operation for THz emitters can be expected with a current deca-nanoscale Si CMOS technology.

TABLE II. CALCULATION RESULTS OF L_{MAX} FOR VARIOUS CHANNEL MATERIALS IN MOSFET AND HEMT STRUCTURES.

Material [MOSFET]	**μ (cm^2/Vs)**	**m/m_0**	**L_{max} (nm)**
InAs	10500 [60]	0.023	96.94
$In_{0.53}Ga_{0.47}As$	6600 [61]	0.045	85.40
GaAs	4500 [62]	0.063	68.87
Ge	1100 [63]	0.12	22.90
strained Si (s-Si)	500 [64]	0.19	12.87
Si	250 [65]	0.26	7.24
Material [HEMT]	**μ (cm^2/Vs)**	**m/m_0**	**L_{max} (nm)**
InAs	13000 [66]	0.023	120.26
$In_{0.53}Ga_{0.47}As$	9500 [66]	0.045	123.15
	16500 [67]	0.045	214.15
strained Si (s-Si)	1500 [68]	0.19	39.87
	1000 [68]	0.19	26.45

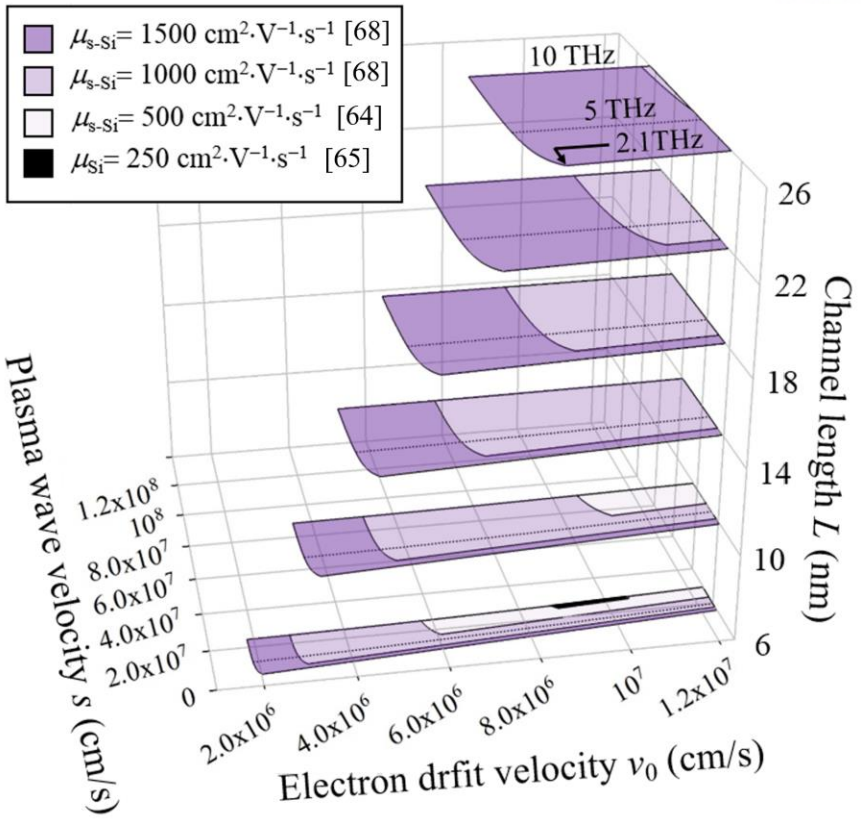

Figure 4-3. Si and strained-Si resonance windows on 3D plot by assigning L to z-axis. The minimum operation frequency range for the $\mu_{s\text{-}Si}$= 1500 cm²·V⁻¹·s⁻¹ is near 2.1 THz at L= 26 nm, where the reflection condition $(s\text{-}v_0)\tau_p/L$ forms boundary of resonant window.

For a comparison of the evaluated resonance windows from Si-compatible PWTs with deca-nanoscale L shorter than L_{max}, the channel length can be assigned to the additional z-axis based on the 2-D s-v_0 plot. Figure 4-3 illustrates the 3D plot of R-PWT resonance windows based on Si-compatible channel under each given channel length of 6, 10, 14, 18, 22, and 26 nm (z-axis). By enhancing channel mobility, larger resonance window is obtained only when given $L < L_{max}$. In case of L=26 nm, s-Si n-MODFET (one of the HEMTs) with μ= 1500 cm²·V⁻¹·s⁻¹ only shows the possible resonance window with a wide operation frequency range of 2.1 THz < f < 10 THz. Based on the lighter effective mass consideration of s-Si as m= 0.19m_0, the boundary of v_{inj} a little bit more increased than Si (m= 0.26m_0) as demonstrated in the case of L= 6 nm where conventional Si MOSFETs with μ= 250 cm²·V⁻¹·s⁻¹ show very difficult to obtain resonance window.

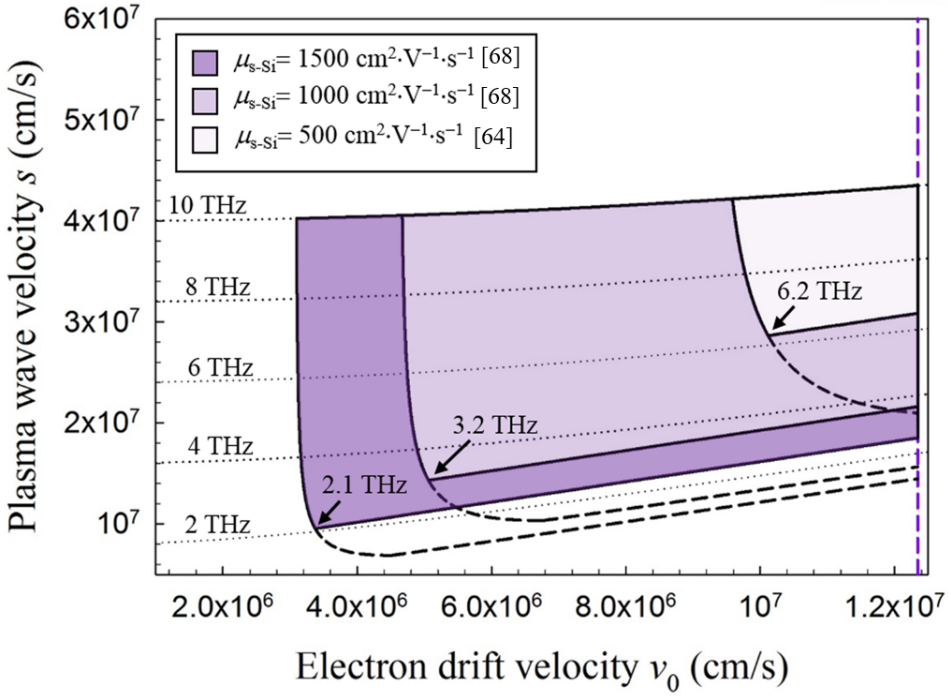

Figure 4-4. R-PWT 2D design window for emission assuming s-Si MOSFET and HEMT structures having L= 10 nm.

It should be noted that, with enhanced channel mobility, the resonance window broadens in the lower left direction at the same channel length as shown in Fig. 4-4, which shows the resonant windows for s-Si PWTs at L= 10 nm. Qualitatively, enhanced mobility (i.e. increased τ_p) of the channel of R-PWT means more underdamped, reflection and increment of plasma-waves, which guarantees that rare scattering events maintain its amplitude and propagation distance further so that the resonance occurs with slower v_0 and s at given L. For quantitative results, in s-Si HEMT with μ= 1500 cm²·V⁻¹·s⁻¹ and L= 10 nm, the resonant PWT can be operated within the range of $9.55\times10^6 < s < 4.35\times10^7$ cm/s and $3.10\times10^6 < v_0 < 1.23\times10^7$ cm/s in the frequency range of $2.1 < f < 10$ THz, which is broader than s-Si MOSFET with μ= 500 cm²·V⁻¹·s⁻¹ case ($2.87\times10^7 < s < 4.35\times10^7$ cm/s and $9.59\times10^6 < v_0 < 1.23\times10^7$ cm/s in the operation frequency range of $6.2 < f < 10$ THz). The dashed lines in Fig. 4-4 are boundaries by only considering increment ($\omega'' > 0$) and underdamped ($\omega'\tau_p > 1$) condition without the reflection condition ($(s-v_0)\tau_p/L > 1$). When the PWT channels become more diffusive and $s \sim v_0$ ranges are comparable, the $(s-v_0)\tau_p/L > 1$ condition should be included for more accurate and realistic design of PWT THz emitters because the operation frequency range is modulated.

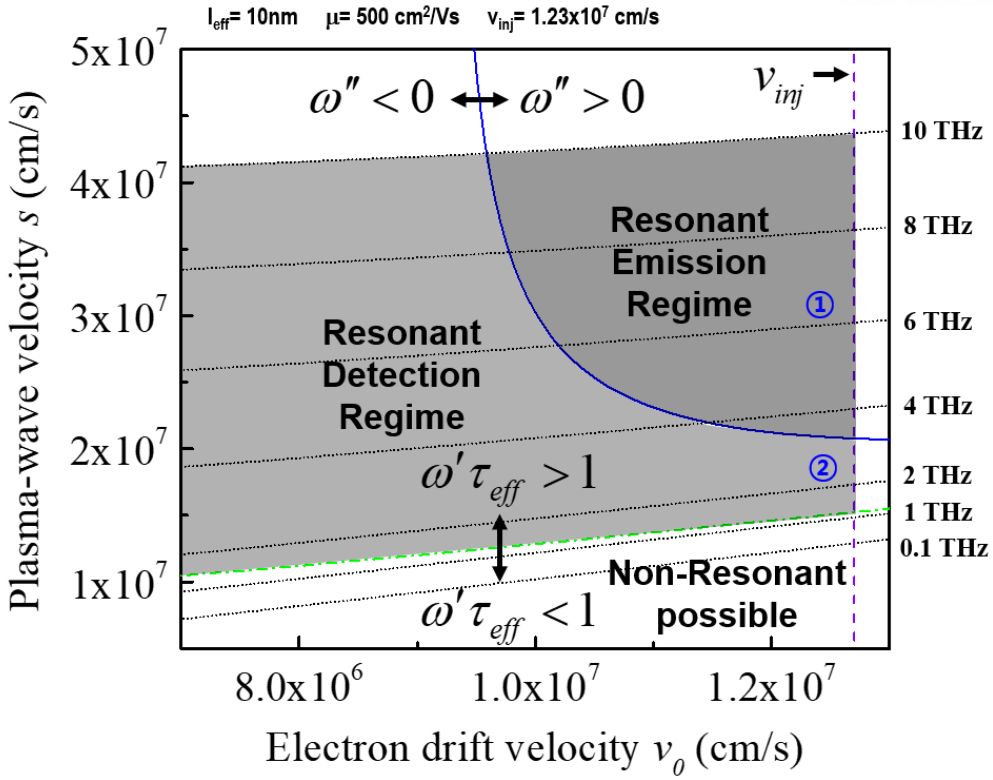

Figure 4-5. R-PWT 2D design window for detector and emitter assuming s-Si MOSFET having L= 10 nm.

Also, if we consider the quality factor for resonant THz detection, $Q = \omega' \tau_{eff} > 1$, it is possible to judge whether the R-PWT can be used as resonant THz detector. These criteria of resonant detection can be included in the design window as shown in Fig. 4-5. If there is no external THz signal, plasma-wave resonance occurs only in $\omega'' > 0$ region, as explained previously. This new physical condition to explain degradation of plasma-wave amplitude can be represented as

$$s = \frac{1}{\tau_p}\left[\frac{\left|1-M^2\right|}{2L} N\pi + \frac{(1-M^2)}{L} \ln\left|\frac{1+M}{1-M}\right|\right]^{-1} \tag{4.7}$$

It is noteworthy that the non-resonant regime at low frequency is also displayed on the design window, which is discussed in previous chapters.

4.2.2. Consideration of source injection velocity

The carrier transport model, which explains the behavior of electrons composed into plasma-wave in the channel, should be considered for analyzing R-PWT properly. In the PWT theory, the source injection velocity (v_{inj}) of electrons is assumed as maximum value of v_0, as discussed in chapter 4.2.1. It is possible to attain to its maximum when no backscattering is achieved (i.e. ballistic carrier transport) [70]. In semiconductor physics, the value of v_{inj} can be changed in the degenerate 2DEG, which is dependent on the electron concentration understood by Fermi-Dirac distribution. In this case, the band diagram of MOSFET, especially in strong inversion, should be considered (i.e. $\psi_s > 2\phi_F$, where ψ_s is the surface potential and ϕ_F is bulk Fermi potential). The source injection velocity in the degenerate 2DEG can be represented as [70]

$$v_{inj} = v_{inj}^{*}\frac{F_{1/2}(\eta_F)}{F_0(\eta_F)} = \sqrt{\frac{2k_BT}{\pi m}}\frac{F_{1/2}(\eta_F)}{\ln\left(1+e^{\eta_F}\right)} \tag{4.8}$$

where $F_j(\eta_F)$ is the Fermi-Dirac integral of order j, $\eta_F = \{E_F - \varepsilon_1(0)\}/k_BT$, $\varepsilon_1(0) = (h^2z^2)/(8mt_{si})$ is the first sub-band energy at oxide-channel interface, h is plank constant, z is integer and $t_{s\text{-}Si}$ is thickness of strained silicon (s-Si) layer. In order to solve the $F_{1/2}(\eta_F)$ term, it is required to use approximated equation, as follows [71]:

$$F_{1/2}(\eta_F) \simeq [e^{-\eta_F} + \xi(\eta_F)]^{-1} \tag{4.9}$$

$$\xi(\eta_F) = 3\sqrt{\pi/2}[(\eta_F + 2.13) + (|\eta_F - 2.13|^{2.4} + 9.6)^{5/12}]^{-3/2} \tag{4.10}$$

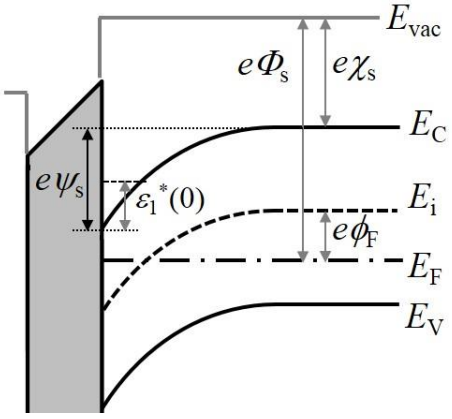

Figure 4-6. MOSFET band diagram considering starting point of strong inversion $\psi_s = 2\phi_F$.

As illustrated in Fig. 4-6, η_F can be defined as

$$\eta_F(\psi_s) = \frac{\{e\psi_s - (e\Phi_s - e\chi_s)\} - \varepsilon_1(0)}{k_B T} \tag{4.11}$$

where Φ_s is a work function, χ_s is an electron affinity of semiconductor. All parameters in Eq. (4.11) has values for specific channel materials except surface potential which is important variable because ψ_s decides source injection velocity and channel electron concentration as [72]

$$n_0 = \frac{m_{de} k_B T}{\pi \hbar^2} F_0(\eta_F) \simeq \frac{C_{ox} U_0}{e} \tag{4.12}$$

where m_{de} is DoS effective mass of electron and $\hbar$ is Dirac constant. By using Eq. (4.12), it is feasible to illustrate v_{inj} as a function of n_0 as shown in Fig. 4-7 (a). In the Boltzmann limit [E_F-$\varepsilon_1(0) << 0$], $F_j(\eta_F)$ changes to simple $e^{\eta F}$ so that constant v_{inj} is obtained (v_{inj}^*).

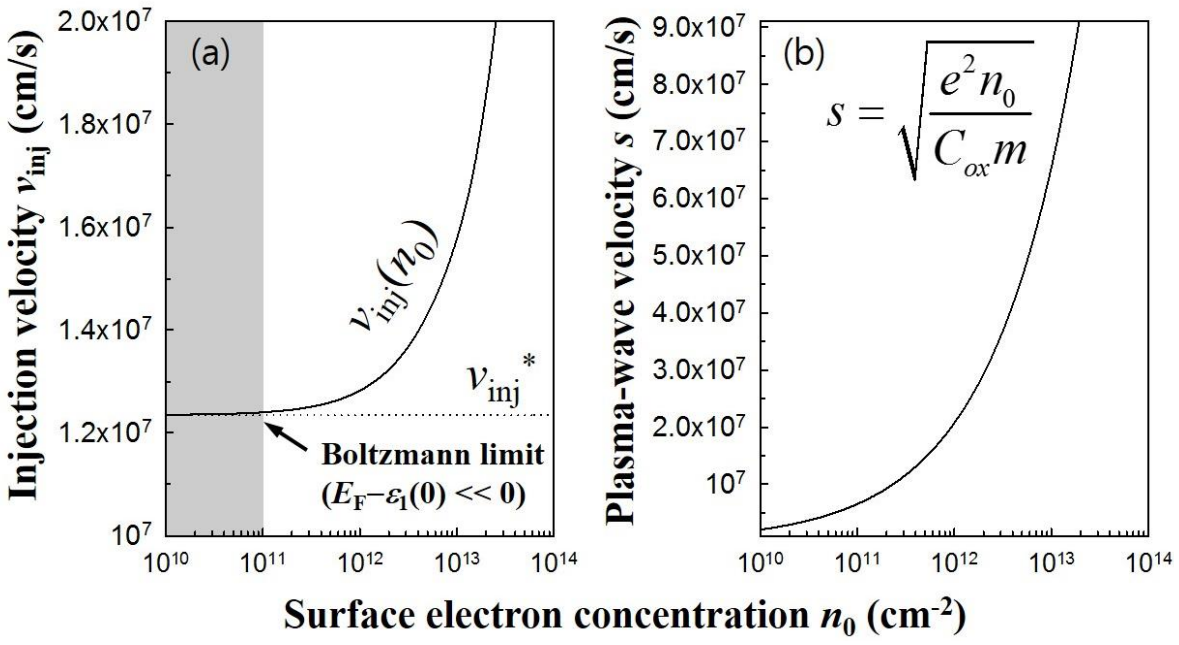

Figure 4-7. (a) Plot of v_{inj} as a function of n_0. The dashed line shows constant v_{inj}^* in the Boltzmann limit and (b) of s as a function of n_0 for the s-Si case (E_g= 0.89 eV, $e\chi_s$= 4.03 eV, $e\Phi_s$= 4.726 eV, $e\phi_F$= 0.252 eV, m_{de}= 0.82m_0, m_{dh}= 0.76m_0, m= 0.19m_0, ε_s= 14.3ε_0 and ultrathin oxide t_{ox}= 1 nm are used)

As deviating the Boltzmann limit, though, the degenerate 2DEG also exhibits a significant deviation from a non-degenerate Maxwellian case and v_{inj} begins to increase as a function of $n_0 > 10^{11}$ cm^{-2}. Because s is also varied by n_0 with the relation of Eq. (4.12), as shown in Fig. 4-7 (b), the increment of v_{inj} shows the strong dependency of plasma-wave velocity as shown in Fig. 4-8.

Figure 4-8 (a) and (b) illustrates the rapid increment of source injection velocity with thin oxide and high oxide permittivity (ε_{ox}). That's because the degenerate 2DEG is more easily created for relatively smaller $U_0(\psi_s)$ (i.e., relatively smaller s) and thinner oxide with higher ε_{ox}. Moreover, there is a reverse-proportional relation between v_{inj} and DoS effective mass [see Fig. 4-8 (c)]. For example, GaAs (m_{de}= $0.067m_0$, m_{dh}= $0.47m_0$) and Ge (m_{de}= $0.56m_0$, m_{dh}= $0.29m_0$), which has lighter $m_{de,dh}$ compared to Si case (m_{de}= $1.08m_0$, m_{dh}= $0.81m_0$), have higher v_{inj} for the same s. Finally, it should be noted that doping concentration in the substrate can be neglected as illustrated in Fig. 4-8 (d).

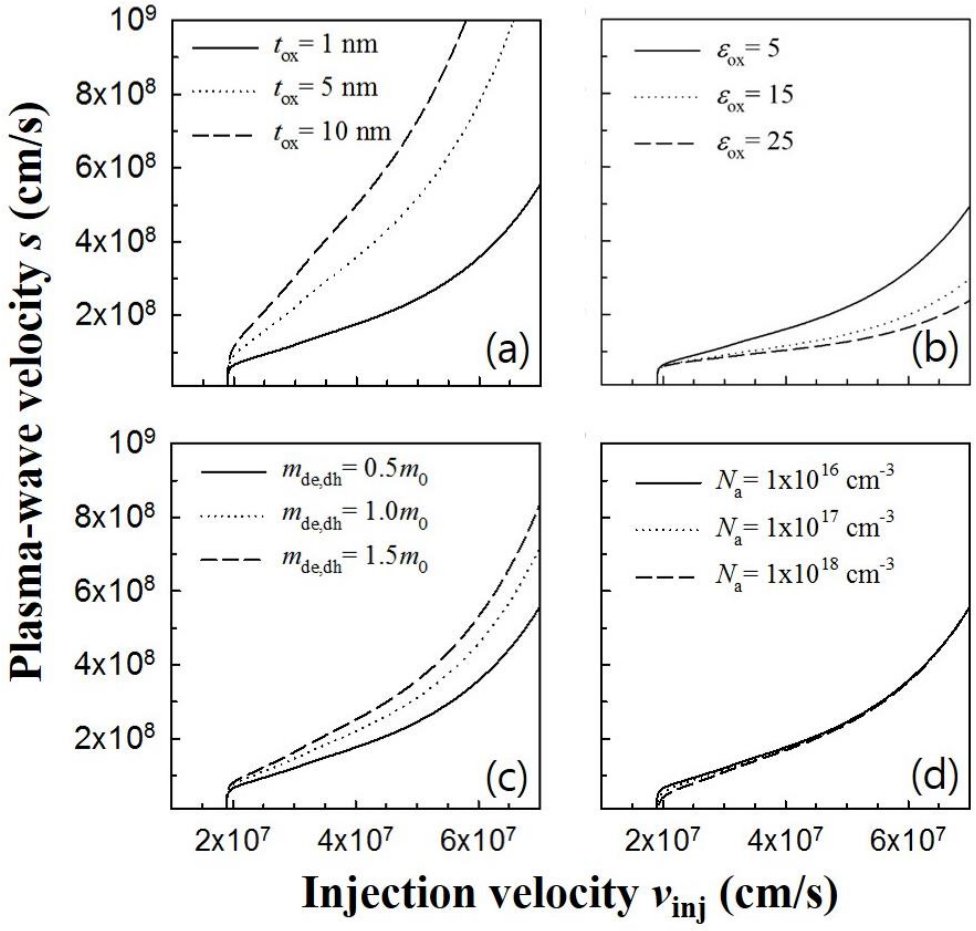

Figure 4-8. Plots of v_{inj} vs s for varying (a) t_{ox}, (b) ε_{ox}, (c) $m_{de,dh}$, and (d) N_a. Here $v_{inj}^* = 1.9\times10^7$ cm/s is calculated for an arbitrary material (m= $0.08m_0$).

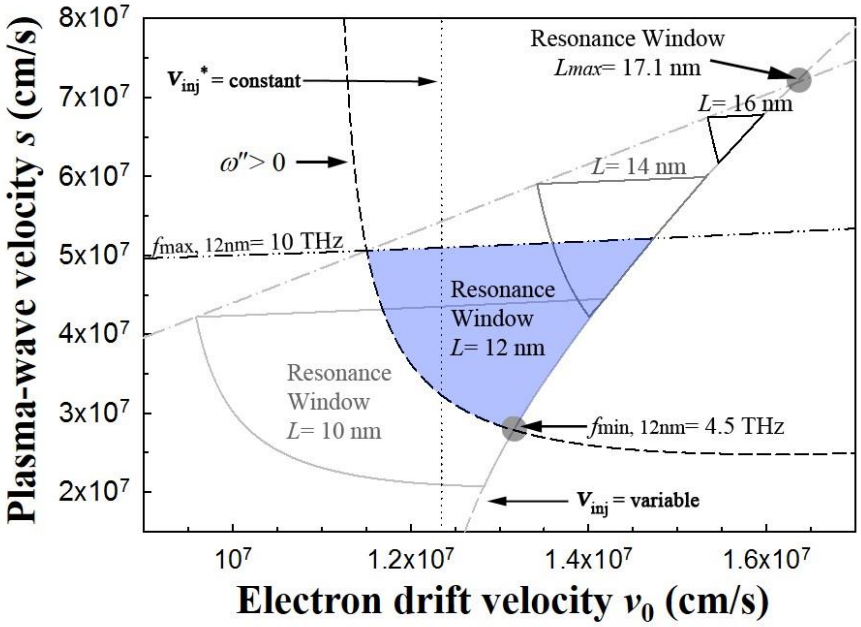

Figure 4-9. s-Si PWT design window (N= 1) assuming μ= 500 cm^2·V^{-1}·s^{-1} for t_{ox}= 1 nm, L= 10, 12, 14, 16, and 17.1 nm (L_{max}). The variable boundary of v_{inj} (Eq. (4.8)) based on degenerate 2DEG broaden the design window and L_{max}. Vertical dotted line illustrates the boundary of v_{inj}^* (constant) in the Boltzmann limit.

Figure 4-9 shows the design window including the degenerate carrier velocity model [73]. It is clear that the s-Si PWT THz emitter with μ= 500 cm^2·V^{-1}·s^{-1} has maximum channel length L_{max}= 17 nm, which is enhanced by the increment of injection velocity. It can be compared with the result of L_{max}= 12 nm in the previous chapter, which only considers non-degenerate 2DEG case.

Even though L_{max} is increased, it is noteworthy that the resonant frequency range in $v_{inj}^* < v_0 < v_{inj}$ regime in Fig.4-9 isn't broad much and is near the upper limit of 10 THz. In order to make the frequency range become broad near 1 THz, it is important to enhance the channel mobility to broaden the resonance window. The influence of the channel mobility on the R-PWT frequency range in design window is shown in Fig. 4-10. In the case of μ= 650 cm^2·V^{-1}·s^{-1}, the frequency range is considerably broaden as 3.8 < f < 10 THz compared to 9.05 < f < 10 THz for the case of the μ= 500 cm^2·V^{-1}·s^{-1}.

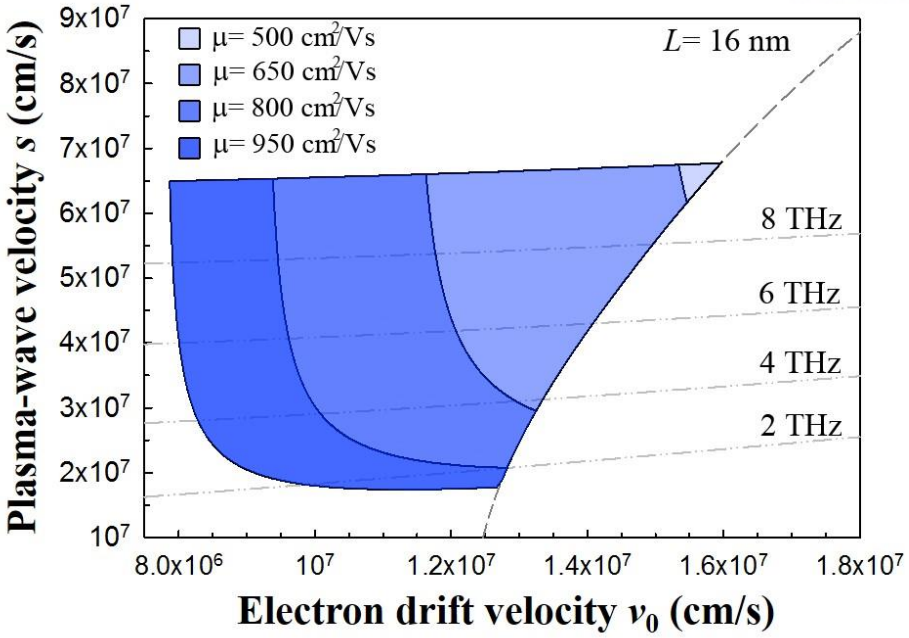

Figure 4-10. s-Si PWT design window (N= 1) assuming L= 16 nm with μ= 500, 650, 800, and 950 $cm^2 \cdot V^{-1} \cdot s^{-1}$.

Combining increased v_{inj} with enhanced μ remarkably improves L_{max} as illustrated in Fig. 4-11 which is the 3D design window using L as the z-axis. Here we assume that the 2DEG should not be strongly degenerate ($\{e\psi_s-(e\Phi_s-e\chi_s)\}-\varepsilon_1^*(0) < 4k_BT$) for sustaining electron-electron collision [29]. The assumption is correct since the electrons are mediums to propagate longitudinal plasma-wave. With the Eq. (4.8), for the s-Si case, Fermi level (E_F) exceeds $4k_BT$ above the first sub-band [$\varepsilon_1(0)$] when n_0= 3.52×10^{13} cm^{-2} so that s= 3.74×10^8 cm/s means the upper limitation of plasma-wave velocity in the resonance window. Thus, maximum frequency f_{max} is not 10 THz at L= 35 nm for μ= 800 $cm^2 \cdot V^{-1} \cdot s^{-1}$ case in Fig. 4-10. For realizing actual R-PWT THz emitter, it is necessary to consider gate oxide breakdown because of biasing relatively high U_0 to induce n_0 as the L increases. As a sample criterion, it is reported that breakdown occurs on MOS capacitor with t_{ox}= 3.9 nm when biasing $U_g \cong$ 6 V for 35 s [74]. Considering U_0~ 1.5 V as the breakdown voltage, it induces n_0= 3.3×10^{13} cm^{-2} (s= 1.18×10^7 cm/s) for s-Si PWT with t_{ox}= 1 nm and μ= 800 $cm^2 \cdot V^{-1} \cdot s^{-1}$ so that it would be safe to fabricate PWT until approximately L~ 35 nm.

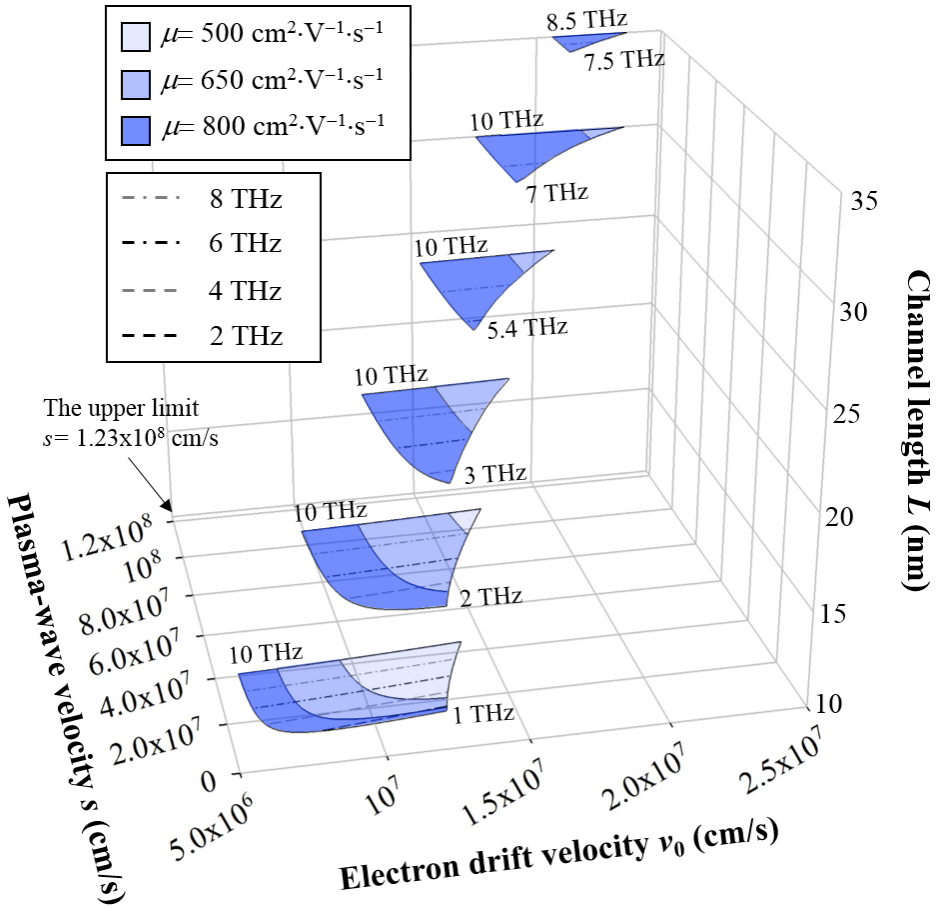

Figure 4-11. 3D design window plot which illustrates the trends of extending resonance window and operation frequency range with enhancing channel mobility.

4.3. Design window of FG SC-PWD

Starting from the plasma-wave frequency $\omega = \omega' + i\omega''$ as

$$\omega' = \frac{\alpha}{2v_0}\sqrt{1-\frac{1}{4}\left\{\left(2-\frac{v_0^2}{\alpha L}N\pi\right)^2-2\right\}^2} \tag{4.13}$$

$$\omega'' = \frac{v_0\sqrt{1-(2\eta)^2}}{\left(\sqrt{1+2\eta}-\sqrt{1-2\eta}\right)L}\ln|r_d| - \frac{1}{2\tau_p} \tag{4.14}$$

As known by Eqs. (4.13) and (4.14), plasma-wave frequency and its resonance are strongly dependent on v_0 and $s(v_0, \alpha, \eta)$ so that the design window of 2-D s-v_0 plot is helpful for evaluating FG SC-PWD THz emitter. By modulating plasma-wave velocity of Eq. (3.5) for the downstream, the basic s-v_0 line equation is given by

$$s_+ = \left[1+\sqrt{\frac{2}{1+\eta-\sqrt{1+2\eta}}}\right]v_{0,phys} \tag{4.15}$$

where $v_{0,phys}$ is determined by physical conditions in Table 1 for each η. Assuming $|Z_d| = \infty$, line equation for the increment condition can be induced by find the point where ideal and critical drain coefficients become equal ($r_{d,i} = r_{d,c}$ (i.e., $\omega'' = 0$)) for each η, which $r_{d,i}$ and $r_{d,c}$ are defined as

$$r_{d,i} = \frac{1-\eta-\sqrt{1-2\eta}}{1+\eta-\sqrt{1+2\eta}} \tag{4.16}$$

$$r_{d,c} = \exp\left[\frac{\left(\sqrt{1+2\eta}-\sqrt{1-2\eta}\right)L}{2\tau_p v_0\sqrt{1-(2\eta)^2}}\right] \tag{4.17}$$

the result is as follows:

$$v_{0,Incre}^{|Z_d|=\infty} = \frac{\left(\sqrt{1+2\eta}-\sqrt{1-2\eta}\right)L}{2\tau_p\sqrt{1-(2\eta)^2}\ln\left[r_{d,i}\right]} \tag{4.18}$$

Also, by using Eq. (4.13), $v_{0,phys}$ for the frequency condition is given by

$$v_{0,\,freq} = \frac{\omega' L}{\eta\pi}\left[2 - \sqrt{2 + 2\sqrt{1-(2\eta)^2}}\right] \tag{4.19}$$

Furthermore, if we also consider finite $|Z_d|$, the $v_{0,\mathrm{phys}}$ for the increment conditions can be obtained by using Eq. (4.17) and r_d as

$$r_d = r_{d,i} - \frac{r_{d,i}+1}{\left(1-2|Z_d|W\varepsilon\omega\right)e^{ik_+L_g}} \tag{4.20}$$

$$v_{0,Incre}^{|Z_d|\neq\infty} = \frac{\left(\sqrt{1+2\eta}-\sqrt{1-2\eta}\right)L}{2\tau_p\sqrt{1-(2\eta)^2}\ln\left[r_{d,i} - \dfrac{\left(r_{d,i}+1\right)\cos\left(k_+L\right)}{1-2|Z_d|W\varepsilon\omega'}\right]} \tag{4.21}$$

Because ω' is contained in both η and Eq. (4.21), we cannot yield line equation for increment condition with finite impedance by solely using Eq. (4.21). Instead, finding η where $v_{0,freq}$–$v_{0,\mathrm{incre}}$ for the fixed frequency and substituting this η in Eq. (4.19) can induce right line equation for this case. Fig. 4-12 illustrates various resonance window and its boundary lines, where dashed line is for instability condition, solid line is for increment condition, and dotted line is for frequency condition. It can be checked that resonance window is gradually disappeared as lowering $|Z_\mathrm{d}|$ with decreasing operation frequency range. Also, Figs. 3-2 and 4-12 have well explained each other. If $|Z_\mathrm{d}|$= 300 Ω is implemented on FG SC-PWD, the THz emitter operates with minimum frequency $f_{\min}$~ 5.5 THz.

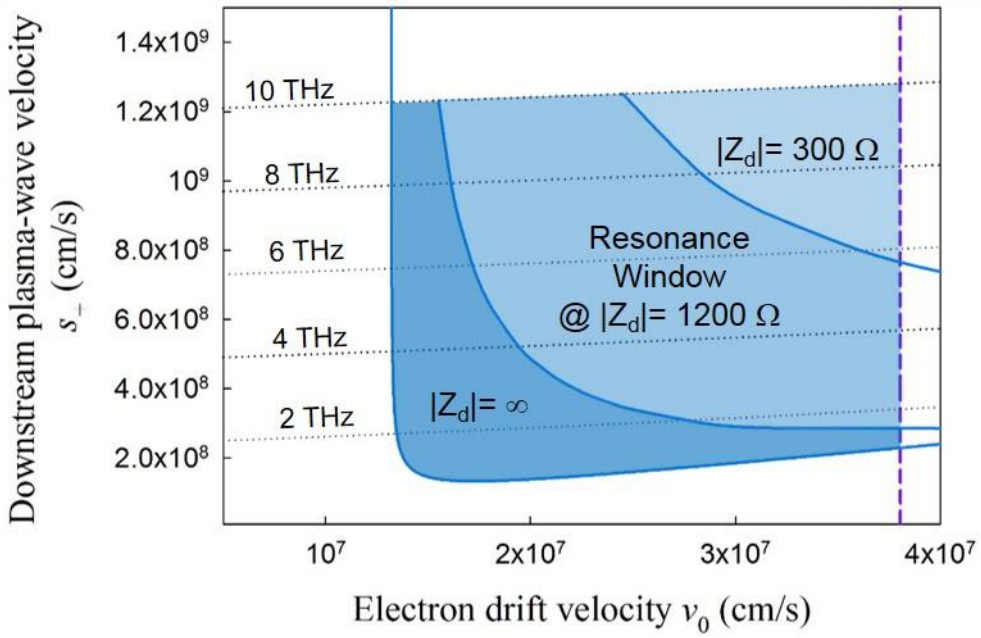

Figure 4-12. FG SC-PWD THz emitter 2D design window considering suspended graphene (μ= 10^5 cm^2/Vs) channel with L= 300 nm and W= 1000 nm

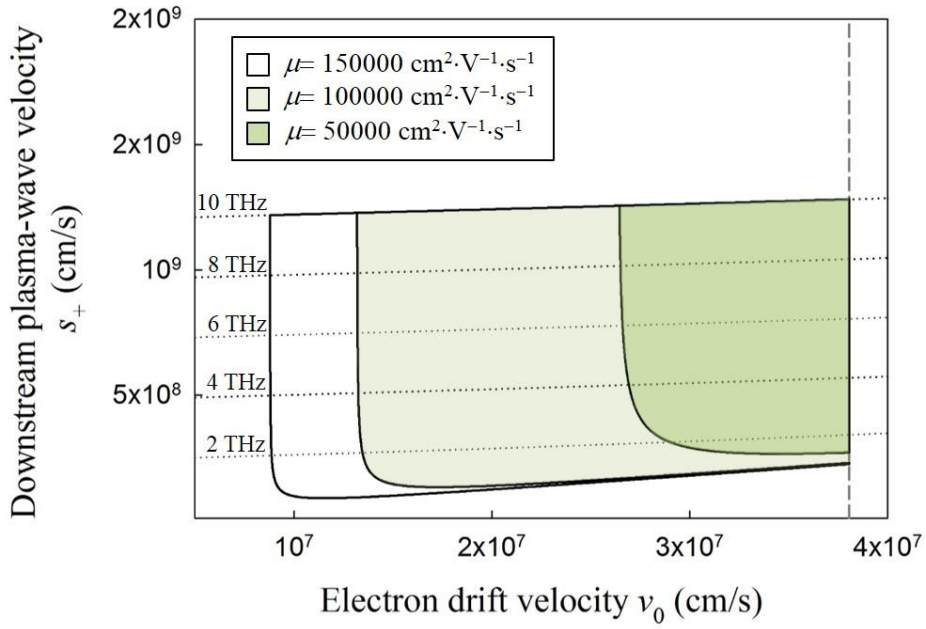

Figure 4-13. FG SC-PWD THz emitter 2D design window considering suspended graphene chan nel mobility with L= 300 nm and W= 1000 nm

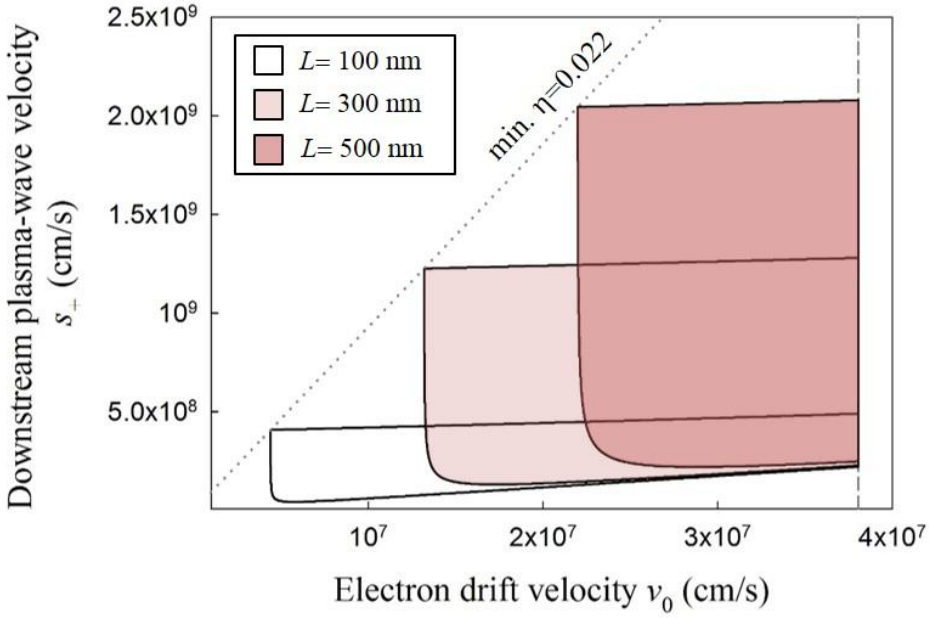

Figure 4-14. FG SC-PWD THz emitter 2D design window considering suspended graphene (μ= 10^5 cm^2/Vs) channel with W= 1000 nm

Figs. 4-13 and 4-14 illustrate various resonance windows for ideal boundary conditions by changing channel mobility and channel length. If the channel of SC-PWD has high mobility, plasma-wave can propagate further with relatively low electron drift velocity. For the channel length variation, it can be noted that resonance windows share same $\eta_{\min}$ for the same channel mobility. By using this fact, it is possible to calculate maximum channel length ($L_{\max}$) by using Eq. (4.18) as

$$L_{\max} = \frac{2\tau_p v_{inj}\sqrt{1-(2\eta_{\min})^2}\ln\left[r_{d,i}(\eta_{\min})\right]}{\left(\sqrt{1+2\eta_{\min}}-\sqrt{1-2\eta_{\min}}\right)} \tag{4.22}$$

For the case of graphene FG SC-PWD with μ= 10^5 cm/Vs, calculated $L_{\max}$ is 865 nm. However, if we consider practical boundary conditions ($|Z_d|$= finite), $L_{\max}$ is decreased as lowered $|Z_d|$. Fig. 4-15 describes this fact with assigning L as z-axis of 3-D design window. As explained previously in Fig. 4-12, decreased $|Z_d|$ makes resonance window shrink so that $L_{\max}$ is also decreased. Therefore, it is needed to implement $|Z_d|$ as much as possible. Also, it is recommended that making channel length as short as possible for obtaining broader operation frequency range even with low $|Z_d|$. It can be expected that FG SC-PWD THz emitter has higher possibility for practical and realizable device compared to R-PWT THz emitter because R-PWT shows narrow operation frequency range due to requiring higher $|Z_d|$ than FG SC-PWD at same channel length.

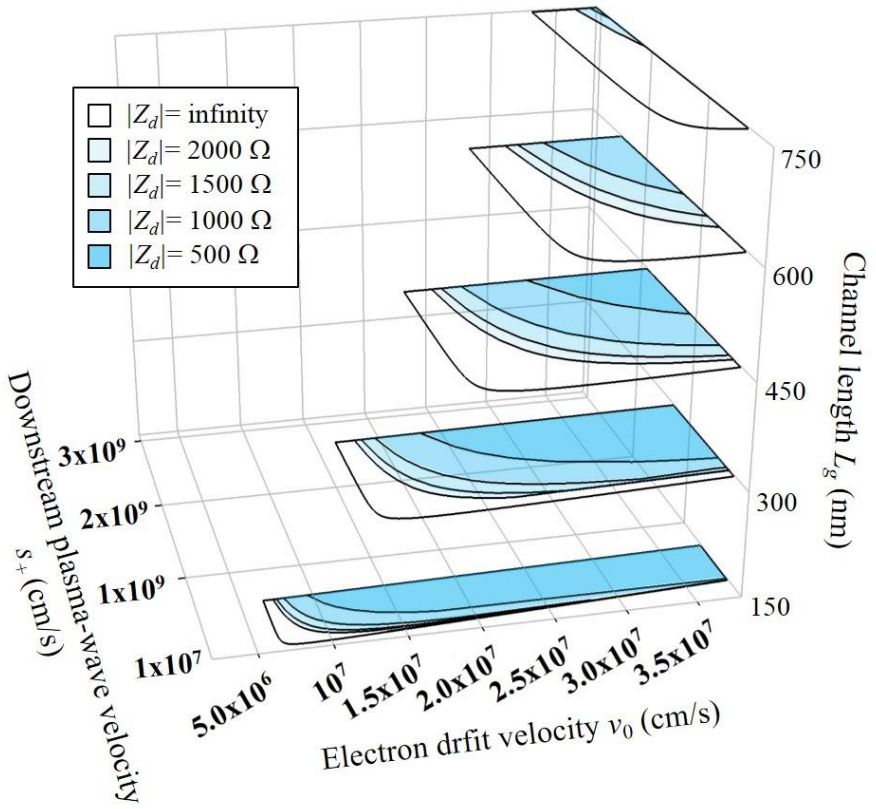

Figure 4-15. FG SC-PWD THz emitter 3D design window considering suspended graphene (μ= 10^5 cm^2/Vs) channel with L= 300 nm and W= 1000 nm for various values of drain impedance

4.4. Summary

In this chapter, the concepts of design window have been introduced to examine the possibility of R-PWT for various channel material, which have been only analyzed on III-V compounds or graphene cases with high channel mobility due to the lack of practical and realistic theory considering non-ideal assumptions. Firstly, the design window for R-PWT have shed light on the possibility of Si as a channel material of R-PWT by using physical conditions and considering electron source injection velocity as a variable. Next, it has been demonstrated that FG SC-PWD with ultra-high channel mobility of exfoliated graphene can be applied to THz technology with considering finite drain impedance.

Chapter V
Si R-PWT THz detector

5.1. Introduction

Based on the design window for Si R-PWT, which shows that resonant THz detection is possible even at l_{eff}= 20 nm (see Fig. 5-1), the objectives of device fabrication are focused on two approaches. One is enhancing channel mobility and the other is shortening channel length. In this chapter, the detailed device structure and experimental setup are discussed. Next, the experimental results are presented, and theoretical evidences guarantee resonant THz detection with Si technology.

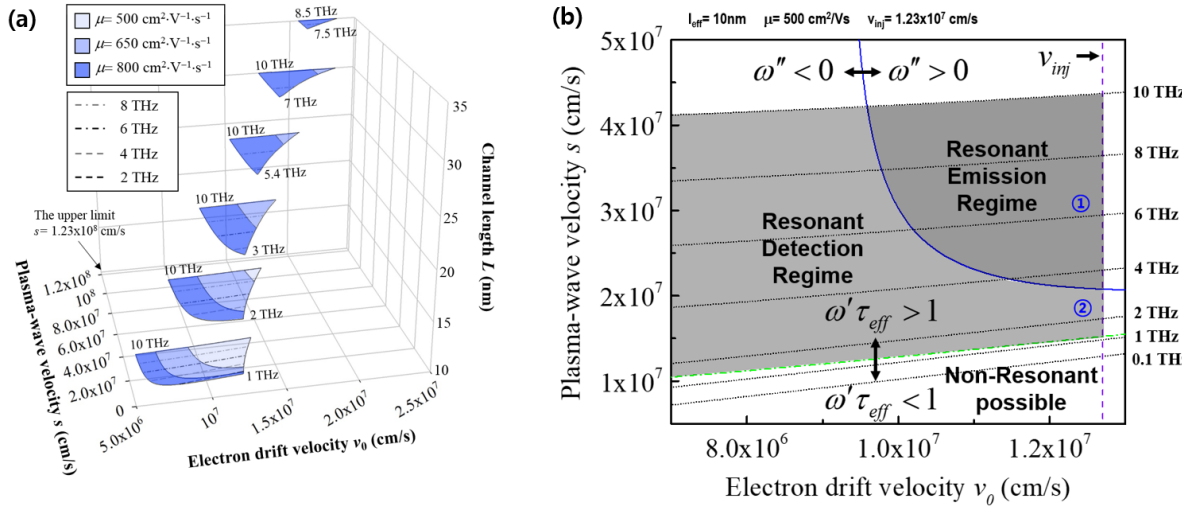

Figure 5-1. (a) Si R-PWT 3D design window considering source injection velocity as a variable, which shows resonance window as THz emitter. (b) Si R-PWT 2D design window shows resonant detection regime. These plots imply that resonant THz detection (and even emission) is possible by devise optimization (Figs. 4-5 and 4-9 are reused.)

5.2. Device structure and experimental setup

Figure 5-2(a) shows that fabricated strained-Si FinFET device structure. Starting with 8-inch strained SOI wafer with 15 nm of top Si thickness, an n-channel FinFET was fabricated with a channel thickness of 10 nm. The photolithography process using 0.18-um technology was employed to define the Fin. To achieve a minimum feature size of the fin and gate length, the photoresist ashing by oxygen plasma in part was performed. Fins were patterned by simple Si mesa etching. The gate stack consists of gate oxide of 3 nm formed by dry oxidation and in-situ phosphorus doped poly-crystalline Si (poly-Si). Arsenic implantation of a dose of $3x10^{15}$ cm^{-2} and energy level of 7 keV for the source and drain electrodes was done subsequent to the formation of the gate spacer. In order to have low parasitic resistance, $CoSi_2$ was selected for forming source and drain, which reduced resistance more than 1000 times so that the performance of the fabricated FET is also drastically improved. Also, it is very important to create a high quality of SiO_2-to-Si interface as this is deeply related to the generation of traps, which affect the mobility as well as the reliability of the devices. The forming gas annealing (FGA) process make the low field mobility increases from 480 cm^2/Vs to 800 cm^2/Vs at T= 293 K. The obtained mobility value is one of the record high values that have ever reported in other previous works. And it is obvious that the strain influences on electron transports in the ultra-thin body (UTB) as expected [48].

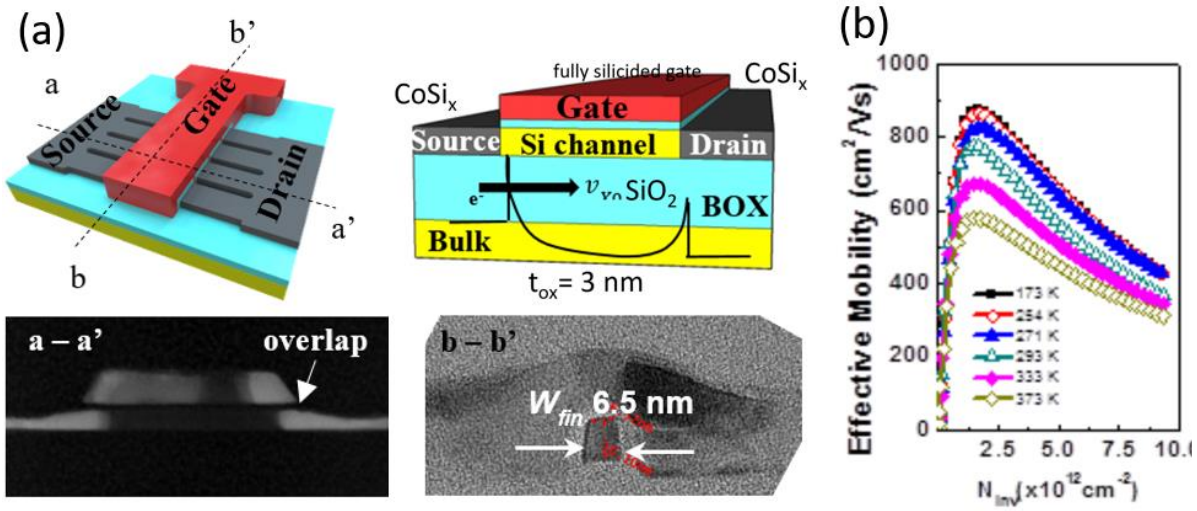

Figure 5-2. (a) Device structure and (b) its measured mobility.

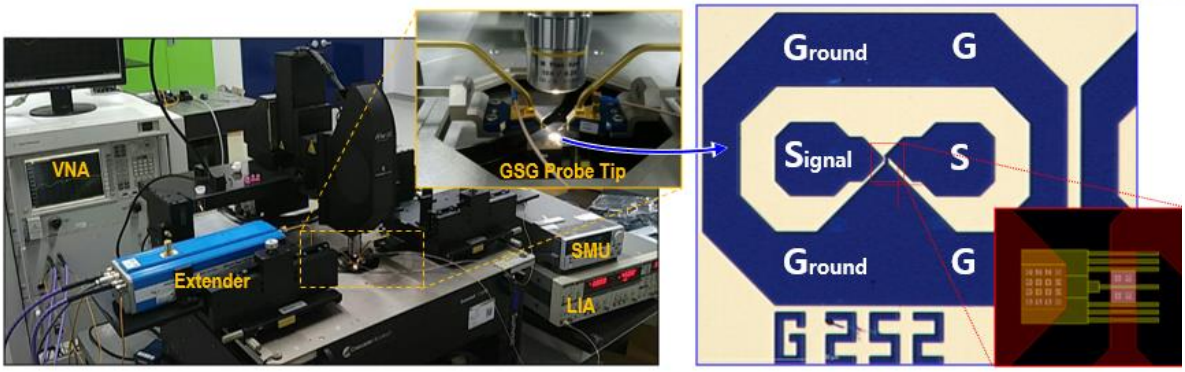

Figure 5-3. Experimental setup for THz detection.

Fabricated s-Si FinFET was measured on probe station for ground-signal-ground probe tips with VNA extender f= 90-220 GHz and Gunn diode source f= 500 GHz. Before measuring V_{out}, by using lock-in-amp (LIA), two I_d-V_g curves were measured continuously by using source meter unit (SMU). One is biasing THz signal using VNA and the other is turn off VNA. This procedure has advantage of fast checking compared to use LIA, which should dial each gate voltage manually. Most devices only show non-resonant (NR) THz detection as shown in Fig. 5-4. As non-resonant theory expects, NR peak appear when $C_{gs} < C_{gd}$ or $C_{gs} > C_{gd}$. Among lots of devices, few samples show clear resonant response, which will be discussed in next section.

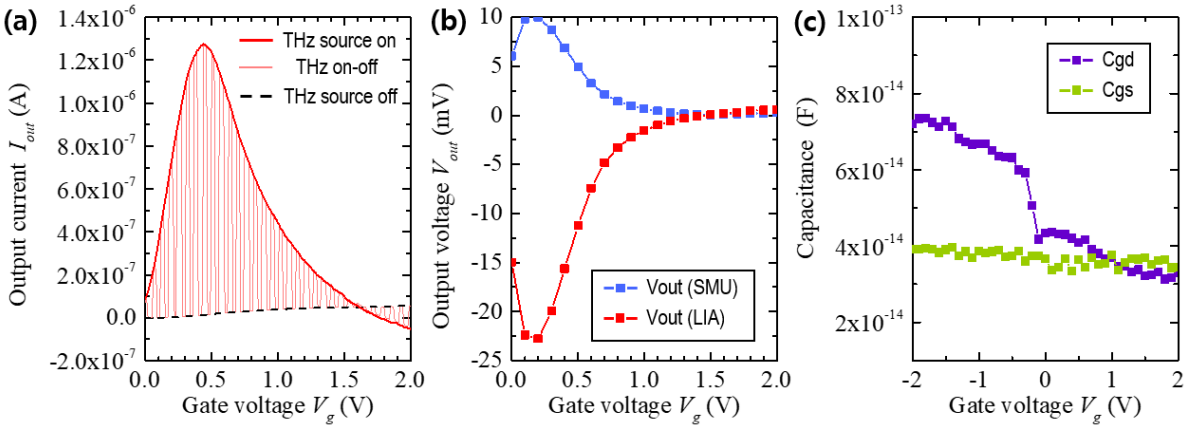

Figure 5-4. One example of NR peak characteristics (l_{eff}= 335 nm), which is helpful to analyze resonant peak, related to (a) I_{out}, (b) V_{out}, and (c) capacitance. This NR peak sample shows $C_{gs} < C_{gd}$ so that V_{out} measured by SMU has negative sign, which means $<U(x=0)>$ is higher than $<U(x=l_{eff})>$. It is noticeable that the I_{out} sign is reverse of V_{out} sign. Also, the lock-in-amp reads V_{out} as absolute value so that it shows positive V_{out} sign in the panel.

5.3. Experimental evidence for resonant THz detection

5.3.1. High quality factor of $\omega'\tau_{eff}>1$

TABLE III. CALCULATED QUALITY FACTORS FOR S-SI R-PWT BASED ON BFET STURUCTURE

Frequency (THz)	τ_{eff} **(fs)**	**Converted** $\mu(\tau_{eff})$ **(cm²/V·s)**	$\omega'\tau_{eff}$
0.1	197	1820	0.96
0.5	207	1920	1.09
1	270	2500	1.96
1.5	374	3460	3.63

There are three evidences to determine whether the device shows characteristics of resonant THz detection. One is that high quality factor ($\omega'\tau_{eff}>1$) is achieved in Si R-PWT due to short l_{eff}= 20 nm and high μ= 800 cm²/Vs. If we consider effective momentum relaxation time which can be represented as

$$\frac{1}{\tau_{eff}} = \frac{1}{\tau} - \frac{s^2 - v_0^2}{l_{eff}\, s} \ln\left(\frac{s + v_0}{s - v_0}\right) \tag{5.1}$$

As discussed in chapter 2.5.1, the concept of τ_{eff} is to explain resonant phenomena even when $\omega''<0$ so that plasma-wave resonance cannot occur itself with biasing gate or drain bias. Because high τ_{eff} means less damping of the amplitude of plasma-wave, the criterion combining τ_{eff} with resonant plasma-wave frequency (ω') (i.e. $\omega'\tau_{eff}>1$) is helpful to judge the possibility of R-PWT THz detection. As shown in Table III, which is calculation result based on measured parameters (l_{eff}= 20 nm, μ = 800 cm²/Vs) , the effective momentum relaxation time is evaluated τ_{eff} = 197 fs even at f= 0.1 THz so that $\omega'\tau_{eff}$ = 0.96 and its converted mobility for plasma-wave is μ (τ_{eff}) = 1820 cm²/Vs. oscillation

5.3.2. Resonant V_{out} peak placed above threshold voltage

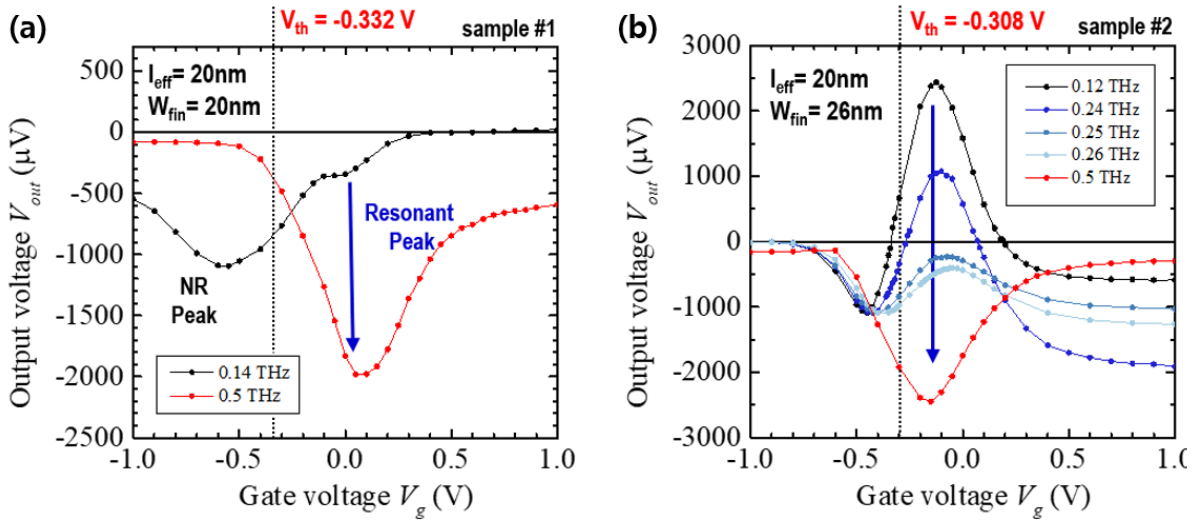

Figure 5-5. Measured V_{out} showing both resonant and non-resonant peaks. The values of threshold voltage are calculated from I_d-V_g curve using $g_{m,max}$ at V_d= 50 mV.

The main difference between resonant and non-resonant mode is that the resonant phenomenon occurs in the strong inversion condition of MOSFET since plasma-wave should propagate and make multiple reflections in the channel. Lack of electrons in the channel hampers forming temporal and spatial collective oscillations (i.e. plasma-wave). On the contrary, non-resonant phenomenon is only excited by external THz signal, which makes plasma-wave starting from source side when the ideal condition ($C_{gd} > C_{gs}$) is achieved. The highest V_{out} peak of non-resonant plasma-wave lose its amplitude by increased plasma-wave velocity, which means the wave become gradually close to the drain side as increasing V_g. In this case, If the quality factor is higher than unity with achieving boundary conditions, it is possible that the amplitude of plasma-wave increases again, and its peak is placed on the point that resonant frequency coincides with external THz frequency. Figure 5-5 demonstrates this procedure well because there are shown two peaks which placed each other across threshold voltage.

5.3.3. Non-linear increment of V_{out} peak

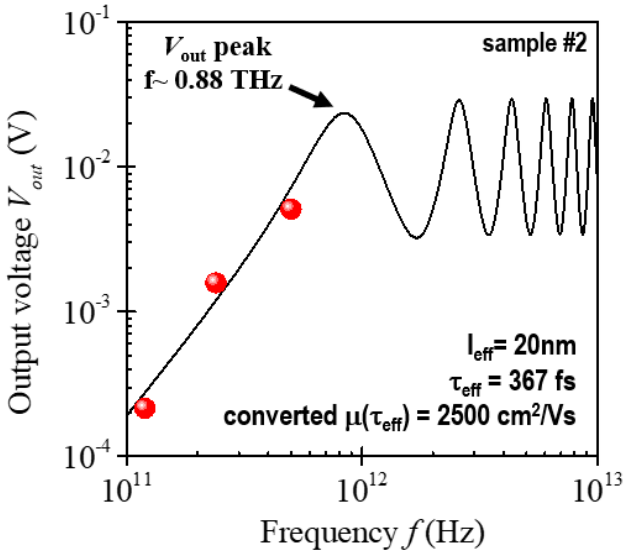

Figure 5-6. V_{out} vs. f plot showing non-linear increment of plasma-wave resonance as frequency increases. The measurement data is displayed by red dot and theoretical V_{out} (black solid line) is evaluated by using reported 'NR+R V_{out} equation' (Eq. 2.40).

Finally, the plasma-wave resonance should show non-linear increment as frequency increases. The resonant peak of sample 2 in Fig. 5-5 increases apparently from f= 0.1 to 0.5 THz compared to NR peaks placed below V_{th}. Figure 5-6 illustrates that measured V_{out} shows non-linear increment as frequency increases. Three red dots are picked by experimental data from 0.12/0.25/0.5 THz and theoretical V_{out} is calculated by using Eq. (2.40) which shows Vout resonant peak occurs at f~ 0.88 THz. There are still unclear points to explain as a further work. One is that the value of resonant V_{out} peak starts from positive sign at f= 0.1 THz and increases with changing its sign to be negative at f= 0.5 THz. The other is that experimental results of f= 0.24-0.26 THz in sample 2 shows unclear increasing trends to explain non-linear increment compared to theoretical V_{out} using Eq. (2.40). All reported V_{out} equations by many researchers assume that external THz signal make electrons inject into the channel only from the source of FET. However, as non-resonant boundary conditions explain, electrons can be injected from both source and drain side by C_{gs} and C_{gd}. Therefore, it is necessary to derive quantitative V_{out} equations that deals with two starting direction of plasma-wave from source and drain sides in the channel to explain all resonant peak generated at $\omega = \omega'$.

5.4. Summary

In this chapter, the first experimental results of resonant THz detection by using Si as a channel material of R-PWT have been introduced as expected by the design window of Si R-PWT. The devices have been carefully fabricated, which has Schottky barrier between source/drain and channel based on short channel FinFET (l_{eff}= 20 nm) structure with recording channel mobility of 800 cm^2/Vs. The experiment has been conducted by using VNA and Gunn diode source with frequency range of 0.1-0.5 THz. These experimental data have demonstrated that plasma-wave occurs in the channel of R-PWT, which are verified by three evidences: One is that high quality factor of $\omega'\tau_{eff}$>1 is secured. The other is measured V_{out} peak placed above V_{th} (compared to NR V_{out} peak below V_{th}). Finally, the measured V_{out} as frequency increases shows non-linear tendency, even though it is necessary to conduct strict investigation based on plasma-wave theory as a further work.

Chapter VI
Remaining work to be done

In this thesis, it has been reported that R-PWD can be a best candidate to achieve lots of THz applications based on electronic approaches. To verify it, theory of R-PWT and FG SC-PWD has been demonstrated with design windows. By using these theoretical expectations, it has been firstly introduced that plasma-wave resonance can occurs in the channel of Si R-PWT with various evidences. However, there are still remaining work to be done. Starting from the theory of THz emission, because the evaluated power of R-PWT assuming ideal conditions is in μW scale, which is too low and comparable to the reported experimental emission power in non-ideal conditions, the derivation of power equation for R-PWT should be carefully reconstructed by inspecting missing concepts and variables. Also, in terms of FG SC-PWD, it is necessary to consider optimal distance between floating gate and suspended channel, which should be contained in the power equation. The other remaining work is related to theory of R-PWT THz detection. Despite it has been successfully derived that wavenumber and V_{out} equations explain resonant plasma-wave behaviors, it has been revealed that these equations are insufficient to study non-resonant phenomena and interpret the experimental data related to the non-linear increment of V_{out} with increasing frequency.

Chapter VII
Conclusion

In this thesis, I firstly report the possibility of silicon (Si) plasma wave transistor (PWT) as a resonant terahertz (THz) emitter and detector based on the theoretical analysis focusing on the strained Si with enhanced mobility. Under asymmetric boundary conditions for plasma wave instability, the amplitude of plasma wave in FET channel increases and this plasma wave increment provides the basis of the electromagnetic (EM) wave emission from FET and responses for external THz signal. Secondly, I introduced novel device structure of FG SC-PWD which is possible to emit and detect THz signal with higher performance. In order to verify the possibility of R-PWD for various materials, I suggested the concept of design window which considers both plasma-wave and electronic device theories. Finally, based on the design window of R-PWT, I reported experimental evidences for plasma-wave resonance in strained-Si channel FET. I explained three reasons why resonance occurs with various measurement data: Resonant peak exists above-threshold regime and its output response voltage increase non-linearly as external frequency increases when quality factor $Q = \omega' \tau_{eff} > 1$ condition is satisfied.

Reference

[1] Z. Zhang, Y. Xiao, Z. Ma, M. Xiao, Z. Ding, X. Lei, G. K. Karagiannidis, and P. Fan, "6G Wireless Networks: Vision, Requirements, Architecture, and Key Technologies," IEEE Veh. Technol. Mag. 14, pp 28–41, 2019.

[2] A. I. Tsvetkov, A. P. Fokin, and A. S. Sedov, "First experiments on data transmission using a sub-THz gyrotron," J. Infrared Millim. Terahertz Waves. vol. 40, no. 6, pp 696-702, Jun. 2019.

[3] E. C. Strinati, S. Barbarossa, J. L. Gonzalez-Jimenez, D. Ktenas, N. Cassiau, L. Maret, and C. Dehos, "6g: The next frontier: From holographic messaging to artificial intelligence using subterahertz and visible light communication," IEEE Veh. Technol. Mag. 14, pp 42–50, 2019.

[4] M. W. Ryu, J. S. Lee, K. Park, W.-K. Park, S.-T. Han, and K. R. Kim, "Photoresponse enhancement of plasmonic terahertz wave detector based on asymmetric silicon MOSFETs with antenna integration," Jpn. J. Appl. Phys., vol. 53, no. 4S, pp. 04EJ05-1-04EJ05-4, Apr. 2014.

[5] M. W. Ryu, K. S. Kim, J. S. Lee, K. Park, J. -R. Yang, S. -T. Han and K. R. Kim, "Performance enhancement of plasmonic sub-terahertz detector based on antenna integrated low-impedance silicon MOSFET" IEEE Electron Devices Lett., vol. 36, pp. 220-222, 2015.

[6] M. W. Ryu, S. H. Ahn, J.-R. Yang, W.-J. Lee, S.-T. Han and K. R. Kim, "Plasmonic 1x200 array scanner based on 65-nm CMOS asymmetric FETs for real-time terahertz imaging" in Proc. 74th Device Research Conference, pp. 223-224, 2016.

[7] M. W. Ryu, J.S. Lee, K.S. Kim, K. Park, J.R. Yang, S.-T. Han, and K.R. Kim, "High Performance Plasmonic THZ detector on Asymmetric FET with Vertically Integrated Antenna in CMOS Technologe." IEEE Transactions on Electron Devices, vol. 63, no 4, pp.1742-1748, Apr 2016.Imaging

[8] M. Krbal, J. Kucharik, H. Sopha, H. Nemec, and J. M. Macak, "Charge transport in anodic TiO2 nanotubes studied by terahertz spectroscopy," Phys. Status Solidi. RRL 10, no. 9, pp 691-695, 2016.

[9] Hannah J Joyce, Jessica L Boland, Christopher L Davies, Sarwat A Baig and Michael B Johnston, "A review of the electrical properties of semiconductor nanowires: insights gained from terahertz conductivity spectroscopy" Semicond. Sci. Technol. 31, 103003, 2016

[10] T. Morimoto, M. Nagai, Y. Minowa, M. Ashida, Y. Yokotani, Y. Okuyama, and Y. Kani, "Microscopic ion migration in solid electrolytes revealed by terahertz time-domain spectroscopy," Nat. Comm. 10, 2662, 2019.

[11] Alexander I. McIntosh, Bin Yang, Stephen M. Goldup, Michael Watkinson and Robert S.

Donnan, “Terahertz spectroscopy: a powerful new tool for the chemical sciences?.” Chem. Soc. Rev., 41, 2072-2082, 2012

[12] L. Zhou, L. Chen, G. Ren, Z. Zhu, H. Zhao, H. Wang, W. Zhang, and J. Han, “Monitoring cis-to-trans isomerization of azobenzene using terahertz time-domain spectroscopy,” Phys. Chem. Chem. Phys., 20, 27205, 2018.

[13] Carr, G., Martin, M., McKinney, W. et al. High-power terahertz radiation from relativistic electrons. Nature 420, 153–156, 2002.

[14] G. Liang, T. Liu, and Q. J. Wang, “Recent Developments of Terahertz Quantum Cascade Lasers,” IEEE J. Sel. Top. Quantum Electron., 23(4), 2017

[15] P. Chevalier, A. Amirzhan, F. Wang, M. Piccardo, S. G. Johnson, F. Capasso1, and H. O. Everitt, “Widely tunable compact terahertz gas lasers,” Science 366, 6467, 2019

[16] M. Tonouchi, “Cutting-edge terahertz technology,” nature photonics 1, 2007

[17] G. I. Haddad and R. J. Trew, “ Microwave Solid-State Active Devices,” IEEE Trans. Microw. Theory Tech., vol. 50, no. 3, 2002

[18] G. H. Jessen, R. C. Fitch, J. K. Gillespie, G. Via, A. Crespo, D. Langley, D. J. Denninghoff, M. Trejo, and E. R. Heller, “Short-Channel Effect Limitations on High-Frequency Operation of AlGaN/GaN HEMTs for T-Gate Devices,” IEEE Trans. Electron Devices, Vol. 54 (10), 2007

[19] V. Ryzhii and M. S. Shur, "Plasma wave electronics devices," presented at 2003 International Semiconductor Device Research Symposium, no.03EX741, Washington, DC, USA, 2003.

[20] A. El Fatimy, F. Teppe, N. Dyakonova, and W. Knap, “Resonant and voltage-tunable terahertz detection in InGaAs⁄InP nanometer transistors”, Appl. Phys. Lett., vol. 89, no. 13, 131926, 2006.

[21] A. Shchepetov, C. Gardes, Y. Roelens, A. Cappy, S. Bollaert, S. Boubanga-Tombet, F. Teppe, D. Coquillat, S. Nadar, N. Dyakonova, H. Videlier, W Knap, D. Seliuta, R. Vadoklis, and G. Valusis, “Oblique modes effect on terahertz plasma wave resonant detection in InGaAs⁄InAlAs multichannel transistors”, Appl. Phys. Lett., vol.92, 242105, 2008.

[22] S. Boubanga-Tombet, F. Teppe, D.Coquillat, S. Badar, N. Dyakonova, H. Videlier, W. Knap, A. Shchepetov, C. Gardes, Y. Roelens, S. Bollaert, D. Seliuta, R. Vadoklis, and G. Valusis, “Current driven resonant plasma wave detection of terahertz radiation: Toward the Dyakonov-Shur instability”, Appl. Phys. Lett., vol. 92, 212101, 2008.

[23] J.-Q. Lu, and M. Shur, “Terahertz detection by high-electron-mobility transistor: Enhancement by drain bias”, Appl. Phys. Lett., vol.78, 12, 2001.

[24] J.-Q. Lű, M. S. Shur, J. L. Hesler, L. Sun, and R. Weikle, “Terahertz detector utilizing two-dimensional electronic fluid,” IEEE Electron Devices Lett., vol. 19, no. 10, pp. 373-375, Oct.

1998

[25] J. Mateos and T. Gonzalez, "Plasma Enhanced Terahertz Rectification and Noise in InGaAs HEMTs," IEEE Trans. THz Sci. Technol., vol. 2, no. 5, pp. 562–569, Sep. 2012.

[26] T. Otsuji, T. Komori, T. Watanabe, T. Suemitsu, D. Coquillat, W. Knap, "Plasmon-Resonant Microchip Emitters and Detectors for Terahertz Sensing and Spectroscopic Applications," in Proc. of SPIE, vol. 7671, 2010, pp.767102-1-767102-12.

[27] W. Knap and J. Lusakowski, T. Parenty, S. Bollaert, A. Cappy, V. V. Popov, M. S. Shur, "Terahertz emission by plasma waves in 60 nm gate high electron mobility transistors," Appl. Phys. Lett., vol. 84, no. 13, pp. 2331–2333, Mar. 2004.

[28] S. Boubanga-Tombet, F. Teppe, J. Torres, A. El Moutaouakil, D. Coquillat, N. Dyakonova, C. Consejo, P. Arcade, P. Nouvel, H. Marinchio, T. Laurent, C. Palermo, A. Penarier, T. Otsuji, L. Varani, and W. Knap, "Room temperature coherent and voltage tunable terahertz emission from nanometer-sized field effect transistors," Appl. Phys. Lett., vol. 97, 2010, Art. ID 262108.

[29] M. Dyakonov and M. Shur, "Shallow Water Analogy for a Ballistic Field Effect Transistor: New Mechanism of Plasma Wave Generation by dc Current," Phys. Rev. Lett. vol. 71, no. 15, pp. 2465-2468, Oct. 1993.

[30] J. Y. Park, S.-H. Kim, Y.-K. Choi, S. Hong, S.-G. Lee, and K. R. Kim, "Possibility and design of resonant terahertz emitters based on nanoscale strained silicon plasma wave transistors with enhanced mobility," Jpn. J. Appl. Phys., vol. 53, 2014.

[31] J. Y. Park, S.-H. Kim, and K. R. Kim, "Deca-nanoscale maximum gate length of plasma wave transistor for operating terahertz emitter based on strained silicon platform," in Proc. 14th IEEE NANO, pp. 150–153, Aug. 2014.

[32] J. Y. Park, S.-H. Kim, S. Hong, and K. R. Kim, "Physical Analysis and Design of Resonant Plasma-Wave Transistors for Terahertz Emitters," IEEE Trans. THz Sci. Technol., vol. 5, no. 2, pp. 244–250, Mar. 2015.

[33] M. Dyakonov and M. Shur, "Detection, mixing, and frequency multiplication of terahertz radiation by two-dimensional electronic fluid," IEEE Trans. Electron. Devices, vol. 43, no. 3, pp. 380-387, Mar. 1996.

[34] D. A. Bandurin, D. Svintsov, I. Gayduchenko, S. G. Xu, A. Principi, M. Moskotin, I. Tretyakov, D. Yagodkin, S. Zhukov, T. Taniguchi, K. Watanabe, I. V. Grigorieva, M. Polini, G. N. Goltsman, A. K. Geim, and G. Fedorov, "Resonant terahertz detection using graphene plasmons," Nat. Comm. 9, 5392, 2018.

[35] F. J. Crowne, "Contact boundary conditions and the Dyakonov–Shur instability in high electron mobility transistors," J. Appl. Phys., vol. 82, no. 3, pp. 1242-1254, Aug. 1997.

[36] F. Teppe, W. Knap, D. Veksler, M. Shur, A. P. Dmitriev, V. Yu. Kachorovskii, and S.

Rumyantsev, “Room-temperature plasma waves resonant detection of sub-terahertz radiation by nanometer field-effect transistor,” Appl. Phys. Lett., vol. 87, 052107, 2005.

[37] S. Rudin, G. Rupper, A. Gutin, and M. Shur, “Theory and measurement of plasmonic terahertz detector response to large signals,” J. Appl. Phys., vol. 115, 064503, 2014.

[38] V. V. Popov, O. V. Polischuk, W. Knap, and A. El Fatimy, “Broadening of the plasmon resonance due to plasmon-plasmon intermode scattering in terahertz high-electron-mobility transistors,” Appl. Phys. Lett., vol. 93, no. 26, pp. 263503-1-3, Dec. 2008.

[39] V. Ryzhii, A. Satou, W. Knap, and M. S. Shur, “Plasma oscillations in high-electron mobility transistors with recessed gate,” J. Appl. Phys. 99, 084507, 2006.

[40] M. V. Cheremisin and, G. G. Samsonidze, “Current instability and single-mode THz generation in ungated two-dimensional electron gas,” Solid-State Electron.: Short Communication, vol. 52, pp. 338–340, 2008.

[41] M. V. Cheremisin, “Resonance terahertz detection in ungated two-dimensional electron gas,” J. Appl. Phys. 106, 104501, 2009.

[42] M. V. Cheremisin, M. I. Dyakonov, M. S. Shur, and, G. Samsonidze, “Influence of electron scattering on current instability in field effect transistors,” Solid-State Electron., vol. 42, no. 9, pp. 1737–1742, 1998.

[43] Jr. B. W. Griffith, “Transmission lines,” in Radio-Electronic Transmission Fundamentals, 2nd ed. Stevenage, U.K.: SciTech Publishing, 2000, ch. 2, pp. 210–212..

[44] Y. Zhao, W. Chen, W. Li, M. Zhu, Y. Yue, B. Song, J. Encomendero, B. Sensale-Rodriguez, H. Xing, and P. Fay: Direct electrical observation of plasma wave-related effects in GaN-based two-dimensional electron gases, Appl. Phys. Lett., vol. 105, no. 17, 173508-1-173508-5, 2014

[45] L. Wang, I. Meric, P. Y. Huang, Q. Gao, Y. Gao, H. Tran, T. Taniguchi, K. Watanabe, L. M. Campos, D. A. Muller, J. Guo, P. Kim, J. Hone, K. L. Shepard, and C. R. Dean: One-Dimensional Electrical Contact to a Two-Dimensional Material, Science, 342, 614-617, 2013

[46] Xuesong Li, Carl W. Magnuson, Archana Venugopal, Rudolf M. Tromp, James B. Hannon, Eric M. Vogel, Luigi Colombo, and Rodney S. Ruoff: Large-Area Graphene Single Crystals Grown by Low-Pressure Chemical Vapor Deposition of Methane on Copper, J. Am. Chem. Soc., vol. 133, 2816-2819, 2011

[47] Libo Gao, Wencai Ren, Huilong Xu, Li Jin, Zhenxing Wang, Teng Ma, Lai-Peng Ma, Zhiyong Zhang, Qiang Fu, Lian-Mao Peng, Xinhe Bao, and Hui-Ming Cheng: Repeated Growth and Bubbling Transfer of Graphene with Milimtre-Size Single-Crystal grains Using Platinum, Nature Communications, vol. 3, 2012

[48] Chang-Hoon Jeon, Byung-Hyun Lee, Byung Chul Jang, Sung-Yool Choi, and Yang-Kyu Choi, “Experimental study on quantum mechanical effect for insensitivity of threshold

voltage against temperature variation in strained SOI MOSFETs", 2015 IEEE SOI-3D-Subthreshold Microelectronics Technology Unified Conference (S3S), 5-8, Oct. 2015.

[49] M. I. Dyakonov, "Boundary Instability of a Two-Dimensional Electron Fluid," Semiconductors, Vol. 42, No. 9, pp. 984-988, 2008

[50] Stanford Research Systems. (2011). MODEL SR830: DSP Lock-In Amplifier. Sunnyvale, California: SRS

[51] T. Onishi, T. Tanigawa, and S. Takigawa, "High power terahertz emission from a single gate AlGaN/GaN field effect transistor with periodic Ohmic contacts for plasmon coupling," Appl. Phys. Lett. 97, 092117, 2010

[52] D. Veksler, F. Teppe, A. P. Dmitriev, V. Yu. Kachorovskii, W. Knap, and M. S. Shur, "Detection of terahertz radiation in gated two-dimensional structures governed by dc current," Phys. Rev. B, 73, 125328, 2006.

[53] W.knap, V. Kachorovskii, Y. Deng, S. Rumyantsev, J. -Q. Lu, R. Gaska, M. S. Shur, G. Simin, X. Hu, M. A. Khan, C. A. Saylor, and L. C. Brunel, "Nonresonant detection of terahertz radiation in field effect transistors," J. Appl. Phys., 91, 11, 2002.

[54] N. Dyakonova, A. El Fatimy, J. Łusakowski, and W. Knap, "Room-temperature terahertz emission from nanometer field-effect transistors," Appl. Phys. Lett. 88, 141906, 2006

[55] T. Otsuji, T. Watanabe, A. El Moutaouakil, H. Karasawa, T. Komori, A. Satou, T. Suemitsu, M. Suemitsu, E. Sano, W. Knap, and V. Ryzhii, "Emission of Terahertz Radiation from Two-Dimensional Electron Systems in Semiconductor Nano- and Hetero-Structures," J. Infrared Milli Terahz Waves, vol. 32, no. 5, pp. 629-645, May 2011.

[56] F. Schwierz, "Graphene transistors," Nature Nanotechnology, vol. 5, pp. 487-496, May 2010.

[57] Y. Q. Wu, Y.-M. Lin, K. A. Jenkins, J. A. Ott, C. Dimitrakopoulos, D. B. Farmer, F. Xia, A. Grill, D. A. Antoniadis, P. Avouris, "RF performance of short channel graphene field-effect transistor", Proc. IEEE Int. Electron Devices Meeting (IEDM), pp. 9.6.1-9.6.3, Dec. 2010.

[58] S. Shivaraman, R. A. Barton, X. Yu, J. Alden, L. Herman, MVS Chandrashekhar, J. Park, P. L. McEuen, J. M. Parpia, H. G. Craighead, and M. G. Spencer, "Free-Standing Epitaxial Graphene," Nano Letters 9 (9), 3100-3105, 2009.

[59] M. Dyakonov and M. S. Shur, "Current instability and plasma waves generation in ungated two-dimensional electron layers," Appl. Phys. Lett., 87, 111501, 2005.

[60] H.-C. Ho, T.–W. Fan, and H.–K. Lin, "Low Output-Conductance InAs-Channel Metal-Oxide-Semiconductor Field-Effect Transistors with SiO2 Gate Dielectrics," Electrochem. Solid-State Lett., vol. 14, no. 8, pp. H340-H342, May 2011.

[61] S. J. Bentley, M. Holland, X. Li, G. W. Paterson, H. Zhou, O. Ignatova, D. Macintyre, S. Thoms, A. Asenov, B. Shin, J. Ahn, P. C. McIntyre, and I. G. Thayne, "Electron Mobility in

Surface and Buried Channel Flatband In0.53Ga0.47As MOSFETs with ALD Al2O3 Gate Dielectric," IEEE Electron Device Lett., vol. 32, no. 4. pp. 494-496, Apr. 2011.

[62] K. Rajagopalan, J. Abrokwah, R. Droopad, and M. Passlack, "Enhancement-Mode GaAs n-Channel MOSFET," IEEE Electron Device Lett., vol. 27, no. 12, pp. 959-962, Dec. 2006.

[63] K. Morii, T. Iwasaki, R. Nakane, M. Takenaka, and S. Takaki, "High-Performance GeO2/Ge nMOSFETs with Source/Drain Junctions Formed by Gas-Phase Doping," IEEE Electron Device Lett., vol. 31, no. 10, pp. 1092-1094, Oct. 2010.

[64] W. Xiong, C. R. Cleavelin, P. Kohli, C. Huffman, T. Schulz, K. Schruefer, G. Gebara, K. Mathews, P. Patruno, Y. M. L. Vaillant, I. Cayrefourcq, M. Kennard, K. Shin, and T. J. K. Liu, "Impact of Strained Silicon-on-Insulator (sSOI) Substrate on FinFET Mobility" IEEE Electron Device Lett., vol. 27, no. 7, pp. 612-614, Jul. 2006.

[65] S. Takagi, A. Toriumi, M. Iwase, and H. Tango, "on the Universality of Inversion Layer Mobility in Si MOSFET's: Part II-Effects of Surface Orientation," IEEE Trans. Electron Devices, vol. 41, no. 12, pp. 2363-2368, Dec. 1994.

[66] J. A. del Alamo, "Nanometre-Scale Electronics with III-V Compound Semiconductors," Nature, vol. 479, pp. 317-323, Nov. 2011.

[67] T. Akazaki, J. Nitta, H. Takayanagi, T. Enoki, and K. Arai, "Improving the Mobility of an In0.52Al0.48As/In0.53Ga0.47As Inverted Modulation-Doped Structure by Inserting a Strained InAs Quantum Well," Appl. Phys. Lett., vol. 65, pp. 1263-1265, Sep. 1994.

[68] F. Schäffler, "High-Mobility Si and Ge structures," Semicond. Sci. Technol., vol. 12, pp. 1515-1549, Aug. 1997.

[69] M. Hanabe, T. Otsuji, T. Ishibashi, T. Uno, and V. Ryzhii, "Modulation Effects of Photocarriers on the Terahertz Plasma-Wave Resonance in High-Electron-Mobility Transistors under Interband Photoexcitation," Jpn, J. Appl. Phys., vol. 44, no. 6A, pp. 3842-3847, Jun. 2005.

[70] M. Lundstrom and Z. Ren, "Essential physics of carrier transport in nanoscale MOSFETs," IEEE Trans. Electron Devices 49, 133, 2002

[71] R. F. Pierret, Advanced Semiconductor Fundamentals (Prentice Hall, Englewood Cliffs, NJ, 2003) 2nd ed., p. 113.

[72] M. Lundstrom and J. Guo, Nanoscale Transistors: Device Physics, Modeling, and Simulation (Springer, New York, 2006) Chap. 1, p. 8

[73] J. Y. Park. S. -H. Kim, and K. R. Kim, "Extended design window of resonant plasma-wave transistor for terahertz emitter by considering degenerate carrier velocity model with Fermi-Dirac distribution," Jpn. J. Appl. Phys., vol. 54, 2015.

[74] M. Depas, T. Nigam, and M. M. Heyns, "Soft breakdown of ultra-thin gate oxide layers," IEEE Trans. Electron Devices 43, 1499, 1996.

감사의 글

이번 박사 학위논문 집필은 지금까지 해왔던 내용을 다시 한번 정리한다는 의미에서 즐겁고 신중하게 진행하고자 노력하였습니다. 2013년에 입학한 이래로 2020년인 지금에 이르는 과정을 천천히 살펴본 셈인데, 그동안 진행하였던 연구 하나하나에 많은 분들께 큰 은혜를 받아왔다는 것을 새삼스럽게 느끼게 됩니다. 우선 제가 생각하는 바를 진지하게 경청하여 주시고 교정하여 주시면서, 저의 길고 긴 이론적인 연구의 과정들을 기다려 주시고 지켜 봐주신 저희 교수님께 가장 큰 감사를 표하고자 합니다. 교수님께서 연구와 관련하여 날카롭게 지적하여 주시는 일면과, 그 외의 연구실생활과 관련된 부분에서 학생들에게 편하게 대하여 주시는 일면에서 인간적으로 많은 감화를 받았습니다. 논문화 하지 않은 연구 결과들이 상당히 많다는 것을 이번 기회에 다시 한번 파악하게 되었는데, 논문 끝에 언급한 해결 과제들을 포함하여 남김없이 눈문으로 발표하는 것이 교수님의 배려와 큰 은혜에 보답하는 길이 되지 않나 생각합니다. 또한 수업이나 논문 디펜스 등으로 제게 큰 도움을 주셨던 전기전자공학과와 물리학과 교수님들께 깊은 감사를 드립니다. 연구실에서 박사 후 과정을 하고 계신 민우형과는 오랜 세월을 같이 하면서 쌓았던 많은 추억이 있습니다. 보통 다른 연구실에서는 학생들끼리 깊이 반목하는 경우도 있다고 들었는데 (?), 이런 일이 없게끔 연구실의 분위기를 올바르게 잡아주셔서 학생들에게 쓸데없는 부분을 배제하고 연구에만 집중할 수 있게끔 해주셨습니다. 또한 저에게 테라헤르츠 연구와 관련하여 많은 조언을 해주셨습니다. 각종 실험의 과정들과 비공진 현상을 이해하는데 있어서 민우형의 논문들과 조언이 너무나도 큰 도움이 되었습니다. 앞으로도 계속 보겠지만, 지면상으로 진심 어린 감사를 표합니다. 함께 연구를 시작하였다가 지금은 조금 다른 과제를 연구하고 있는 성호와도 참으로 오랜 기간 연구실생활을 보냈습니다. 연구를 진행하면서 도와주는 부분도 많고, 연구 외에도 같이 어울려준 점에 대하여.. 특히 술 자체를 자주 마시지는 않았지만 마신다면 성호와 가장 자주 마셨던 것으로 아는데, 저의 정신적인 측면에서 지지하여준 바에 대하여 감사를 표합니다. 또한 재원이와는 참된 의미에서 지음의 관계라 말할 수 있습니다. 같이 여행도 가보고, 비슷한 취미를 공유하면서 보낸 즐거운 추억들이 참으로 깊습니다. 이에 대해 감사를 표합니다. 이산이는 참으로 두루두루 알고 있는 것이 많은데, 이산이도 저와 엇비슷한 취미로 함께 즐겁게 보낸 나날이 많습니다. 가끔 테라헤르츠 연구에 관하여 이야기를 나누면 참 도움이 많이 되었던 바, 깊은 감사를 드립니다. 상효는 본인이 진행하고 있는 연구에 진정으로

몰두하고 있는 모습이 보기 좋다고 생각해왔습니다. 세세한 연구실 관리에 관련하여 상효에게 부탁한 것이 많은데, 이를 묵묵히 때로는 본인의 의견도 성실하게 표현하면서 도와준 점에 대하여, 또한 이산이나 민우형과 마찬가지로 테라헤르츠 연구와 관련하여 나눈 이야기는 큰 도움이 되었던 바, 진심 어린 감사를 표합니다. 항상 열심히 연구하고 공부하는 영은이와도 학회 등지에서의 즐거웠던 추억을 가지고 있습니다. 앞으로 하는 연구에 건투를 빕니다. 우석이도 제주도에서 함께 했던 좋은 기억이 떠오릅니다. 재원이 아래에서 바쁘게 일하면서도, 이따금씩 부탁하는 바에 잘 따라준 점에 대하여 감사를 드립니다. Finally, Ramesh thank you for your helpful advices and congratulations on your wedding.

학교 외에서는, 연구에만 집중하느라 제가 나서서 누군가를 찾아가기 위해 울산을 벗어난 적도, 아예 제가 먼저 연락한 적이 거의 없습니다. 원래라면 연구 외의 인간관계는 파탄이 나야 마땅한 상황인데, 그럼에도 불구하고, 저에게 항상 먼저 연락을 주곤 하였던 분들께 큰 감사를 드립니다. 먼저 고등학교 친구 병희와는 너무나 오랜기간동안 함께 보낸 추억이 많으며, 계속 연락을 지속하여 주는 점에 감사를 표하며, 앞으로 하는 일에 무엇이든, 어떤 난관에도 결국에는 원하는 방향으로 나아가기를 진심으로 바랍니다. 대학교 친구인 지환이형에게는 보자고 계획을 잡아주셔도 찾아가지를 않아서 죄송한 마음이 큽니다. 언제 찾아가도 반갑게 맞이하여 주실 분인데, 인하형에게도 동일한 이유로 죄송한 마음을 표합니다. 영태에게도 항상 먼저 연락하여 주고, 아예 울산에 일관계로 내려오더라도 제가 만나주지를 않아서 항상 미안한 마음이 큽니다. 결혼을 앞둔 창섭이에게 앞으로의 축복을 빌고, 우상이도 앞으로 하는 일이 잘되길 기원합니다. 베트남에서 열심히 일하고 있는 진영이에게도 항상 수고가 많습니다.

또한 항상 찾아가면 좋은 친구가 되어주고, 많은 조언도 하여주는 형님에게 큰 감사를 드립니다. 마지막으로 연락도 자주 드리지 못하고, 찾아뵙지도 못하는 불효를 저지르는 저에게 계속 큰 격려를 하여 주시는 저의 어머님과 아버님께 직접 말씀은 못드려 왔지만 글로 표현하기에는 부족할 정도로 항상 감사함과 죄송한 마음을 느끼고 있음을 함께 전합니다.

시간 관계 상 언급하지 못한 많은 분들에게 깊은 감사를 표합니다.

2020년 1월 울산에서